On the Experimental Generation and Characterization of Entangled States of Light

Von der Fakultät für Mathematik und Physik
der Gottfried Wilhelm Leibniz Universität Hannover
zur Erlangung des Grades

Doktor der Naturwissenschaften
– Dr. rer. nat. –

genehmigte Dissertation
von

Dipl.-Phys. James DiGuglielmo

geboren am 22. April 1982 in Belleville, New Jersey
Vereinigte Staaten von Amerika

2010

Referent: Prof. Dr. Roman Schnabel
Korreferent: Prof. Dr. Karsten Danzmann
Tag der Promotion: 15.07.2010

Abstract

Shared entanglement combined with local operations and classical communication can be used as the physical resource for a communication channel. It is therefore important to develop the experimental techniques to prepare various multipartite entangled states and characterize their entanglement properties. Additionally, since all experimental results involve statistical uncertainty, methods to estimate this uncertainty and propagate it through further calculations is essential for any proof-of-principle experiment.

The first set of experimental results to be presented involves the preparation and characterization of various classes of bipartite quadrature entanglement. These states are reconstructed by measuring the full 4×4 covariance matrix and evaluating from it information theoretic quantities such as the raw secret key rate, the quantum channel capacity and the teleportation fidelity for coherent states. The connection between the quantity of entanglement and its utility as a communication channel is numerically explored.

The next experiment focuses on a new statistical scheme based on the Bayesian paradigm for quantum state reconstruction. The key result of this work is the calculation of error-bars in the form of a probability distribution known as the posterior distribution on the reconstructed Wigner function for phase-diffused squeezed states. The method relies on the Markov chain Monte Carlo algorithm to draw samples from the posterior distribution. Since these samples contain all of the relevant statistical information with regard to the reconstruction, probability distributions can be derived for quantities, such as the state purity, without having to make additional assumptions as to the distributional form of the statistical uncertainties.

Finally, the experimental demonstration of Gaussian bound entangled states is presented. Continuous-variable bound entanglement is an example of a four party mixed entangled state, whose preparation requires precise control over a network of interference beam splitters, homodyne detectors and nonlinear optical cavities. The experimental and feedback control techniques required for this task are explained and illustrated using results from the laboratory. Finally, the experimental demonstration of bound entanglement is presented along with a discussion of the data analysis methods and possible improvements for future experiments.

Having demonstrated the capability to control multimode entangled states, it becomes possible to explore various other types of multipartite entangled states for both quantum communication and quantum computing.

Keywords: Mutlipartite entanglement, Bound Entanglement, Quantum State Reconstruction.

Zusammenfassung

Verschränkte Zustände bilden zusammen mit lokalen Operationen und klassischer Kommunikation die physikalische Grundlage eines Quantenkommunikationskanals. Deshalb sind die Entwicklung von experimentellen Techniken zur Herstellung unterschiedlicher verschränkter Zustände sowie ihre Charakterisierung von besonderer Bedeutung.

Da alle Experimente, unter anderem sogenannte "proof-of-principle" Versuche, durch statistische Ungewissheit begrenzt sind, ist auch die Entwicklung von Methoden der Fehleranalyse wichtig. Beginnend mit der Charakterisierung der freien Verschränkung wird der Zusammenhang zwischen der Verteilung verschränkter Zustände und der Quantenkommunikation theoretisch wie auch experimentell dargestellt. Die vollständige Messung der Kovarianzmatrix diverser verschränkter Zustände liefert Einsichten in Informationen wie die Kapazität des Quantenkanals (quantum channel capacity), die Quantengenauigkeit (fidelity) und andere.

Ferner wurde ein neues Bayes'sches Verfahren zur Quantenzustandsrekonstruktion eingeführt. Dieses ermöglicht es, die Fehler einer Rekonstruktion aus der sogenannten Posterior Verteilung mithilfe des Markov chain Monte Carlo Algorithmus zu berechnen. Da somit die vollständige, statistische Information der Rekonstruktion vorliegt, können weitere Eigenschaften des Zustandes wie z.B. die Reinheit ohne zusätzliche Annahmen bestimmt werden.

Schlussendlich wird der experimentelle Nachweis Gaußscher gebundener Verschränkung dargestellt. Die Erzeugung fand im Regime kontinuierlicher Variablen statt und benötigte neben linearen Elementen wie Phasenschiebern, Interferenzstrahlteilern und Homodyndetektoren auch nicht-lineare Resonatoren und genaue Reglungstechniken. Diese Methoden sind anhand der experimentellen Ergebnisse beschrieben. Der experimentelle Nachweis der gebundenen Verschränkung wird auch im Rahmen der Datenanalyse diskutiert.

Die Herstellung von Mehrmoden Verschränkung ermöglicht die Untersuchung verschiedener Arten von Verschränkung für die Quantenkommunikation bzw. den Quantencomputer.

Schlüßelwörter: gebundene Verschränkung, Quantenzustandsrekonstruktion, Mehrmoden Verschränkung.

List of Publications

- J. DiGuglielmo, B. Hage, A. Franzen, J. Fiurášek, and R. Schnabel, *Experimental characterization of gaussian quantum-communication channels*, Physical Review A **76** (2007), 012323.
- J. DiGuglielmo, C. Messenger, J. Fiurášek, B. Hage, A. Samblowski, T. Schmidt, and R. Schnabel, *Markov chain monte carlo reconstruction of quantum states*, Physical Review A **79** (2009), 032114.
- A. Franzen, B. Hage, J. DiGuglielmo, J. Fiurášek, and R. Schnabel, *Experimental demonstration of continuous variable purification of squeezed states*, Physical Review Letters **97** (2006), 150505.
- B. Hage, A. Franzen, J. DiGuglielmo, P. Marek, J. Fiurášek, and R. Schnabel, *On the distillation and purification of phase-diffused squeezed states*, New Journal of Physics **9** (2007), 227.
- B. Hage, A. Samblowski, J. DiGuglielmo, A. Franzen, J. Fiurášek, and R. Schnabel, *Preparation of distilled and purified continuous-variable entangled states*, Nature Physics **4** (2008), 915.
- T. Kiesel, W. Vogel, B. Hage, J. DiGuglielmo, A. Samblowski, and R. Schnabel, *Experimental test of nonclassicality criteria for phase-diffused squeezed states*, Physical Review A **79** (2009), 022122.
- P. Marek, J. Fiurášek, B. Hage, A. Franzen, J. DiGuglielmo, and R. Schnabel, *Multiple-copy distillation and purification of phase-diffused squeezed states*, Physical Review A **76** (2007), 053820.

Contents

Abstract **i**

Zusammenfassung **iv**

List of Publications **vi**

List of Figures **xi**

List of Tables **xiv**

1 Introduction **1**

2 Physical Systems and Information Transfer **5**
- 2.1 The Quantum State of Light 5
- 2.2 Characterizing Quantum Noise 7
  - 2.2.1 Statistical Distributions: Wigner Function 8
  - 2.2.2 Gaussian States 10
- 2.3 Characterizing Information 10
  - 2.3.1 Basic Illustration of Information 11
  - 2.3.2 Quantifying Information 12
- 2.4 Quantum Noise and Information Transfer 12
  - 2.4.1 Entanglement Based Information Transfer 13
  - 2.4.2 Carrying Classical Information: Dense Coding 15
  - 2.4.3 Carrying Quantum Information: Teleportation 17
- 2.5 Distillability and Information: Bound Entanglement 18

3 Free Entanglement **21**
- 3.1 The Separability Problem 21
  - 3.1.1 Peres-Horodecki: NPT Entanglement 22
  - 3.1.2 Duan Criterion 24
  - 3.1.3 Separable Matrices 27
- 3.2 The Measurability Problem 28
  - 3.2.1 Distance Measures 28
  - 3.2.2 Operational Measures 29
  - 3.2.3 Utility Measures 29
- 3.3 The Distillability Problem 31

3.4 Summary 31

4 Bound Entanglement 33
4.1 Criteria for Bound Entanglement 33
4.1.1 PPT Condition 34
4.1.2 Inseparability Condition 34
4.2 Searching for Bound Entangled States 35
4.3 Reversible and Irreversible Transformations 36
4.3.1 Reversible Transformations 37
4.3.2 Irreversible Transformations 38
4.3.3 Bound Entanglement and Irreversible Transformations 38
4.4 Summary 38

5 Laboratory Tools: Devices and Techniques 41
5.1 Building Blocks of an Entanglement Experiment 41
5.1.1 Nonlinear Devices: The Optical Parameteric Amplifier 41
5.1.2 Linear Devices: Beam splitters, Phase Shifters and Mode Cleaner . . 43
5.1.3 Homodyne Detection 44
5.2 Feedback Control Schemes 46
5.2.1 Optical Fields and Classical Modulations 46
5.2.2 Single-Sideband: Phase-Lock Loop 47
5.2.3 Setting a Phase-Gate 48
5.3 Generation of Hot Squeezing 51
5.3.1 Method 1: EPR-Approach 51
5.3.2 Method 2: Modulation Approach 52
5.4 Summary 52

6 Reconstructing a Quantum State 53
6.1 Bayesian Statistical Analysis 54
6.1.1 Assigning the Likelihood 55
6.1.2 Assigning the Prior 56
6.2 Markov Chain Monte Carlo 57
6.2.1 Basic Idea 58
6.2.2 Metropolis-Hastings Algorithm 59
6.3 Reconstructing a Phase-Diffused Squeezed State 64
6.3.1 Deriving the Posterior 65
6.4 Description of the Experiment 66
6.5 Sampling from the Posterior 68
6.5.1 Results of the MCMC 68
6.5.2 Estimating the State Purity 69
6.6 Summary 70

7 Entanglement as a Communication Channel 71
7.1 Experimental modus operandi 72
7.1.1 Preliminary Considerations 72
7.1.2 Description of the Partial Tomographic Protocol 73
7.2 Experimental setup 74
7.3 Experimental implementation of PTP 75
7.4 Theoretical description of Quantum Communication Channels 76
7.5 Experimental Results 79
7.6 Discussion 82
7.7 Summary 82

8 Experimental Demonstration of Gaussian Bound Entangled States 83
8.1 Experimental Procedure 83
8.1.1 Preparing the Input Squeezed States 84
8.1.2 Setting the Phase-Gate Operating Point 85
8.1.3 Setting the Homodyne Detectors 89
8.1.4 Data Acquisition 90
8.2 Presentation and Analysis of Results 91
8.2.1 First Results 92
8.2.2 Data Binning 93
8.2.3 Determining Physical Matrices 93
8.3 Summary 94

9 Conclusion and Outlook 97

A Rules for Experimentalists 99
A.1 Rule 1: Impedance Matching 99
A.2 Rule 2: Ground loops 100
A.3 Rule 3: RF Pickup 101

Literature 101

Acknowledgements 109

Selbständigkeitserklärung 111

List of Figures

2.1 Depiction of a physical resource for a communication channel 6
2.2 Quantum noise of the electric field for squeezed and vacuum states 8
2.3 Example Wigner functions 9
2.4 Illustration of basic concepts in information theory 11
2.5 Experimental implementation of a coherent state and entangled state communication channel 13
2.6 Quantum noise projections of Alice and Bob's local modes 14
2.7 Quantum noise projections of Alice and Bob's joint modes 15
2.8 Channel capacities for dense coding and teleportation of coherent states . . . 16
2.9 Quantum noise explanation of dense coding 17
2.10 Experimental setup for teleportation 18
2.11 Quantum noise explanation of teleportation 19

3.1 Distance measure of entanglement 28
3.2 Log-Negativity and Entanglement of Formation 30

4.1 Bound entanglement preparation circuit 36
4.2 Robustness of bound entanglement 37

5.1 $\chi^{(2)}$ nonlinear optical processes 42
5.2 Power spectrum of laser from mode cleaner 44
5.3 Phase-lock loop for single-sideband scheme 47
5.4 Setup for single photodetector phase-gate locking 49
5.5 Setup for dual photodetector phase-gate locking 50
5.6 Single-sideband error-signals 51
5.7 Methods to generate hot squeezing 52

6.1 Example posterior space 58
6.2 Strategies for posterior sampling 60
6.3 Selecting proposal distribution standard deviations 61
6.4 Behavior of proposal distributions 63
6.5 Markov Chains from reconstruction of phase-diffused squeezed states 67
6.6 Marginalized posteriors from MCMC: Phase-diffused squeezed states 68
6.7 Probability density on the state purity 69

7.1 Classes of entanglement 73

7.2 Experimental setup for quantum communication channels 75
7.3 Simulated channel properties for S and V-Class entanglement 81

8.1 Bound entanglement experimental setup 86
8.2 Setting the phase-gates 87
8.3 Relationship between carrier field and quantum noise 88
8.4 DC voltage from single phase-gate locking photodetector 89
8.5 DC voltage from single homodyne photodetector 90
8.6 Schematic of data acquisition pipeline 91

A.1 Effect of impedance matching on bandpass circuit 100

List of Tables

6.1 List of conjugate priors 57
6.2 Basic Markov chain Monte Carlo concepts 59

7.1 Measured channel characteristics for V-Class and S-Class entanglement . . . 77

8.1 Parameters for preparing a bound entangled state 84
8.2 Average quantum noise phase-gates 86
8.3 Non-invariance of phase-gates 88
8.4 Measurement settings for bound entanglement 92
8.5 Data binning results 93
8.6 Data binning results using 2-norm 94
8.7 Data binning results using 1-norm 94

1

Introduction

In the early years of quantum mechanics Erwin Schrödinger discovered a class of states for which, as he phrased it, knowledge of the complete state does not imply knowledge of its constitute components [Sch35]. He described these states as being “verschränkt” or entangled in order to encapsulate in one concept the fact that these states demand an all or nothing approach when trying to characterize them. Since that time, entanglement has been the subject of much research both theoretical and experimental. Its study has lead to fundamental experiments in physics as illustrated by Aspect in measuring the violation of certain Bell inequalities [AGR81]. But entanglement is more than just another quantum state, it is a resource for transmitting quantum and classical information which can demonstrably surpass any classical resource [BTB$^+$03b, JZY$^+$03]. It is this feature of entanglement that is explored by the experiments performed for this thesis.

Beginning with Chapter 2 I motivate the fact that entanglement is a physical resource for information transfer by first generally illustrating what role a physical channel plays in information transfer. This requires taking into consideration the quantum fluctuations of light in order to determine the fundamental limits set by the physical resource. I show how the electric field is quantized and how these quantum fluctuations are quantified. I then introduce a bipartite entangled state and illustrate how the noise variance behaves depending on which quadratures are examined. With an understanding of how to characterize quantum noise, I introduce the dense coding protocol and analyze it in terms of the evolution of its quantum noise properties. This yields an intuitive understanding of why this protocol can always improve the classical information carrying capacity of a channel over any classical resource [BK00]. As a second example, I introduce the teleportation protocol and again explain its operation using the evolution of its quantum noise properties. Teleportation highlights the fact that entanglement is not only a good resource for classical information but also for sending unknown quantum states [BBC$^+$93, BK98].

Having given an overview of entanglement and its role as a physical resource for information transfer, I introduce the mathematical theory of entanglement in Chapter 3. Entanglement theory concerns itself with three main problems: *separability*, *measurability* and *distillability*. The first of these seeks to develop necessary and sufficient criteria for detecting inseparable states. One of the first criteria developed was introduced by Peres [Per96] and is known as the nonpositive partial transpose. It identifies entangled states by looking for those states which fail to remain positive under partial transposition. As I discuss in the chapter, when developing criteria for entanglement certain properties of states or observables are used to identify entanglement. I discuss all criteria at the level of both density matrices and covariance matrices, the latter being important for Gaussian quantum states since the finite dimensional covariance matrix provides a full description. The measurability problem is treated next, where I discuss the logarithmic negativity since it corresponds to a computable entanglement measure for continuous-variable systems [VW02]. Finally, the distillability problem is discussed with a view towards the following chapter on bound entangled states. I cite some protocols designed to distill against different forms of decoherence and reference some recent experimental work for both single-copy and iterative entanglement distillation.

In Chapter 4 I introduce bound entangled states. These are states which, although inseparable, cannot be distilled. These states were first discovered by Horodecki *et al.* in connection with mixed state entanglement and distillation and have since been the subject of much theoretical work [HH98, WW01, KLC02, Mas06]. A method to prepare these states in the continuous-variable regime using quadrature entanglement is presented along with simulations as to their robustness. With regard to their utility for quantum information processing tasks, such as quantum cryptography and teleportation, there is mixed reviews in the literature. Horodecki showed [HHH] that with bound entanglement teleportation cannot be performed better than through a classical channel. In [Mas06], Masanes showed that for two parties any entangled state can enhance the teleportation power over any other. Regardless of their possible applications to quantum information processing, they create another avenue through which some fundamental questions regarding the relationship between information, thermodynamics and entanglement theory can be explored. As I briefly discuss in the last section of the chapter, the preparation of bound entanglement is an example of an irreversible process since distillable entanglement is required for its preparation but cannot be restored after.

Chapter 5 contains a complete description of all the laboratory techniques and devices developed for the experiments performed in this thesis. I start by discussing the nonlinear optical components since quadrature squeezing is a fundamental resource for the generation of quadrature entanglement. I next discuss some linear optical components such as beam splitters and the mode cleaner. The main part of the chapter is dedicated to explaining the single-sideband optical RF locking scheme developed for controlling the bound entanglement experiment. This method enables the setting of the relative phase between interfering fields to an arbitrary angle. It does this by reducing the setting of the working point to adjusting the electronic demodulation phase. I derive the error-signal for this control scheme and show how it can be used to set both the homodyne detectors and the phase-gates to an arbitrary relative phase. Finally, the preparation of bound entanglement requires a type of squeezing known as “hot squeezing”. This is a state for which the conjugate quadratures exhibit different noise powers none of which fall below the quantum noise level.

The first few chapters of this thesis are preparatory material for the experimental results which are presented in the remaining chapters. Those results begin in Chapter 6 where I present a new method based on Bayesian statistics for the reconstruction of a general quantum state. I start the chapter by introducing the Bayesian statistical paradigm. Unlike the so called “frequentist approach”, Bayesian statistics treats probabilities as degrees of uncertainty rather than the limiting values of long-run trials. I treat quantum state reconstruction as a parameter estimation problem and show how the posterior distribution, which quantifies the statistical uncertainties on the underlying parameters, can be derived from the likelihood function and prior. In order to obtain the marginalized posteriors, which provide an estimate of the uncertainty on the individual parameters, I make use of the Markov chain Monte Carlo algorithm to perform the high dimensional integration. I explain the steps of the algorithm and include Matlab code snippets to illustrate the actual implementation. As a test case for quantum state reconstruction, I consider the phase-diffused squeezed states. Due to their non-Gaussian Wigner function, they cannot be described by the covariance matrix alone. But since they can be modeled, the entire reconstruction scheme can be reduced to estimating a few parameters. After the reconstruction, I use the Markov chain to calculate the purity of the state, showing how a probability distribution on the purity containing all of the relevant statistical information can be obtained from the method.

In Chapter 7, I turn to the experimental study of distributed quadrature entanglement as a communication channel. Three classes of CV quadrature entanglement are identified corresponding to the preparation procedure used to generate the entanglement. After deriving some quantities that characterize entanglement as a quantum channel, e.g. quantum channel capacity, teleportation fidelity of coherent states etc, I present the reconstructed covariance matrix for each prepared state. A key experimental result is that the full ten parameter covariance matrix is measured and the technical details behind the measurement are explained in full detail. Finally, I use the reconstructed covariance matrices to evaluate the channel characteristics and conclude with a discussion of the results.

In the last chapter, I present an experimental preparation of Gaussian bound entangled states. Preparing a bound entangled state requires the construction of a four party entangled state. The experimental setup involves multiple beam splitters, phase shifters, nonlinear squeezing sources and homodyne detectors all of which must be set to specific operating points in order to produce the desired state. A procedure for preparing these states is developed and demonstrated with examples from the laboratory. Since these states are Gaussian, it is sufficient to measure the 8×8 covariance matrix. As will be seen, however, the reconstructed matrix can fail to correspond to a bona fide quantum state. This can be an indication that the overall amount of experimental and statistical error is large. Numerical methods to obtain the nearest physical state to that which is measured are discussed and applied to the measured data.

Entangled states of light provide a test bench to understand not only fundamental properties of nature but also the constraints a physical system places on information transfer. Before these constraints can be fully explored, the connection between physical resources and communication channels needs to be established and is the topic of the next chapter.

2

Physical Systems and Information Transfer

2.1 The Quantum State of Light

The advent of the telegraph ushered in a period in which physical systems, such as electrons, would no longer be considered merely as one of nature's fundamental building blocks but also as a useful resource for information transfer. A further implication of this notion is that information transfer has as much to do with the available physical resources as it does with the way in which a message is represented. The systematic study of these resources is the domain of the physics of information.

While modern telecommunication is introducing fiber optics, the basic principles behind the physics of information remain the same. These principles are best illustrated by example. Suppose Alice has a message that she wants to communicate with her distant friend Bob. She decides to encode her message using photons and sends them through a fiber optic link to Bob. The maximum amount of information that can be transfered using this channel is quantified by the *channel capacity* and is given in this case by [BK00]

$$C = \ln\left(1 + \bar{n}\right), \tag{2.1}$$

where $\bar{n}$ quantifies the average number of photons in each pulse. The more photons Alice employs the larger the capacity to transmit information using this channel.

The description of the physical channel shared between Alice and Bob as the average number of photons ignores the fact that light possess two physical properties, an *amplitude* and a *phase*. In order to incorporate the phase property, the channel is described by a series of equally spaced arrows each with a different length as seen in Figure 2.1a and Figure 2.1b. The length of each arrow corresponds to the amplitude of the signal and the distance between the arrows represents the time interval between each sent signal, representing the phase. The relationship between the average number of photons, $\bar{n}$, and the length of each arrow is given

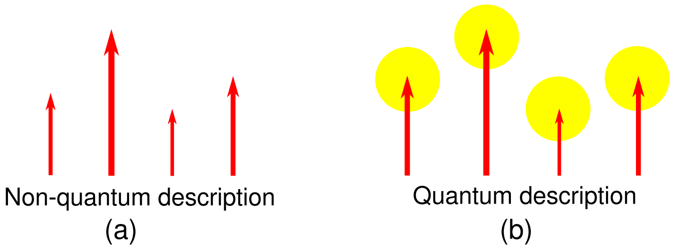

FIGURE 2.1: Physical resource shared between Alice and Bob: In order to send a message to her distant friend Bob, Alice uses as a physical channel light pulses, represented here by the various lengths of the arrows. The spacing between the arrows represents the time interval between each new pulse. When ignoring the quantum fluctuations of the light, Figure(a) , each pulse possess a well defined amplitude and phase. The situation is much different when quantum noise is considered, Figure(b). Then it is seen that neither the amplitude nor the phase is well defined. The limit at which the amplitude and orientation can be known is given by the Heisenberg uncertainty relation and is represented by the edge of the yellow ball. The uncertainty in the amplitude and phase limits the information carrying capacity of the channel.

the *coherent* states defined by

$$|\alpha\rangle = \exp(-\frac{1}{2}\,|\alpha|^2)\sum_{n=0}^{\infty}\frac{\alpha^n}{\sqrt{n}}|n\rangle, \tag{2.2}$$

where $|n\rangle$ is vector in the Fock basis and α is the eigenvalue of the annihilation operator in the coherent state basis, $|\alpha\rangle$. Calculating the average number of photons in a coherent state, where the number operator is defined by $\hat{n} = \hat{a}^{\dagger}\hat{a}$ and $\hat{a}^{\dagger}$, $\hat{a}$ are the creation and annihilation operators, respectively yields

$$\langle\alpha|\hat{n}|\alpha\rangle = |\alpha|^2, \tag{2.3}$$

which corresponds to the lenght of each arrow.

The resource depicted in Figure 2.1a assumes that each arrow possess a well defined amplitude and phase. This is the case if the quantum nature of light is ignored. The situation looks much different if the *quantum noise* properties of the light are considered. Figure 2.1b depicts the same resource as Figure 2.1a but this time including the effects of quantum fluctuations. Whereas in the non-quantum noise scenario the arrows all have well defined tips and orientations, the effect of quantum noise is to introduce *uncertainty* into both of these features as indicated by the yellow area surrounding each arrow. This is a fundamental property of any physical system and prohibits a precise preparation and detection of a pulse regardless of the means employed by Alice and Bob. The quantum theory of light quantifies the amount of uncertainty for the states depicted in Figure 2.1b through the variance of the amplitude and phase fluctuations. Their product defines the minimal uncertainty and is known as the *Heisenberg uncertainty* relation

$$\langle\Delta^2 X\rangle\langle\Delta^2 P\rangle \geq 1, \tag{2.4}$$

where X corresponds to the amplitude of the light field and P corresponds to the phase. States for which equality is achieved are said to be "minimal uncertainty" states. Additionally, states for which $\langle \Delta^2 X \rangle = 1$ and or $\langle \Delta^2 P \rangle = 1$ are referred to as being "vacuum noise limited". Since quantum fluctuations are apart of any physical system, it would seem the very desirable situation depicted in Figure 2.1a is beyond reach. As I will show in the following sections, the vacuum noise limit can be breached by manipulating the very source of the problem.

2.2 Characterizing Quantum Noise

Figure 2.1a-b is a pictoral representation of quantum noise. An example of the effect of quantum noise is depicted in Figure 2.2a-b. The plots correspond to a simulated measurement of squeezed vacuum state, Figure 2.2a, and the vacuum state, Figure 2.2b of the quantized electromagnetic field. The vacuum state is seen to posses time-independent noise whereas the squeezed state periodically varies between becoming more and less noisy than the vacuum state.

To see how these two different cases are due to the quantum fluctuations of light, the single-mode electric field must first be written in its quantized form

$$\hat{E}(\chi) = \mathcal{E}_o(\hat{a}e^{-i\chi} + \hat{a}^\dagger e^{i\chi}), \tag{2.5}$$

where $\chi = \omega t$ is the phase of the field, $\mathcal{E}_o = \sqrt{\hbar\omega/\epsilon_o V)}$ is a measure of the strength of the electric field per photon and $\hat{a}, \hat{a}^\dagger$ are the annihilation and creation operators, respectively, with commutator given by [GK05]

$$[\hat{a}, \hat{a}^\dagger] = 1. \tag{2.6}$$

Equation (2.5) can be rewritten in terms of the so called quadrature operators and is given by

$$\hat{E} = \mathcal{E}_o[\hat{X}_1 \cos(\chi) + \hat{X}_2 \sin(\chi)], \tag{2.7}$$

where the quadratures are defined in terms of the annihilation and creation operators by

$$\hat{X}_1 = \hat{a} + \hat{a}^\dagger, \quad \hat{X}_2 = i(\hat{a}^\dagger - \hat{a}). \tag{2.8}$$

In order to see the quantum fluctuations associated with the quantized field, I calculate the variance of the field for both the vacuum state and the squeezed state. In the Fock basis the vacuum and squeezed states are given by

$$|\text{vac}\rangle = |0\rangle, \quad |\xi\rangle = \hat{S}(\xi, \theta)|0\rangle, \tag{2.9}$$

where

$$\hat{S}(\xi, \theta) = \exp[\frac{1}{2}(\xi^* \hat{a}^2 - \xi \hat{a}^{\dagger 2})], \tag{2.10}$$

is the squeezing operator with $\xi = re^{i\theta}$ where r is the squeezing parameter which determines the amount of squeezing in the state and θ which determines the squeezed quadrature. The variance of the electric field for the vacuum state is given by

$$\langle \Delta^2 \hat{E} \rangle = \mathcal{E}_o^2 \tag{2.11}$$

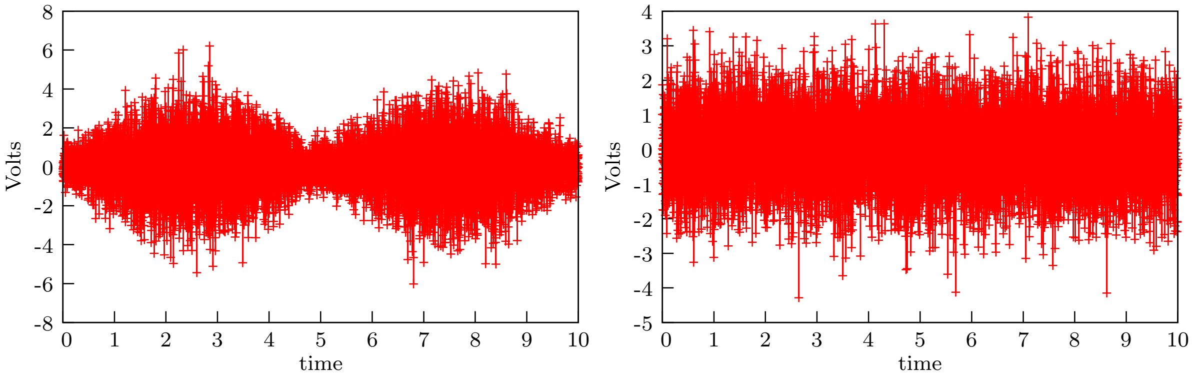

(a) Squeezed vacuum state (b) Vacuum state

FIGURE 2.2: Quantum noise of the quantized electric field: These figures depict simulated noise traces corresponding to a squeezed vacuum state, Figure(a), and a vacuum state, Figure(b) of the quantized electromagnetic field. The noise of the vacuum state is seen to be constant whereas the noise of the squeezed state varies with time. This is the representation of the fact that a squeezed state exhibits less quantum fluctuations than the vacuum level in one quadrature and excess fluctuations in the conjugate quadrature.

and for the squeezed state by

$$\langle \Delta^2 \hat{E} \rangle = \mathcal{E}_o^2 [\langle \Delta^2 \hat{X}_1 \rangle \cos^2(\chi) + \langle \Delta^2 \hat{X}_2 \rangle \sin^2(\chi)], \tag{2.12}$$

where it is assumed that $\langle \Delta^2 \hat{X}_1 \rangle < \langle \Delta^2 \hat{X}_2 \rangle$. Equation (2.11) shows that the variance of the field is independent of the phase and is therefore equal in all quadratures. For a squeezed state, however, Equation (2.12) shows that the quantum fluctuations are phase-dependent and predicts the behavior of the field in Figure 2.2. Squeezed states enable one to reduce the quantum fluctuations in one quadrature below the vacuum noise limit at the expense of increasing them above the vacuum noise limit in the conjugate quadrature.

2.2.1 Statistical Distributions: Wigner Function

In Section 2.2, I considered the quantum noise properties of single-mode quantized electric fields and showed how in the case of squeezed states their quantum fluctuations are phase dependent. These fluctuations were quantified by calculating the variance of the electric field for squeezed and vacuum states. It is also possible, however, to describe quantum noise by a full probability distribution where, in the case of light, the quadrature operators act as the random variables and their eigenvalues as the samples which are distributed according to some distribution. The Wigner function is one such quasi-probability distribution and is defined for a general quantum state as the Fourier transform of the characteristic function

$$W = \frac{1}{\pi} \int \chi(\xi) \exp(\alpha \xi^* - \alpha^* \xi) d^2\xi, \tag{2.13}$$

where the characteristic function $\chi(\xi)$ is given by

$$\chi(\xi) = \mathrm{tr}\left(\rho D(\xi)\right), \tag{2.14}$$

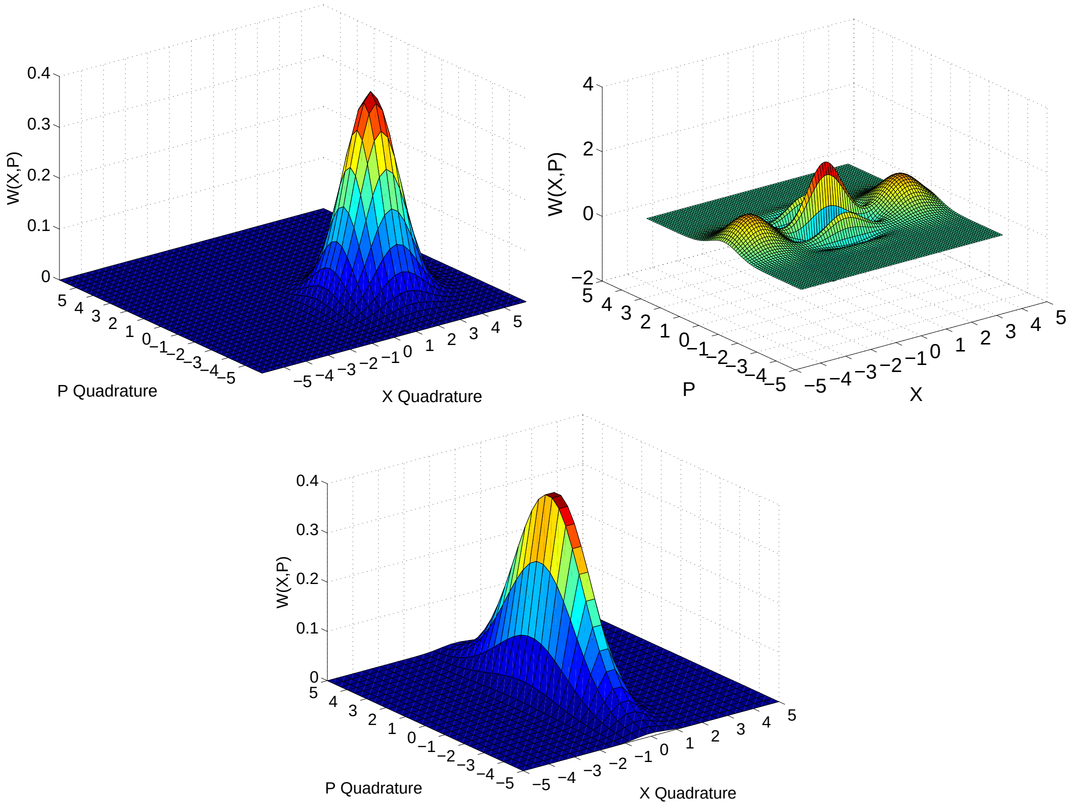

Figure 2.3: Example Wigner functions: These graphs depict the quantum noise distribution for three different quantum states. The upper left graph is a coherent state which is characterized by a Gaussian distribution shifted in phase-space corresponding to the average number of photons. The upper right graph is a non-Gaussian Schrödinger cat state which is a superposition of two coherent states and exhibits quantum interference between them. The middle graph is a Gaussian squeezed state which has reduced noise below the vacuum level in one quadrature and amplified noise above the vacuum noise level in the conjugate quadrature.

where ρ is the density matrix describing the quantum state and $D(\xi)$ is the displacement operator [CG69]. The Wigner function was first introduced by Wigner as the quantum mechanical analog of the phase-space distribution common in classical mechanics [Wig32]. The Wigner function is a “quasi” probability distribution because it is known for certain states to become negative, a property which violates the positivity condition of a bona fide probability distribution [Leo97].

Figure 2.3 provides examples of three different Wigner representations of quantum noise. The figure in the upper left hand corner is an example of a *coherent* state. This state has the properties that the center of the distribution is shifted in phase-space which physically corresponds to the mean number of photons. The width, or standard deviation, of the marginal distributions quantify the strength of the quantum fluctuations of each quadrature.

Another example of a Gaussian state is the *squeezed* state, depicted in the lower figure. This state differs from the coherent state in that the noise is reduced below the vacuum noise level in one quadrature, in this case the $\hat{X}$ quadrature, while being amplified above the vacuum noise level in the conjugate P quadrature. The last example is an illustration of a non-Gaussian *Schrödinger cat* state. The cat states are a superposition of two coherent states and exhibit *quantum interference* between them.

The Wigner function contains the full statistical information as to how the quantum noise is distributed. There is a class of states whose quantum noise properties can be captured using only the second moments of the statistical distribution. These states are known as the *Gaussian* states and are the topic of the next section.

2.2.2 Gaussian States

Gaussian states posses a Wigner function given by a Gaussian probability density

$$W(\hat{\xi}) = \frac{1}{(2\pi)^{N/2}\sqrt{\det(\gamma)}} e^{-\frac{1}{2}(\hat{\xi}-\mu)^T \gamma^{-1} (\hat{\xi}-\mu)}, \tag{2.15}$$

where $\hat{\xi}$ is a vector containing the mode operators, γ is the covariance matrix describing the second moments of the quadrature operators, N specifies the number of modes and μ is the mean vector describing the displacement of the state. This class of continuous-variable quantum states is particularly useful experimentally since they can be prepared using only beam splitters, phase shifters and squeezers. From the theoretical perspective, Gaussian states can be completely described by its mean vector, μ and covariance matrix, γ. As I will discuss in more detail in Section 7.4, Gaussian quantum communication channels established using shared entanglement are completely described by the covariance matrix of the bipartite entangled state and can be used to calculate many properties of the channel.

Before demonstrating how quantum noise can be used as a medium for information transfer, I will first briefly describe some of the key ideas in classical information theory. There are many great texts on this topic and I would suggest the following for further information [CT06]. This review of information theory will be cursory and will focus only on those concepts that are needed to understand the rest of the chapter and the rest of this thesis.

2.3 Characterizing Information

Information theory provides the mathematical basis for three main information processing tasks: *data compression*, *error-correction* and *cryptography.* The father of information theory is Claude Shannon and the entire field can be traced back to his 1948 paper "A Mathematical Theory of Communication" [Sha48]. In that paper, Shannon recognized that the information content of a message is a function of the statistical properties of its components. Knowing how a message is described statistically allows for optimal coding of the message in the sense of representing the original message using a minimal number of resources and still being able to transmit it faithfully through a communication channel. Before giving the definition of information which was defined by Shannon and now bears his name, the following example illustrates many of the key ideas behind the theory.

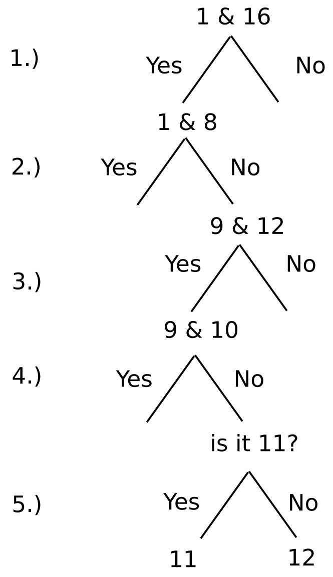

Figure 2.4: Illustration of information: This diagram depicts a game in which a player attempts to guess a number between 1 and 32. The goal of the game is to determine the unknown number asking a minimal number of questions. The Shannon information yields the minimal number of questions the player must ask. This game illustrates three properties that are common to information transfer systems: uniformity of the possible states, distinguishability of the possible states and lack of knowledge on the part of the receiver.

2.3.1 Basic Illustration of Information

To illustrate some of the basic notions from information theory imagine the following game where a player is asked to guess a number between 1 and 32. What are the minimal number of questions the player can ask in order to faithfully determine the number? Figure 2.4 provides a schematic of the optimal strategy. The strategy for the player is to break up all of the numbers into intervals of decreasing size and to ask a series of "yes/no" questions as to whether the number is within the selected interval. Depending on the answer, the player either continues forming smaller intervals or a new interval is selected. In total, the player only needs to ask five questions in order to determine the unknown number.

There are three features of this game that are worth mentioning. First, all of the numbers were equally likely and there were no correlations amongst them. Second, the numbers could be distinguished from one another enabling a series of yes/no questions to be asked. Third, the number was unknown beforehand and therefore the player had to ask in order to determine what is was. These three points, *uniformity* in the distribution of the possible numbers, *distinguishablility* of the numbers from each other and finally the *ignorance* on the part of the person playing the game are all properties that any good information transfer system will possess. The number of questions that the player had to ask quantifies the information content of the message and is known as the *Shannon information.*

2.3.2 Quantifying Information

The definition of information introduced by Shannon is given by

$$H = -\sum_{i}^{n} p_i \log p_i, \tag{2.16}$$

where n is the total number of possible states in a message, p_i is the probability for the i^{th} state to occur and the logarithm is usually taken to be base two giving the units of bits for information. With regard to the game illustrated in Figure 2.4 there were thirty-two equally likely numbers. The Shannon information in this case is

$$H = -\sum_{i=1}^{n=32} \frac{1}{32} \log \frac{1}{32} = 5 \tag{2.17}$$

yielding the number of questions that needs to be asked in order to determine the unknown number. Equation (2.16) is understood as quantifying the average amount of information within a message. Indeed, had the player been asked to guess a number between 1 and 33, they would have had to ask a total of $H = 5.044$ questions. This is a statement of the fact that sometimes the player may have to ask some additional questions in order to determine the unknown number.

I am now going to bring together the ideas of Section 2.3 and Section 2.2 and show how the quantum fluctuations of light can be used for information transfer. As will be seen, it is the unique ability of quantum states to transmit both quantum and classical information.

2.4 Quantum Noise and Information Transfer

Let us consider again Alice and Bob's physical resource depicted in Figure 2.1. The quantum noise associated with each pulse sent by Alice is described by a coherent state Figure 2.3. Since the state is Gaussian, it can be completely described by a mean vector, μ and covariance matrix γ.

Using coherent state, a possible experimental implementation is given in Figure 2.5a. In the preparation stage, Alice produces a pulse with given amplitude and phase and sends it to Bob through a fiber optic link. Bob then detects the pulse with a photodetector and records the data. The actual information Alice wants to transfer to Bob is given by the mean value of the data stream. The quantum fluctuations manifest themselves in the excess of points around the center of the stream. They set a fundamental limit as to how well each pulse can be defined in its amplitude and phase quadratures. The strength of the fluctuations is given by the variances of the amplitude and phase observables and their product sets the lower limit given by the uncertainty principle, Equation (2.4). They can, however, beat the quantum noise limit by utilizing as a physical resource a quantum state whose noise powers in both quadratures exhibit a simultaneous reduction below the vacuum noise level. States which possess these noise properties are said to be *entangled* and are the subject of the next section.

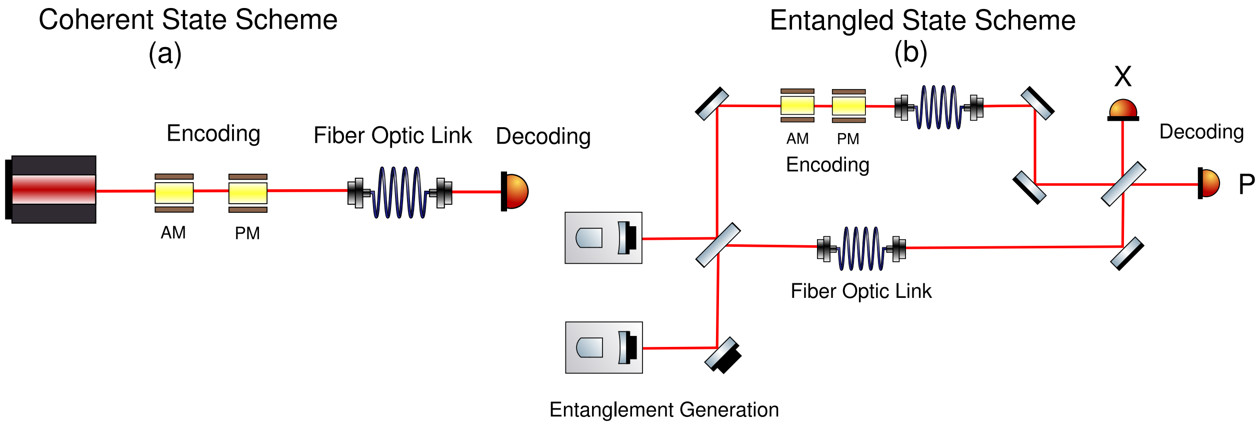

FIGURE 2.5: Coherent and entanglement based communication channels: These figures depict a possible experimental setup for establishing a communication channel using coherent states, Figure(a), and using entangled states, Figure(b). In the entanglement based scheme, two squeezed states are needed in order to build the underlying entanglement. A comparison of the information carrying capacity of these channels is given in Figure 2.8a. There it is seen that entanglement always increasing the capacity of the channel for classical information.

2.4.1 Entanglement Based Information Transfer

The coherent state scheme depicted in Figure 2.5a utilized a single mode for the information transfer. Entanglement, however, is an example of a *composite* state. The entanglement based information transfer scheme is depicted in Figure 2.5b. In this case, two quantum modes are involved in the information transfer. Because the state is Gaussian, its quantum noise properties are completely characterized by a 4×4 covariance matrix γ.

Equation (2.18) represents the covariance matrix of a two-mode entangled Gaussian state

$$\gamma = \begin{pmatrix} 1.45 & 0 & 1.05 & 0 \\ 0 & 1.45 & 0 & -1.05 \\ 1.05 & 0 & 1.45 & 0 \\ 0 & -1.05 & 0 & 1.45 \end{pmatrix}, \tag{2.18}$$

as can be produced by overlapping two pure squeezed modes having 4 dB squeezing each on a balanced beam splitter [DHF$^+$07]. Alice and Bob's local modes are described by the sub-matrices

$$\gamma_{\hat{X}_A,\hat{P}_A} = \begin{pmatrix} 1.45 & 0 \\ 0 & 1.45 \end{pmatrix}, \quad \gamma_{\hat{X}_B,\hat{P}_B} = \begin{pmatrix} 1.45 & 0 \\ 0 & 1.45 \end{pmatrix}. \tag{2.19}$$

Figure 2.6 depicts a contour plot of the subsystems. It is readily seen that taken on their own, the observables corresponding to Alice, i.e. $\hat{X}_A$, $\hat{P}_A$ and those corresponding to Bob, i.e. $\hat{X}_B$, $\hat{P}_B$ are uncorrelated and very noisy.

The situation is different if their joint modes are considered. The covariance matrix of

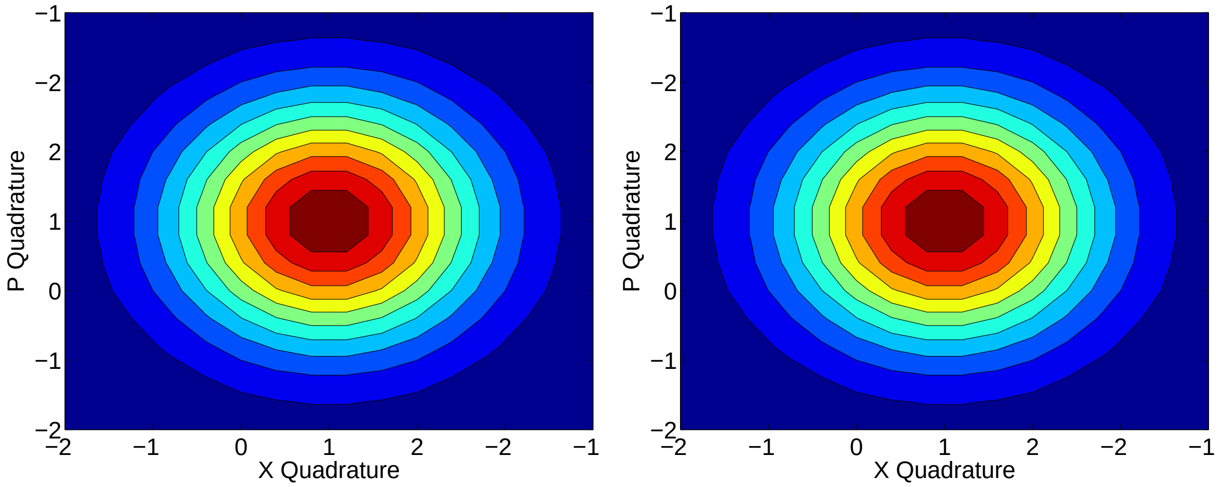

Figure 2.6: Quantum noise projections of local modes: These contour plots depict the quantum noise distributions of Alice and Bob's local modes, i.e. $W(X_A, P_A)$ and $W(X_B, P_B)$. The noise is Gaussian distributed and its variance is larger than than vacuum level, assuming vacuum is set to 1.

this subsystem reads

$$\gamma_{\hat{X}_A,\hat{X}_B} = \begin{pmatrix} 1.45 & 1.05 \\ 1.05 & 1.45 \end{pmatrix}. \tag{2.20}$$

Examining the contour plot, Figure 2.7, reveals that the observables are correlated! Further analysis reveals that not only are the amplitude quadratures correlated but also the phase quadratures, as illustrated by that subsystem

$$\gamma_{\hat{P}_A,\hat{P}_B} = \begin{pmatrix} 1.45 & -1.05 \\ -1.05 & 1.45 \end{pmatrix}. \tag{2.21}$$

At first glance these results seem to be counterintuitive. How can it be that ignorance of ones own local mode implies knowledge of the other party's? Perhaps it was this fact that Erwin Schrödinger had in mind when he coined the term *Verschränkung* and described it in these words:

> Maximalle Kenntnis von einem Gesamtsystem schließt nicht notwendig maximaller Kenntnis aller seiner Teile ein.

which is to say that knowledge of the total system does not necessarily imply knowledge of the subsystems.

An uncertainty relation describing this new state can be derived from two new observables

$$\hat{u} = \hat{X}_A + \hat{X}_B, \quad \hat{v} = \hat{P}_A - \hat{P}_B, \tag{2.22}$$

which are linear combinations of Alice's and Bob's amplitude and phase quadratures, respectively. For the case of an entangled state, the uncertainty relation reads

$$\Delta^2\hat{u}\Delta^2\hat{v} = 0, \tag{2.23}$$

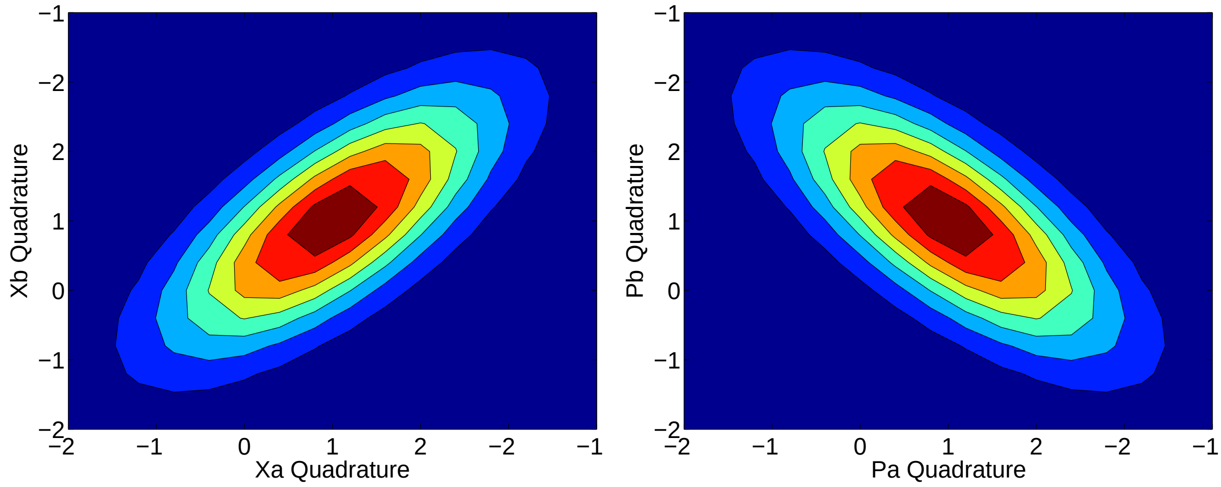

Figure 2.7: Quantum noise projections of joint modes: These contour plots correspond to the joint quadratures between Alice and Bob's amplitude, $W(X_A, X_B)$, and phase quadratures, $W(P_A, P_B)$. The rotation indicates correlation between the respective quadratures and the small width in the one direction indicates reduced noise below the vacuum noise level.

since these operators commute $[\hat{u}, \hat{v}] = 0$. Equation (2.23) implies that the result of a measurement by Bob would reduce the mutual deviation from the mean in the extreme case to zero. At the extreme point, the relative amplitude and phase quadratures with respect to each other would be perfectly defined and Bob could perform an exact measurement.

In the previous section, I introduced entanglement as that quantum state which lends itself to an exact global description but is poorly defined in its individual components. In this section, I will argue that it is exactly this property which makes entanglement useful for information processing tasks. In fact, entanglement is so useful, that by using it as a physical resource for information transfer, not only can one enhance the information transfer potential but one can send both *classical* and *quantum* information.

2.4.2 Carrying Classical Information: Dense Coding

As a first example, I now show how entanglement is used to transfer classical information. The experimental implementation is shown in Figure 2.5b. Both Alice and Bob share one half of a bipartite entangled state. Bob's receives his half at any time before the transmission of the classical information. Alice takes her half and puts a classical modulation in both the amplitude and phase quadratures of the state. These coherent displacements are the classical information to be received by Bob. Upon receiving the second half of the entangled state, Bob mixes the two halves on a balanced beam splitter and performs homodyne detection on each output mode measuring the amplitude quadrature of one of the modes and the phase quadrature of the other mode.

The protocol just described is known as *Dense Coding*. It was first theoretically described by Bennett *et al.* [BW92] for the discrete case and later experimentally implemented by Mattle *et al.* [MWKZ96]. It was later extended to the continuous-variable regime by Braunstein

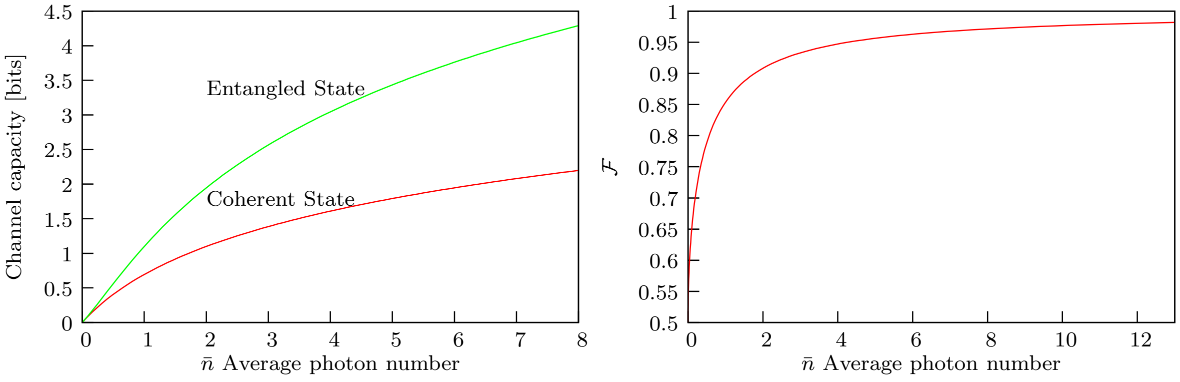

(a) Dense coding channel capacity (b) Teleportation fidelity

FIGURE 2.8: Dense coding and teleportation channel capacities: The capacity of a channel to transmit classical bits as a function of the number of photons in the physical link between the communicating parties is given in Figure(a) for the case of a coherent state as the physical resource, red curve, and for the case of an entangled state as the physical resource, green curve. For non-zero number of photons in the channel, entanglement always represents an increase in the capacity of the channel to transmit classical bits. Figure(b) gives the teleporation fidelity for coherent states also as a function of the average number of photons in the underlying squeezed state. As the squeezing strength increases the fidelity approaches unity.

and Kimble [BK00] and experimentally demonstrated first by Mizuno [MWFS05] in the bipartite case and later by Jing [JZY$^+$03] for the tripartite case.

In order to understand why dense coding works it is best to observe how the quantum noise of the distributed modes is changed during the course of the protocol. This is depicted in Figure 2.9. The first part of the protocol is the "preparation stage". Here, Alice prepares an entangled state and sends one half to Bob while keeping the other. Taken on their own, the noise power or variance of the state is much larger than that of the vacuum fluctuations and grows with increasing entanglement between the two beams. The next stage is the "encoding" stage. Alice places both an amplitude and phase modulation on her half of the entangled state. This results in a coherent displacement in phase space but does not alter the quantum noise power of the state. Upon receiving the second half of the entangled state, Bob mixes them on a balanced beam splitter, performing the "decoding" part of the protocol. Finally, the last stage is the "read-out", where Bob measures both the amplitude and phase quadratures to read off the value of the amplitude and phase modulation.

Notice in this last step that the quantum noise power is now smaller than vacuum fluctuations in both the amplitude and phase quadratures. This reduction in the quantum noise power is a direct result of the quantum correlations which exist between the modes. Consequently, Bob can perform a measurement below vacuum noise level to determine the coding used by Alice. Had Alice and Bob used a coherent state for the transfer, they would have fundamentally been limited by the vacuum fluctuations. This explains at the level of quantum noise the behavior of the channel capacity curves in Figure 2.8. By increasing the amount of entanglement in the state, and thereby reducing the uncertainty in Bob's measurement in the "read-out" stage of the experiment, Alice is able to increase the information carrying

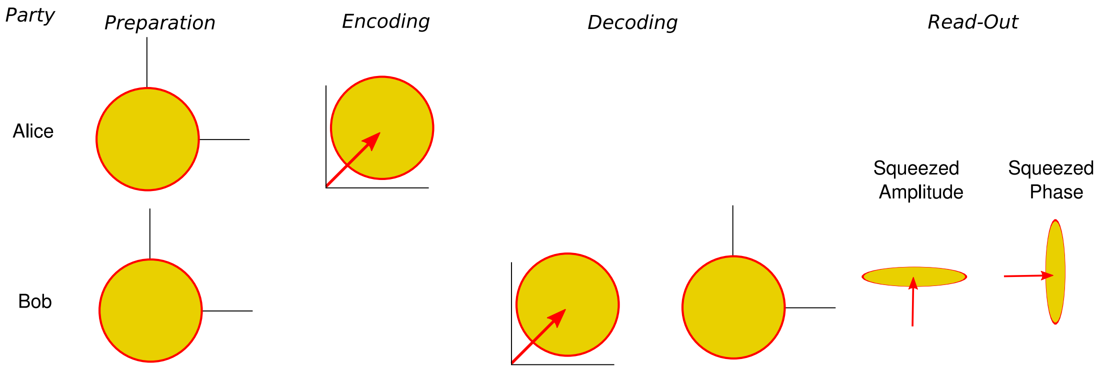

FIGURE 2.9: Carrying classical information: The dense coding protocol can be divided into four stages. In the preparation stage, Alice sends one half of a two-mode squeezed state to Bob and retains the other. In the encoding stage, Alice applies both a phase and amplitude modulation to her half and sends it to Bob. The decoding stages involves Bob mixing his half of the two-mode state with the now modulated half he receives from Alice. Finally, in the read-out stage, Bob measures both the amplitude and phase quadratures of the state. Due to the quantum correlations between Alice's and Bob's states, Bob can perform two below vacuum level measurements.

capacity of her channel beyond that possible with non-entangled states. In terms of the three characteristics of an information transfer system described in Section 2.3.1, the simultaneously "squeezing" of the amplitude and phase quadratures increases the distinugishability of the message components.

2.4.3 Carrying Quantum Information: Teleportation

While increasing the classical capacity of a communication channel is certainly impressive, entanglement offers even more. Shared entanglement can be used to reliably and unconditionally transport *quantum* information! What is meant by quantum information is some *unknown* quantum state ρ that Alice would like to send Bob. The protocol to perform such a transfer was first developed by Bennett*et al.* [BBC$^+$93] for qubits and given the name "teleportation" since the quantum state at the sender station is completely destroyed in the process of the protocol and appears at a far away location perfectly intact. Teleportation was extended to the continuous-variable (CV) regime by Braunstein and Kimble [BK98] and experimentally demonstrated by various groups [BTB$^+$03b, BTB$^+$03a, YBF07, TAK$^+$05].

The basic protocol for CV teleportation is depicted in Figure 2.10. Again, Alice and Bob share a two-mode squeezed state. Alice mixes the unknown quantum state ρ with her half of the entangled state and measures the amplitude and phase quadratures on the output modes of the beam splitter. She then sends the results of this measurement to Bob over a classical channel. Bob takes these results and displaces his half of the entangled state depending on the results of Alice's measurement thus completing the protocol.

The reason why teleportation works can be understood once again by examining the quantum noise of all states involved in the protocol in phase space as depicted in Figure 2.11. The protocol begins similarly to dense coding where first Alice prepares an entanglement

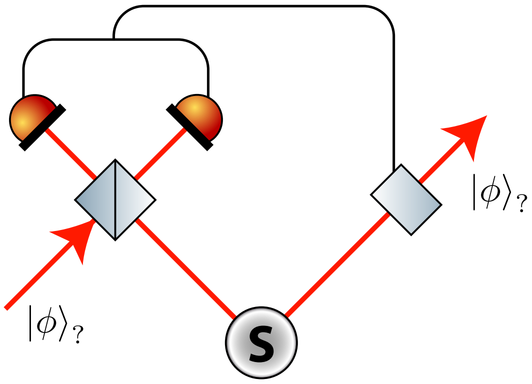

FIGURE 2.10: Experimental setup for teleportation: This figure is a schematic representation of an experimental setup for teleporting an unknown quantum state. Both communicating parties share one half of a bipartite entangled state created from some source "S". The sender mixes the unknown quantum state with their half of the entanglement and performs a simultaneous measurement of the amplitude and phase quadratures on the output modes. The results of this measurement are sent by means of a classical communication channel to the receiver and is used to perform a unitary operation on their half of the entangled state. At this point the teleportation is complete.

resource, one half of which stays with Alice. After combining the unknown state with her half of the entangled state, Alice measures both the amplitude and phase quadratures of the modes at the output of the beam splitter. At this point, Alice has only has the quantum noise fluctuations according to the unknown state to be teleported. Finally, she sends the results of her measurement to Bob who performs a displacement in phase-space obtaining the original state.

The "displacement" stage of the teleportation protocol is important because, as a result of performing a measurement on her half of the entanglement resource, Alice induces a random displacement in phase-space which is equal to the result of Alice's measurement. Bob cannot known *a priori* how his state will be displaced. This information comes from Alice who performs the measurement and utilizes the fact that their shared state is entangled. The quality of the teleportation is measured by a quantity known as the fidelity, $\mathcal{F}$. It is a measure of how much of the original state is faithfully teleported. Figure 2.8b illustrates the dependence of the fidelity on the amount of squeezing in the underlying entangled state. This squeezing is important because Alice adds one unit of vacuum noise into the state by trying to simultaneously measure the amplitude and phase quadratures. This additional noise is suppressed by the shared entanglement between Alice and Bob.

2.5 Distillability and Information: Bound Entanglement

The previous two sections showed that entanglement is superior in transmitting both classical and quantum information. The ability to perform these tasks depends directly on the amount

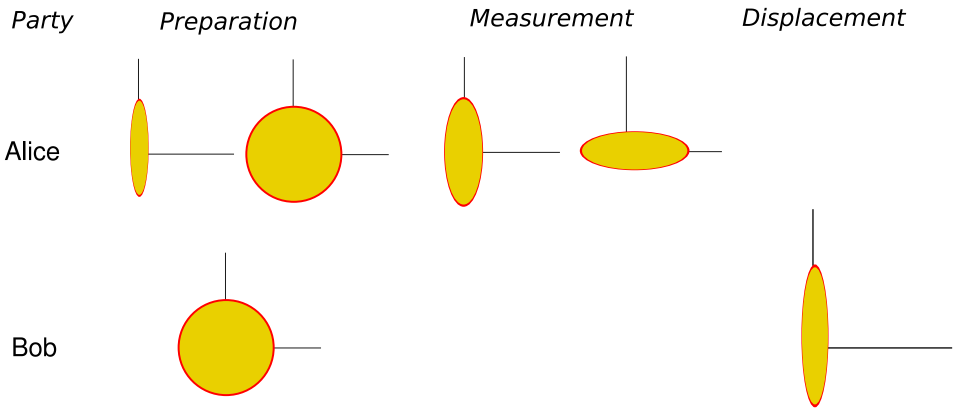

FIGURE 2.11: Carrying quantum information: The teleportation protocol can be understood by following how the quantum noise distribution changes with each step. In the preparation stage of the protocol, Alice possess one half of a bipartite entangled state, depicted here by the large yellow ball and some unknown state which, for example purposes, has been chosen to be a squeezed state. Bob has the other half of the entangled state and is exactly the same as Alice's. In the measurement stage of the protocol, Alice projects Bob's half of the entangled state onto the unknown state. The final stage of the protocol is the displacement state, where Bob applies a unitary transformation on his half of the entangled state depending on the results of the measurement performed by Alice. He now has the unknown state.

of entanglement present in the underlying state. This raises an immediate question: is it possible to increase the initial amount of entanglement in any given state? The answer is a qualified yes!

The method by which the entanglement of a state can be increased is known as *distillation*. Starting with several copies of a weakly entangled state shared between Alice and Bob, they perform a series of operations on their respective parts, discussing each step as they move along. After they are finished, the result is a smaller number of more highly entangled states which can then be used to perform teleportation.

There are, however, a class of quantum states which although entangled, cannot be distilled. These special states are known as *bound entangled* states in analogy with bound energy in thermodynamics [HH98].

Since bound entangled states were first introduced by the Horodecki family [HH98] a theoretical work has been performed in characterizing these states [WW01, GKD$^+$01]. Despite the growth in theoretical knowledge concerning bound entanglement, there has been limited experimental progress in the preparation of these states. In this thesis, I present the first unconditional generation and characterization of bound entangled states of light. I will demonstrate the feasibility of generating these states using current technology and show how these states can be steered between being bound, separable and free entangled. In the next chapter I treat the more technical aspects of entanglement theory and provide all of the theoretical tools necessary in order to understand the remainder of this thesis.

3

Free Entanglement

In this chapter I discuss the theoretical foundations of characterizing entangled states. The theory of entanglement can be divided into three main topics: separability, measurability and distillability. Separability deals with establishing criteria to determine whether a state is entangled; measurability is concerned with quantifying the amount of entanglement; and distillability deals with developing both criteria and protocols to extract from several copies of a weakly, possibly mixed entangled state, fewer copies of pure, more strongly entangled states. I treat each of these topics in turn, introducing and implementing several criteria and measures that are currently known.

There exists a connection between separability and distillability first identified by Horodecki *et al.* [HH98] in the context of mixed-state entanglement distillation. They showed that the Peres non-positive partial transpose (NPT) criterion is a sufficient criterion for distillability [HH99]. Later, Giedke *et al.* presented necessary and sufficient conditions for distillability and separability showing that for Gaussian $n \times m$ states a negative partial transpose is necessary and sufficient for distillabillity [GKLC01a]. Inseparability, however, does not imply distillability and for this reason inseparable quantum states can be classified as being NPT or PPT entangled, the former corresponding to those states which can be distilled. This chapter concerns itself exclusively with npt entanglement.

3.1 The Separability Problem

Given an arbitrary quantum state, ρ, the separability problem involves developing criteria such that separable states can be distinguished from inseparable states. By inseparability it is meant that a composite system ρ_{AB} cannot be written as convex sum of product states

$$\rho = \sum_k w_k \rho_{kA} \otimes \rho_{kB}, \tag{3.1}$$

where w_k are statistical weights which sum to one and ρ_{kA} , ρ_{kB} correspond to the individual subsystems, respectively [Wer89, BvL05]. In identifying this property, entanglement criteria utilize key features of either states or observables. The first criterion I will introduce is known as the *Peres-Horodecki* criterion.

3.1.1 Peres-Horodecki: NPT Entanglement

The Peres-Horodecki criterion, also known as the nonpositive partial transpose (NPT) criterion, was first introduced by Peres for the case of discrete variables [Per96]. The necessity and sufficiency of the criterion was proven by Horodecki *et al.* for discrete systems of dimension 2×2 and 2×3 and later by Simon [Sim00] in the Gaussian continuous-variable regime. The NPT criterion is based on two fundamental properties of quantum states

$$\begin{aligned} \rho &\geq 0, \\ \mathrm{Tr}\,(\rho) &= 1, \end{aligned} \tag{3.2}$$

where the inequality is understood to reference the eigenvalues of the density matrix. The first property is known as "positivity" and ensures that all eigenvalues in every basis as well as the diagonal elements of the matrix itself remain positive. The second property prevents any individual diagonal element from being greater than one. These two features enable the probabilistic interpretation of quantum mechanics and must hold for all bona fide quantum states [HH99].

The positivity condition also places a restriction on the type of physical operations that can be performed on quantum systems

$$T(\rho) \geq 0. \tag{3.3}$$

Equation (3.3) demands that any operator, T, representing a physical operation must be positive, i.e. transform positive density matrices into positive density matrices. For composite systems, Equation (3.3) reads

$$(T \otimes I)\rho_{AB} \geq 0, \tag{3.4}$$

and its effect on separable states such as those described by Equation (3.1) is given by

$$(T \otimes I)\,\rho_{AB} = \sum_k w_k T\,(\rho_A) \otimes \rho_B \geq 0, \tag{3.5}$$

since the unity operator has no effect on the subsystem ρ_B and $T(\rho_A) \geq 0$ due to the positivity of T. Note that the only requirement placed on T is that it be positive. There are, however, a whole class of states for which Equation (3.4) is violated. These are "entangled" or "inseparable" states which cannot be written in the form of Equation (3.1). Equation (3.4) therefore provides a *necessary* condition for separability [Per96, HH99]. It was Peres who first suggested using partial transposition as the positive operator in Equation (3.4) and for that reason the criterion is known as the nonpositive partial transpose (NPT).

I introduced the NPT criterion in terms of density matrices but it works equally well for covariance matrices. The positivity condition, $\rho \geq 0$, for covariance matrices is

$$\gamma + i\Omega \geq 0, \tag{3.6}$$

where γ is a symmetric $2N \times 2N$ covariance matrix for N modes and Ω is the symplectic form given by

$$\Omega = \begin{pmatrix} \sigma & 0 \\ 0 & \sigma \end{pmatrix}, \tag{3.7}$$

with

$$\sigma = \begin{pmatrix} 0 & 1 \\ -1 & 0 \end{pmatrix}. \tag{3.8}$$

Equation (3.6) is an expression of the Heisenberg uncertainty relation [SSM87, SMD94] and is satisfied for all covariances matrices representing bona fide quantum states. Positivity under partial transposition is checked by changing the sign of the phase quadrature of a single mode or in matrix form by $\Gamma_a \gamma \Gamma_a$ where $\Gamma_a = \mathrm{diag}\,(1\,, -1\,, 1\,, -1\ldots)$. The necessary and sufficient condition for separability of Gaussian states then reads [Sim00]

$$\gamma^{T_A} + i\Omega \geq 0, \tag{3.9}$$

where the transposition is taken to act on Alice's momenta.

To illustrate the NPT criterion I present the case of a bipartite entangled Gaussian state. Assuming pure states and 4 dB squeezing in the underlying squeezed states, the covariance matrix of such a state is given by

$$\gamma = \begin{pmatrix} 1.45 & 0 & 1.05 & 0 \\ 0 & 1.45 & 0 & -1.05 \\ 1.05 & 0 & 1.45 & 0 \\ 0 & -1.05 & 0 & 1.45 \end{pmatrix}. \tag{3.10}$$

Applying the NPT criterion yields

$$\min\left(\mathrm{eig}\left(\gamma^{T_a} + i\Omega\right)\right) = -0.4, \tag{3.11}$$

a clear violation of Equation (3.9).

Multiparty Implementation

The NPT criterion can also be applied to cases where there are more than two parties. It establishes a hierarchy of multipartite entangled states where partial transposition is applied to a specific mode denoted by symbol T_n, n corresponding to the mode [GKLC01a]. To illustrate this, I list the various ways in which the NPT criterion can be applied to a tripartite three-mode Gaussian state. The hierarchy of entangled states is achieved by forming five different classes. A state is said to belong to a specific class if all of the conditions of that class are satisfied. The five possible classes for three-mode tripartite entangled states are given by

class 1:

$$\gamma^{T_1} + i\Omega \ngeq 0 \qquad \gamma^{T_2} + i\Omega \ngeq 0 \qquad \gamma^{T_3} + i\Omega \ngeq 0, \tag{3.12}$$

class 2:

$$\gamma^{T_k} + i\Omega \geq 0 \qquad \gamma^{T_m} + i\Omega \ngeq 0 \qquad \gamma^{T_n} + i\Omega \ngeq 0, \tag{3.13}$$

class 3:

$$\gamma^{T_k} + i\Omega \geq 0 \qquad \gamma^{T_m} + i\Omega \geq 0 \qquad \gamma^{T_n} + i\Omega \ngeq 0, \tag{3.14}$$

class 4 or 5:

$$\gamma^{T_1} + i\Omega \geq 0 \qquad \gamma^{T_2} + i\Omega \geq 0 \qquad \gamma^{T_3} + i\Omega \geq 0, \tag{3.15}$$

where the partial transposition is applied to the phase quadrature of the specified mode. The five classes have the following interpretation as elaborated upon by Braunstein and van Loock [BvL05]. Class 1 corresponds to the case of fully inseparable states for any partition of the modes. Class 2 describes the one mode biseparable states, meaning that only one mode is separable from the remaining two modes. Class 3 means that two bipartite splittings of separable states are possible whereas class 4 corresponds to the case of three-mode biseparable states which cannot be written as a mixture of three mode product states. It should be noted that for classes 2 and 3 all permutations of the three modes (k, m, n) must be considered. Finally, class 5 corresponds to the fully separable states such that $\gamma \geq \gamma_1 \oplus \gamma_2 \oplus \gamma_3$ where γ_i corresponds to the one mode correlation matrix.

In order to implement the NPT criterion either the density matrix or the covariance matrix must be measured. For infinite dimensional systems, such as for optical modes, measurement of the density matrix is a challenging experimental task. The covariance matrix, however, can be easily measured using fewer settings then has been performed by many researchers [BSLR04, LKOH$^+$05, WOTBG05, DHF$^+$07] as I will explain in Chapter 7. There are circumstances under which even measuring the covariance matrix requires too many measurement settings. Inseparability can still be ascertained using the Duan criterion and is the topic of the next section.

3.1.2 Duan Criterion

The strategy behind the NPT criterion was to identify those states that fail to retain their physicality under a specific operation. This leads to partial transposition and the realization that density matrices / covariance matrices of entangled states fail to remain physical under this operation. A different approach to the same problem is to exploit the linearity and hermiticity of operators representing observables to separate the class of separable from inseparable states.

The Linearity Property

Before I demonstrate how these two features of quantum theory can be used to solve the separability problem, I first want to review their definitions. Beginning with linearity, a generic operator, $\hat{A}$, is defined to be linear if its action on a linear combination of arbitrary functions, Ψ_i is given by

$$\hat{A}\left(\alpha_1\Psi_1 + \alpha_2\Psi_2 \ldots \alpha_i\Psi_i\right) = \hat{A}\alpha_1\Psi_1 + \hat{A}\alpha_2\Psi_2 \ldots \hat{A}\alpha_i\Psi_i. \tag{3.16}$$

Linearity is also important because it adds an extra restriction on the operators such that the order in which multiple operators can be applied to a function is governed by a quantity known as the *commutator*

$$[\hat{A}\,,\,\hat{B}] \equiv \hat{A}\hat{B} - \hat{B}\hat{A}. \tag{3.17}$$

Operators for which the commutator is zero are said to “commute” and can be applied in any order to a function ψ.

The Hermitian Property

The second fundamental property quantum theory imposes on observables is hermiticity. The defining feature of a Hermitian operator is that its conjugate transpose is the operator itself

$$\hat{A}^\dagger = \hat{A}, \tag{3.18}$$

where the dagger represents complex conjugation and transposition. The Hermitian requirement on observables in quantum theory has both physical and algebraic consequences. The physical consequence of Hermiticity is that expectation values calculated from a complex-valued wavefunction ψ are guaranteed to be real-valued.

The algebraic consequence of hermiticity is that two inequalities must be satisfied; namely, the *Cauchy-Schwarz Inequality*

$$\left|\langle\hat{A}\mid\hat{B}\rangle\right| \leq \left|\langle\hat{A}\rangle\right|\left|\langle\hat{B}\rangle\right|, \tag{3.19}$$

and the *Triangle Inequality*

$$\langle\Delta^2\hat{A}\rangle_\rho + \langle\Delta^2\hat{B}\rangle_\rho \geq \left|\left[\hat{A}\,,\,\hat{B}\right]\right|, \tag{3.20}$$

which is presented here in terms of variances of observables.

I will now show how hermiticity and linearity can be combined to derive an entanglement criterion. To begin with, let us define a set of Hermitian operators which may be a linear combination of other such operators

$$\hat{u} = a_1\hat{x}_1 + a_2\hat{x}_2, \quad \hat{v} = b_1\hat{p}_1 + b_2\hat{p}_2, \tag{3.21}$$

where the constants a_i, b_i are real-valued and $\hat{x}_i, \hat{p}_i$ are assumed to be Hermitian operators. The first case to consider is the constraint that any bona fide quantum state must satisfy. For this case, the Equation (3.20) can be applied directly resulting in [GMVT03]

$$\langle\Delta^2\hat{u}\rangle_\rho + \langle\Delta^2\hat{v}\rangle_\rho \geq \left|a_1b_1\left[\hat{x}_1\,,\,\hat{p}_1\right] + a_2b_2\left[\hat{x}_2\,,\,\hat{p}_2\right]\right|, \tag{3.22}$$

where the commutator $[\hat{u}\,,\,\hat{v}]$ has been evaluated using the identity

$$\left[\hat{A}\,,\,\hat{B}+\hat{C}\right] = \left[\hat{A}\,,\,\hat{B}\right] + \left[\hat{A}\,,\,\hat{C}\right]. \tag{3.23}$$

Equation (3.22) establishes a set of inequalities for all possible values of the coefficients that must be satisfied if the density matrix ρ is to be considered a genuine quantum state [GMVT03].

The next step is to add the further restriction that the state be separable (Equation (3.1)) and again calculate the sum of the variances

$$\langle \hat{u}^2 \rangle_{\rho_{\text{sep}}} = \langle \big(a_1^2 \hat{x}_1^2 + a_2^2 \hat{x}_2^2 + 2 a_1 a_2 \hat{x}_1 \hat{x}_2 \big) \sum_k w_k \rho_{k1} \otimes \rho_{k2} \rangle, \tag{3.24}$$

and

$$\langle \hat{v}^2 \rangle_{\rho_{\text{sep}}} = \langle \big(b_1^2 \hat{p}_1^2 + b_2^2 \hat{p}_2^2 + 2 b_1 b_2 \hat{p}_1 \hat{p}_2 \big) \sum_k w_k \rho_{k1} \otimes \rho_{k2} \rangle. \tag{3.25}$$

The rest of the steps in the calculation can be found in [GMVT03, DGCZ00, vLF03] and only the final result will be presented here

$$\langle \Delta^2 \hat{u} \rangle_{\rho_{\text{sep}}} + \langle \Delta^2 \hat{v} \rangle_{\rho_{\text{sep}}} \geq |a_1 b_1| \, |\langle [\hat{x}_1 \, , \, \hat{p}_1] \rangle| + |a_2 b_2| \, |\langle [\hat{x}_2 \, , \, \hat{p}_2] \rangle| \, . \tag{3.26}$$

Equation (3.26) is a tighter bound than Equation (3.22) [GMVT03]. This same result was first derived by Duan *et al.* [DGCZ00] and shown to be a sufficient condition for inseparability of all continuous-variable states and both necessary and sufficient for Gaussian states. As an example of its application, I will set the coefficients equal to 1 and define the commutator to be

$$[\hat{x}_i \, , \, \hat{p}_j] = 2 i \delta_{ij}. \tag{3.27}$$

The separability criterion, Equation (3.26), becomes

$$\langle \Delta^2 \hat{u} \rangle_{\rho_{\text{sep}}} + \langle \Delta^2 \hat{v} \rangle_{\rho_{\text{sep}}} \geq 4. \tag{3.28}$$

Any violation of this inequality is sufficient for the presence of entanglement. This criterion has the advantage over the NPT criterion in that it requires only a minimal number of measurements to check for separability of the underlying state. It is especially useful in the multipartite regime, where only a few measurement settings are required to obtain the variances contained in the inequalities.

Duan's Multipartite Extension

The Duan criterion can be extended in a similar fashion to the NPT criterion to the case of multiple parties and multiple modes. The general strategy for deriving the criteria was developed by van Loock and Furusawa [vLF03] and comprises the following steps: first the quadratures $\hat{x}_i$ and $\hat{p}_i$ are measured and combined into linear combinations. Second, the variances of these combinations are calculated and checked against necessary conditions for partial separability. Two important factors must be taken into account when forming the linear combinations: the total variances for all partially separable states must be nonzero and the commutators for the combinations must vanish. As an example calculation, van Loock calculates a set of inequalities for a continuous-variable Greenberger-Horne-Zeilinger (GHZ) state [vLF03]. They read

$$\langle \Delta^2 (\hat{x}_1 - \hat{x}_2) \rangle + \langle \Delta^2 (\hat{p}_1 + \hat{p}_2 + \hat{p}_3) \rangle \geq 1, \tag{3.29}$$

$$\langle \Delta^2(\hat{x}_2 - \hat{x}_2)\rangle + \langle \Delta^2(\hat{p}_1 + \hat{p}_2 + \hat{p}_3)\rangle \geq 1, \tag{3.30}$$

$$\langle \Delta^2(\hat{x}_1 - \hat{x}_3)\rangle + \langle \Delta^2(\hat{p}_1 + \hat{p}_2 + \hat{p}_3)\rangle \geq 1. \tag{3.31}$$

These conditions are necessary for different kinds of partial separability and the violation of any pair of inequalities is sufficient for genuine three-party entanglement. This is because, as pointed out by van Loock, the only assumptions in the derivation leading to the inequalities Equation (3.31) are the Heisenberg uncertainty relation and the Cauchy-Schwarz inequality.

3.1.3 Separable Matrices

The final criterion that I present is the method of separable matrices. The idea behind this criterion is to directly use the definition of separability as the criterion for entanglement rather than exploit some other feature of the state that would imply separability. The definition of a separable quantum state was given to be in terms of density matrices

$$\rho = \sum_k w_k \rho_{k1} \otimes \rho_{k2}. \tag{3.32}$$

In terms of covariance matrices Equation (3.32) reads [WW01]

$$\gamma \geq \gamma_A \otimes \gamma_B. \tag{3.33}$$

The goal of this method is to try and find two covariance matrices, γ_A and γ_B, such that Equation (3.33) is satisfied. A method to do this was developed by Giedka *et al.* [GKLC, GKD$^+$01] and is summarized here.

The first step is to arrange the global $2N \times 2N$ covariance matrix into block form

$$\gamma = \begin{pmatrix} \mathbf{A} & \mathbf{C} \\ \mathbf{C}^T & \mathbf{B} \end{pmatrix}, \tag{3.34}$$

where $\dim(\mathbf{A}) = 2l \times 2l$, $\dim(\mathbf{B}) = 2k \times 2k$ and $\dim(\mathbf{C}) = 2l \times 2k$, with l and k specifying the number of modes that Alice and Bob possess. Once the block structure is in place the following iterative procedure is applied

$$\begin{aligned} \mathbf{A}_{N+1} &\equiv \mathbf{B}_{N+1} \equiv \mathbf{A}_N - \mathrm{Re}\,(X_N)\,, \\ \mathbf{C}_{N+1} &\equiv -\mathrm{Im}\,(X_N)\,, \end{aligned} \tag{3.35}$$

where $X_N \equiv \mathbf{C}_N\left(\mathbf{B}_N - iJ\right)^{\mathrm{MP}}\mathbf{C}_N^T$ and “MP” stands for the Morse-Penrose pseudoinverse. The iterative procedure is repeated until either

$$\mathbf{A}_N \ngeq iJ, \tag{3.36}$$

or

$$\mathbf{L}_N \equiv \mathbf{A}_N - |\mathbf{C}_N| \geq iJ. \tag{3.37}$$

This criterion was shown to be both necessary and sufficient for all Gaussian states [GKLC01b]. Since the criterion does not use partial transposition it can detect a larger class of Gaussian entangled states.

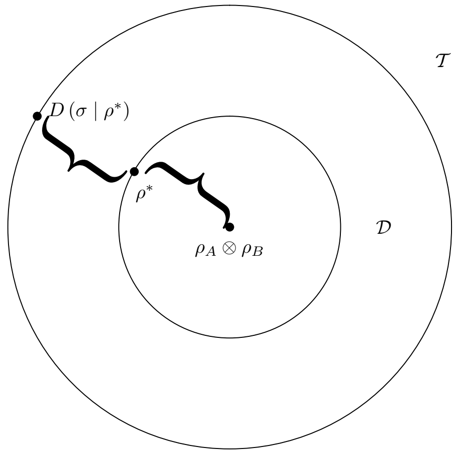

FIGURE 3.1: Distance measure of entanglement: The idea behind this class of entanglement measures is to find the minimum distance from the measured state, σ, to the next nearest separable state, ρ^* using some measure of distance, D. The larger this distance, the more entangled the state. This measure suffers from the drawback that the measured state must be compared against all possible separable states.

3.2 The Measurability Problem

The ability to distinguish between separable and inseparable states is important for quantum information science since many of the protocols require an entangled resource in order to enhance the capabilities beyond a classical resource, e.g. dense coding or to work at all, e.g. teleportation. It was shown in Section 2.4.2 using the examples of dense coding and teleportation, that not only is the presence of entanglement required but also large amounts of it. Quantifying the statement "large amounts" is the topic of the "measurablility problem".

A number of entanglement measures have been developed over the years in both the discrete qubit and continuous-variable regimes. In addition to developing measures themselves, there has been work in trying to develop a theoretical framework from within which new measures of entanglement can be derived and existing measures can be justified [VPRK97, SV]. The details involved in this research program are very technical and beyond the scope of this thesis. In the following sections, I will give an overview of entanglement measures by grouping them into three broad categories: *distance measures*, *operational measures*, and *utility measures*.

3.2.1 Distance Measures

The entanglement measures within this category are the most intuitive. The idea behind a distance measure is depicted in Figure 3.1. The set of all "disentangled" or separable density matrices $\mathcal{D}$ is considered as a subset of the set of all physically admissible density matrices, $\mathcal{I}$. Given some quantum state σ, whose entanglement properties are under investigation, the goal of a distance measure is to quantify the minimum distance between the potentially entangled state σ and some known separable state ρ^*. The problem can be formally stated as follows

$$E(\sigma) \equiv \min_{\rho \in \mathcal{D}} D\left(\sigma || \rho\right), \tag{3.38}$$

where D is any admissible measure of distance and $E(\sigma)$ measures the remaining quantum mechanical correlations [VPRK97]. Some applicable measures of distance include the Kullback-Leibler distance and the von Neumann relative entropy. A major drawback of this measure is that the minimization in Equation (3.38) must be performed over all separable states. It therefore cannot be feasibly computed in all but the smallest dimensional cases. In comparison, the next category of entanglement measures contains some computable measures which have been used in numerous experimental settings.

3.2.2 Operational Measures

Operational measures of entanglement are those that do not necessarily posses a physical meaning but nonetheless are capable of establishing some type of hierarchy amongst entangled states. The most relevant of these measures for continuous-variable systems is the logarithmic negativity (LN), $E_{\mathcal{N}}$[VW02]. The LN is based on the NPT criterion described in Section 3.1.1 and measures the degree to which a partially transposed density matrix fails to be positive. It is defined by

$$E_{\mathcal{N}}(\rho) \equiv \| \log_2 \rho^{T_A} \|_1, \tag{3.39}$$

where $\|.\|_1$ denotes the trace-norm of a matrix.

One advantage of the LN is that even for continuous-variable systems the quantity $E_{\mathcal{N}}$ can be computed. The computation is especially easy if the state is Gaussian. Then, as I pointed out in Chapter 2, the finite dimensional covariance matrix provides the complete description of the state. A further simplification is obtained by realizing that the symplectic eigenvalues of a covariance matrix, ν_i, describe all properties of the state. The LN for Gaussian states can then be computed by

$$E_{\mathcal{N}}(\gamma^{T_A}) = \max[0, -\log_2 \nu_i], \tag{3.40}$$

where in this case ν_i is the smallest positive symplectic eigenvalue [AI05].

As an illustration of its usefulness, the logarithmic negativity was used by DiGuglielmo *et al.* to quantify the amount of entanglement for different classes of continuous-variable entangled states [DHF$^+$07]. It was also used by Fiurášek *et al.* in the context of entanglement distillation and purification as a measure of entanglement even though the state was no longer Gaussian [FFS07].

The use of the LN is mostly due to its computability, it possesses no direct physical interpretation. There is, however, another category of entanglement measures, which do possess a direct physical interpretation and can be calculated for certain Gaussian states. This last category is the topic of the next section.

3.2.3 Utility Measures

Measures belonging to this group are constructed with the explicit view of the underlying states' usefulness for quantum information processing. Two examples of these measures are

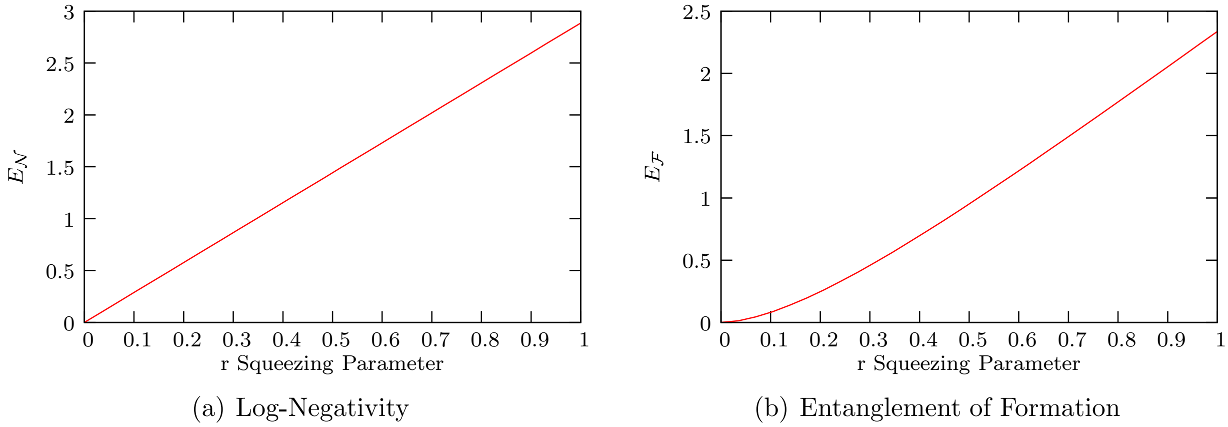

(a) Log-Negativity (b) Entanglement of Formation

FIGURE 3.2: Comparison of the $E_{\mathcal{N}}$ and $E_{\mathcal{F}}$: These two graphs plot the log-negativity, Figure(a), and entanglement of formation, Figure(b), for a bipartite symmetric two-mode squeezed Gaussian state. The squeezing strength of both of the underlying squeezed modes is measured by the squeezing parameter, r, and corresponds to the abscissa. The ordinate corresponds to the respective measure of entanglement. Both are based on the PPT criterion for separability and quantify the degree of entanglement by the smallest symplectic eigenvalue of the partially transposed covariance matrix.

the Entanglement of Formation (EoF) $E_{\mathcal{F}}$ and the Entanglement of Distillation (EoD), $E_{\mathcal{D}}$. The EoF was first introduced by Bennett *et al.* [BDSW96] and quantifies the minimum number of pure maximally entangled states needed to construct the entangled state through local operations and classical communication (LOCC). It is formally defined by

$$E_{\mathcal{F}}(\rho) \equiv \min_{p_i|\Psi\rangle_i} \sum_i p_i E(|\Psi\rangle_i), \tag{3.41}$$

where the minimum is taken over all pure state realizations of the entangled state ρ, i.e. $\rho = \sum_i p_i |\Psi\rangle_{ii}\langle\Psi|$ and E corresponds to the von Neumann entropy. For symmetric two-mode Gaussian states the EoF can be computed exactly and is given by

$$E_{\mathcal{F}}(\gamma^{T_A}) \equiv \max[0, h(\nu_i)], \tag{3.42}$$

where

$$h(\nu_i) = \frac{(1+x)^2}{4x} \log\left(\frac{(1+x)^2}{4x}\right) - \frac{(1-x)^2}{4x} \log\left(\frac{(1-x)^2}{4x}\right), \tag{3.43}$$

and the logarithm is taken to have a convenient basis [AI05]. Figure 3.2a-b are graphs of the LN and EoF for various two-mode pure symmetric Gaussian entangled states, respectively. The abscissa is the squeezing parameter and the ordinate the values of both the LN and EoF in units of bits. Both entanglement measures are monotonic in the symplectic eigenvalue ν.

The entanglement of distillation is defined similarly to the entanglement of formation but quantifies the maximal number of pure entangled states that can be distilled from multiple copies of a weakly, possibly mixed entangled state. If the underlying entangled state is pure, then $E_{\mathcal{D}} = E_{\mathcal{F}}$. As I will discuss in Section 4.3, this is because pure states enable reversible entanglement transformations and therefore provide a unique measure of entanglement.

3.3 The Distillability Problem

The fundamental question behind the distillability problem is to determine how much, if any, strongly entangled states can be extracted from a number of weakly entangled states. The problem is of practical importance since in quantum communication protocols, such as teleportation and quantum key distribution [NA05], the degree of entanglement has an enabling and enhancing effect. The simplest approach is single-copy distillation whereby a local quantum filter is applied to one part of the shared entangled state [BBPS96, DLH$^+$08]. A more sophisticated approach is one that uses local interference of two copies of the entangled states [EBSP04, FFS07]. Entanglement distillation has already been experimentally demonstrated by a number of groups [HSD$^+$08, DLH$^+$08, KBLSG01]. Hage *et al.* have demonstrated the distillation of entangled states against phase-noise decoherence for both the single-copy protocol [HSD$^+$08] as well as iteratively [HSD$^+$10]. These protocols have been performed on states known to be distillable.

The distillability problem has been completely solved for the case of Gaussian states. It was shown in [GKD$^+$01] that a necessary and sufficient condition for distillability of arbitrary bipartite $n \times m$ mode Gaussian states is the NPT criterion. This establishes a relationship between the separability problem and the distillability problem for Gaussian states since the negativity of the partial transpose is both a necessary and sufficient entanglement criterion for Gaussian states of $1 \times N$ and 1×1 modes. It is even tempting to argue that inseparability implies distillability. This is, however, not the case. There is a whole class of Gaussian entangled states which remain positive under partial transposition yet remain inseparable. These states are said to be *bound* entangled and are the topic of the next chapter.

3.4 Summary

In this chapter I discussed the three main problems of entanglement theory, separability, measurability and distillability. There are a number of criteria which can be used to detect inseparable states, the Peres-Horodecki (NPT) criterion being the most commonly used. The NPTcriterion is both a necessary and sufficient criterion for the distillability of $N \times M$ Gaussian entangled states. Finally, measuring the amount of entanglement is motivated by either quantifying the degree of non-positivity of the state, i.e. log-negativity, or by utilizing the interchangeability of entanglement from pure highly entangled states to pure arbitrarily entangled states.

4

Bound Entanglement

In this chapter, I lay the groundwork for the experimental preparation of bound entangled states. Within the overall framework of entangled states, bound entangled states are a special example of "mixed-state" entanglement. They were first discovered by Horodecki [HH98] in the context of distillation and mixed-state entanglement. This was also the first time the connection between positivity under partial transposition and distillability was identified. There it was shown that although bound entangled states are in fact inseparable, they remain positive under the Peres-Horodecki criterion. It is for this reason that entanglement can be divided into two broad types, "NPT" entanglement or "PPT" entanglement. PPT entangled states have also been analyzed in the continuous-variable regime, especially for Gaussian states [WW01, GKD$^+$01] and have been shown to be useless for quantum key distribution [NA05].

Although their non-distillability is interesting on its own, it was Horodecki who drew an analogy between the different types of entanglement and the different types of energy in thermodynamics. They referred to NPT entanglement as "free entanglement" and associated it with *work* since it can be used to perform quantum communication tasks. PPT entanglement was referred to as "bound entanglement" in association with *heat* or bound energy since no useful quantum communication task can be performed with these states. This turns out to be more than just an analogy. The generation of bound entanglement requires the consumption of free entanglement but from which no free entanglement can be distilled, thereby describing an irreversible process. Much of this chapter corresponds to work to be published [DSH$^+$10] as well as colaborative work with Pineda [Pin].

4.1 Criteria for Bound Entanglement

Verifying that a Gaussian state is bound entangled requires that the state satisfy two conditions:

- The state is PPT, i.e. $\gamma^{T_A} + i\Omega \geq 0$.
- The state is inseparable, i.e. $\gamma_{AB} \ngeq \gamma_A \oplus \gamma_B$.

4.1.1 PPT Condition

A covariance matrix γ is said to be PPT if its partial transpose is also a legitimate covariance matrix. Equivalently, this means that

$$\gamma^{T_A} + \mathrm{i}\Omega \geq 0, \tag{4.1}$$

where γ^{T_A} is the partially transposed matrix with respect to the modes A, and Ω is the symplectic form as defined in Section 3.1.1. One criterion to measure the "PPTness" corresponds to the smallest eigenvalue of the matrix in Equation (4.1). It is therefore appropriate to define

$$P(\gamma) = \min \mathrm{eig}\left(\gamma^{T_A} + \mathrm{i}\Omega\right). \tag{4.2}$$

The larger the value of $P(\gamma)$, the more PPT γ will be, i.e. the farther from *any* distillable state.

4.1.2 Inseparability Condition

The check for inseparability is more intricate but can be accomplished for Gaussian states, in contrast to the general case, where it is known to be a hard problem. A state is said to be *entangled* with respect to modes A and B if it is not larger than the combination of two physical covariance matrices. Thus, if there exist γ_A and γ_B, representing states in modes A and B respectively, such that

$$\gamma \geq \gamma_A \oplus \gamma_B, \tag{4.3}$$

with

$$\gamma_A, \gamma_B \geq \mathrm{i}\Omega, \tag{4.4}$$

then the state is separable [WW01, GKLC01b]. To quantify the degree of entanglement, the conditions that the subsystem matrices must fulfill, (Equation (4.3)), are relaxed and the measure of inseparability is taken to be the degree to which the condition is relaxed. This corresponds to a search for

$$E(\gamma) = \max_{\gamma_A, \gamma_B} x \tag{4.5}$$

subject to

$$\gamma \geq \gamma_A \oplus \gamma_B, \tag{4.6}$$

$$\gamma_A, \gamma_B \geq \mathrm{i}x\Omega. \tag{4.7}$$

The condition $E(\gamma) < 1$ implies that the state is entangled. One has to vary over all possible $\gamma_{A,B}$, but in practice this can be done easily. This is a semidefinite program for which some efficient numerical methods are readily available [sed].

4.2 Searching for Bound Entangled States

While many properties of bound entanglement can be determined based solely on a theoretical analysis, the experimental demonstration of their preparation is of great importance. This is because the preparation of these states requires the precise control of a multipartite entangled state, whose parameters are defined within tight limits. Once the experimental methods are developed, however, they will enable the construction of more elaborate multipartite schemes with which both proof-of-principle experiments can be conducted as well as establishing quantum communication networks and computing schemes. The search for a preparation scheme begins by considering an experimental setup consisting of three independent squeezing sources, four beam splitters and three phase shifters [Pin]. For simplicity, all local input states are assumed to be pure and can therefore be characterized only by the variance of the squeezed quadrature, Vs, and an additional variable, η, which represents the transmission of the pure state through a beam splitter of transmittance η. The initial covariance matrix is a product state of the form

$$\gamma_{\text{initial state}} = \gamma_1 \oplus \gamma_2 \oplus \gamma_3 \oplus \gamma_4, \tag{4.8}$$

where the covariance matrices $\gamma_1, \gamma_2, \gamma_3$ are given by

$$\gamma_i = \begin{pmatrix} Vs_i & 0 \\ 0 & Vs_i^{-1} \end{pmatrix}, \tag{4.9}$$

the fourth covariance matrix corresponds to the vacuum mode

$$\gamma_4 = \begin{pmatrix} 1.0 & 0 \\ 0 & 1.0 \end{pmatrix}, \tag{4.10}$$

and the action of the additional losses is modeled by

$$\gamma' = A^T \gamma A + G, \tag{4.11}$$

where the matrices A and G are given by

$$A = \begin{pmatrix} \sqrt{\eta} & 0 \\ 0 & \sqrt{\eta} \end{pmatrix}, \quad G = \begin{pmatrix} 1-\eta & 0 \\ 0 & 1-\eta \end{pmatrix}. \tag{4.12}$$

The state preparation circuit is drawn schematically in Figure 4.1. The preparation scheme begins by applying a phase shift, $\phi 1$, to mode 1 and mixing modes 1 and 2 on a 50–50 beam splitter. Mode 3 is initially mixed with the vacuum mode on a 50–50 beam splitter followed by a phase shift, $\phi 2$, being applied to one of its output modes. Phase shift $\phi 3$ is applied to the other output of the second beam splitter and all output modes are mixed with a corresponding mode from the other state at either a 50–50 or 30–70 beam splitter, where the reflection of the beam splitter is specified first. This produces for some combination of the parameters a PPT bound entangled state.

In order to find more robust states, we look at all physical covariance matrices, once the irrelevant parameters are taken away. The most general such covariance matrix of 4 modes,

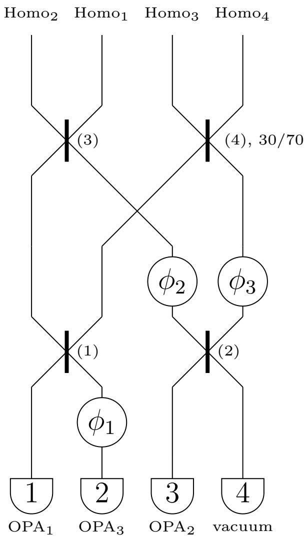

FIGURE 4.1: Simple bound entanglement circuit: This diagram gives a schematic of the circuit used to generate the bound entangled states. In total, three OPAs, four beam splitter, three phase shifters and four homodyne detectors are required. The state preparation is accomplished by mixing the individual modes at certain relative phases with each other on beam splitters. By varying the parameters of the circuit a variety of bound entangled states can be generated.

up to local unitary transformations that will not alter any entanglement properties, is of the form

$$\gamma = \begin{pmatrix} \lambda_1 & 0 & 0 & 0 & \lambda_5 & 0 & \lambda_9 & \lambda_{10} \\ 0 & \lambda_1 & 0 & 0 & 0 & \lambda_6 & \lambda_{11} & \lambda_{12} \\ 0 & 0 & \lambda_2 & 0 & \lambda_{13} & \lambda_{14} & \lambda_7 & 0 \\ 0 & 0 & 0 & \lambda_2 & \lambda_{15} & \lambda_{16} & 0 & \lambda_8 \\ \lambda_5 & 0 & \lambda_{13} & \lambda_{15} & \lambda_3 & 0 & 0 & 0 \\ 0 & \lambda_6 & \lambda_{14} & \lambda_{16} & 0 & \lambda_3 & 0 & 0 \\ \lambda_9 & \lambda_{11} & \lambda_7 & 0 & 0 & 0 & \lambda_4 & 0 \\ \lambda_{10} & \lambda_{12} & 0 & \lambda_8 & 0 & 0 & 0 & \lambda_4 \end{pmatrix}. \tag{4.13}$$

Once a state is obtained we now search for variations in which both $P(\gamma)$ increases and $E(\gamma)$ decreases. Thus, the state after a successful variation will be "more bound entangled".

The robustness of the states can be further checked by varying, for example, the phase-gates from their optimal positions. Figure 4.2 depicts the results of varying the phase-gates by as much as 0.1 rad or 5.7°. The resulting states which are still bound entangled are marked by the red points. This shows that by changing only the phase-gate settings other bound entangled states can be prepared.

4.3 Reversible and Irreversible Transformations

The existence of bound entangled states creates a sharp distinction between the distillability and separability properties of an entangled state. While the PPT criterion has been shown

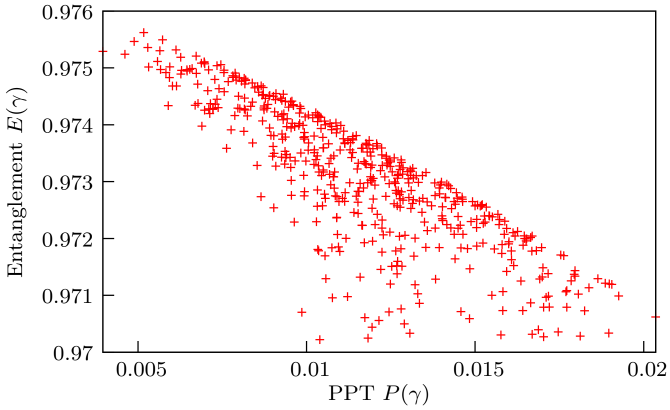

FIGURE 4.2: This plot illustrates the robustness of a bound entanglement. Starting with a bound bound entangled state, the initial phase-gate settings are varied by as much as 0.1 rad resulting in different bound entangled states indicated by the red points.

to be a necessary and sufficient criterion for the distillability of $m \times n$ Gaussian states [GKLC01a], the larger question remains that if perhaps a more physical understanding can be developed to explain why from many copies of a bound entangled state, few copies of a more highly and possibly more pure entangled state cannot be distilled. The foundations of a possible answer to this question are offered in the remaining sections of this chapter where some concepts from thermodynamics will be used. The analysis of entanglement to be given below begins with understanding the nature of reversible and irreversible entanglement transformations.

4.3.1 Reversible Transformations

The first example of a reversible entanglement transformation was provided by Bennett *et al.* [BBPS96]. In that paper, Bennett and coworkers asked the following two questions: 1) assuming one wants to produce n copies of an arbitrary pure bipartite entangled state $|\phi_{AB}\rangle$ by only local operations and classical communication, what is the minimum number, k_{min}, of maximally entangled pure states $|\psi_{AB}\rangle$ needed, 2) assuming there already are n copies of the state $|\phi_{AB}\rangle$, what is the maximum number, k_{max}, of maximally entangled pure states one can can distill using only local operations and classical communication? The mutual link between both questions is given by

$$k_{\text{max}} \leq k_{\text{min}}, \tag{4.14}$$

where,

$$E(|\psi_{AB}\rangle) = \lim_{n\to\infty} \frac{k_{\text{max,min}}}{n} E(|S_{AB}\rangle), \tag{4.15}$$

and the measure of entanglement E is taken to be the von Neumann entropy [PR97, Pre]

$$E = -\text{tr}\,(\rho \log \rho)\,. \tag{4.16}$$

Equation (4.15) is a statement of inter-convertibility between bipartite pure entangled states. It says that both states, $|\psi_{AB}\rangle$ and $|\phi_{AB}\rangle$ contain the same amount of entanglement. Additionally, the use of maximally entangled pure states as the basis against which to compare the entanglement of an arbitrary state is sensible considering that these states can be used to teleport an unknown quantum state with unit fidelity. While pure states imply reversibility, mixed states imply irreversibility.

4.3.2 Irreversible Transformations

The preparation of a quantum state will more often than not result in a mixed state. A quantum system is said to be mixed when it can only be described by a density operator

$$\rho = \sum_i p_i |\psi_i\rangle \langle\psi_i|, \tag{4.17}$$

where $|\psi_i\rangle$ are pure quantum states and p_i are the probabilities that the ith state occurs in the mixture. In general, there is no unique decomposition of a general mixed state, ρ, into a mixture of pure, orthogonal states $|\psi_i\rangle$ [BDSW96, PV01]. However, it is possible to define a minimal amount of classical information that is needed to prepare a general mixed state; and is given by the von Neumann entropy, Equation (4.16).

An example of an irreversible transformation was first provided by Lubkin [Lub87] and the treatment that follows is originally due to Plenio [PV01]. In Lubkin's process, a source which produces pure states, $|\psi_i\rangle$ with probability p_i, is brought into contact with a thermal heat bath at temperature T. Provided the two are in contact long enough, they eventually reach thermal equilibrium resulting in the mixed state ρ. An important point to recognize here is that the resultant state, ρ, is obtained regardless of the type of input states. This is a defining feature of all irreversible processes: regardless of the inputs into a process, the output is always the same.

4.3.3 Bound Entanglement and Irreversible Transformations

The preparation of bound entanglement is similar to Lubkin's irreversible transformation. The circuit begins by preparing two locally independent states, one of which is NPT entangled, and brought into contact with each other by means of the network of phase-gates and beam splitters. At the end of the preparation, a PPT bound entangled state is obtained from which the original NPT entanglement cannot be distilled. Although the state retains its inseparability properties, enough information contained in the original NPT entangled state has been lost such that it can no longer be converted to a maximally entangled state.

4.4 Summary

In this chapter I discussed how bound entangled states are verified and also the means by which they can be experimentally prepared. The circuit produces a multipartite mixed entangled state which is completely characterized by an 8×8 covariance matrix. Additionally, I drew some connections between reversible/irreversible entanglement transformations and pure/mixed entangled states. The preparation of bound entanglement represents an irreversible process whereby enough information is lost such that the state can no longer be converted to a maximally entangled state.

5

Laboratory Tools: Devices and Techniques

In this chapter I present an overview of the various devices implemented and experimental techniques developed in order to perform the experiments for this thesis. Beginning with the nonlinear optical resources, I describe how $\chi^{(2)}$ processes are used to generate the quadrature squeezing needed to prepare quadrature entanglement. I than introduce a single sideband feedback control scheme which is necessary in order to precisely set the phase-gates and homodyne detectors. I derive the error-signal from this method and conclude the chapter with the recipe for the preparation of so called "hot squeezing".

5.1 Building Blocks of an Entanglement Experiment

Entangled states of light can be prepared by implementing a mixture of linear optical components, such as beam splitters and phase shifters, and nonlinear optical components, such as optical parameter amplifiers (OPAs). All of these devices are arranged in such away as to prepare, in the simplest case, an approximation to the original EPR state [BvL05]. The optimal way of constructing such devices was explored theoretically by Wolf*et al.* [WEP03] and experimentally investigated by DiGuglielmo *et al.* [DHF^{+}07]. In order to better appreciate the role these devices play in the creation of quadrature entanglement, I will briefly review their principles of operation and show how they can work in concert to produce a variety of entangled states.

5.1.1 Nonlinear Devices: The Optical Parameteric Amplifier

The generation of multipartite quadrature entangled states requires quadrature squeezing as a fundamental resource. For all the experiments performed for this thesis, the quadrature squeezing was generated using a nonlinear optical process known as *optical parameteric amplification* (OPA). The theory of OPA is well understood and implementation of these

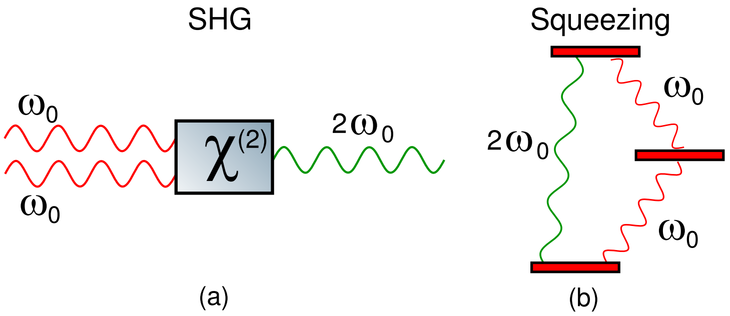

Figure 5.1: The $\chi^{(2)}$ processes: This figure illustrates the two $\chi^{(2)}$ processes used in the experiments for this thesis. Figure(a) is the process known as second harmonic generation, in which the nonlinear crystal transfers energy from the fundamental wavelength at 1064 nm into the second harmonic at 532 nm. This process is also known as *up conversion*. Figure(b) illustrates the generation of squeezing using the same $\chi^{(2)}$ crystal. This time, a strong classical mode at 532 nm is down converted into two photons at 1064 nm. These two photons are in the same mode and are quantum correlated resulting in a single mode quadrature squeezed state.

devices is well established. In this section, I give a cursory review of the theory behind the OPA process. A detailed analytical analysis as well as further applications for OPAs can be found in [Vah08, Che07] and references therein.

The OPA process is one of many that fall within the general category of $\chi^{(2)}$ nonlinear optical processes. Figure 5.1a depicts another such process known as *second harmonic generation* (SHG) and will be discussed first. An incident electric field, E, with angular frequency ω, transverses a nonlinear crystal and is transformed into an output field at double incident frequency. This is possible due to the macroscopic polarization properties of a dielectric material that result from the microscopic displacements of the valence electrons from their normal orbit about the constitute atoms or molecules. The polarization is described by

$$P = \epsilon_0 \left(\chi^{(0)} E + \chi^{(2)} E^2 + \chi^{(3)} E^3 + \ldots \right) \tag{5.1}$$

where $\chi^{(n)}$ are the nonlinear susceptibilities of the medium, E is the scalar electric field incident on the medium, ϵ_0 is the permittivity of free space and P is the polarization vector of the medium. SHG is a three photon process in which two photons at, for example, 1064 nm are converted into one photon at 532 nm. This process is known as *up conversion* and is the conjugate process to *down conversion* which I now discuss.

The OPA process is also an $\chi^{(2)}$ process that is the result of down conversion. The generation of quadrature squeezing from this requires a quantum mechanical description of the OPA process and my treatment will follow that of [GK05]. As depicted in Figure 5.1b, a strong "pump" field at frequency ω_p drives the generation of two photons known as the "signal" and "idler". If both have the same frequency, ω_0, then $2\omega_0 = \omega_\mathrm{p}$. This entire process can be described by the Hamiltonian in the interaction picture by

$$\hat{H} = i\hbar \left[\chi^{(2)} \beta^* \hat{a}^2 e^{i(\omega_\mathrm{p} - 2\omega)t} - \chi^{(2)} \beta \hat{a}^\dagger e^{-i(\omega_\mathrm{p} - 2\omega)t} \right], \tag{5.2}$$

where β corresponds to the amplitude of the pump field, ω_{p} is the frequency of the pump field, $\hat{a}, \hat{a}^{\dagger}$ are the annihilation and creation operators, respectively, and ω is the frequency of the signal and idler photons. Assuming $\omega_{\mathrm{p}} = 2\omega$, the evolution operator associated with the Hamilitonian is given by

$$\hat{U} = \exp -i\hat{H}t/\hbar = \exp \eta^{*} t\hat{a}^{2} - \eta t\hat{a}^{\dagger 2}, \tag{5.3}$$

which has the same form as the squeezing operator introduced in Chapter 2. The strength of the squeezing is determined by $\eta = \chi^{(2)}\beta$. Since the nonlinear susceptibilities tend to be small, the squeezing strength is primarily driven by the amplitude of the pump field.

There are many technical details invovled in producing quadrature squeezing. The interested reader should consult the following references [Vah08, Che07]. In the next section, I describe linear devices that are commonly used in quantum optics experiments.

5.1.2 Linear Devices: Beam splitters, Phase Shifters and Mode Cleaner

The mere presence of squeezed states is not, on its own, sufficient to generate quadrature entanglement. Even in the case of Type-II parameteric processes, the signal and idler must be spatially separated from each other if the creation of the entangled state is to be completed. This is the task of linear optical devices, such as beam splitters and phase shifters.

In addition to being linear, they also belong to the class of operations known as *Gaussian operations*. As a result, they can be conveniently described according to finite dimensional covariance matrices and posses the following form

$$B(\theta) = \begin{pmatrix} \cos(\theta) & 0 & -\sin(\theta) & 0 \\ 0 & \cos(\theta) & 0 & -\sin(\theta) \\ \sin(\theta) & 0 & \cos(\theta) & 0 \\ 0 & \sin(\theta) & 0 & \cos(\theta) \end{pmatrix}, \tag{5.4}$$

for the beam splitter matrix and

$$P(\phi) = \begin{pmatrix} \cos(\phi) & -\sin(\phi) & 0 & 0 \\ \sin(\phi) & \cos(\phi) & 0 & 0 \\ 0 & 0 & 1 & 0 \\ 0 & 0 & 0 & 1 \end{pmatrix}, \tag{5.5}$$

for the phase-shifter matrix where the angle θ is related to the transmittance of the beam splitter by $\cos(\sqrt{\tau})$ and ϕ determines the degree of rotation for the phase shifter.

Mode Cleaner

In order to detect quantum fluctuations a reference beam in the vacuum state is required. This is obtained by filtering the so called optical local oscillator, c.f. Section 5.1.3, through a three mirror ring cavity known as a mode cleaner. The spectral properties of the mode cleaner are of particular interest for experiments in quantum optics. Since the majority of

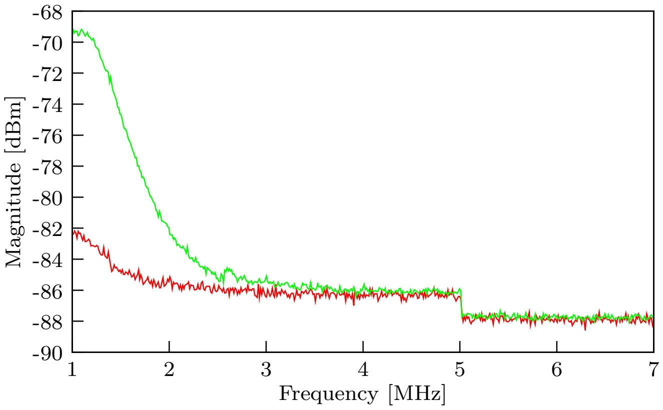

FIGURE 5.2: Power spectrum of local oscillator: This graph depicts the measured power spectrum of the local oscillator after the mode cleaner. Both spectra were measured using a resolution bandwidth, RBW, of 30 kHz and a video bandwidth, VBW, of 30 Hz. The red curve represents the high finesse operation of the mode cleaner and the green curve the low finesse operation of the mode cleaner. In both cases, the local oscillator is vacuum noise limited in the measurement frequency band, 6-7 MHz.

the experiments performed for this thesis where conducted at sideband frequencies on the order of MHz, the local oscillator must be vacuum noise limited at these frequencies. The mode cleaner could be operated in either one of two modes: hight finesse and low finesse. In high finesse mode the linewidth of the resonator is 55 kHz and has a finesse of $\mathcal{F} = 10500$. In low finesse mode the linewidth of the resonator is 1.5 MHz with a finesse of $\mathcal{F} = 369$ [Sam07]. Figure 5.2a depicts the spectral noise power of the local oscillator in high finesse mode and Figure 5.2b in low finesse mode. In both case it is seen that the local oscillator is vacuum noise limited in the frequency band of interest.

5.1.3 Homodyne Detection

Having successfully prepared a quadrature entangled state the final step is the verification of the entanglement. This is achieved by measuring, in the Gaussian case, the covariance matrix of the states quantum fluctuations. This is performed by employing a technique known as *homodyne detection*. The basic idea behind homodyne detection is that a signal beam is split on a beam splitter and detected with two different photodetectors. The AC currents of these two detectors are then subtracted from one another. The result is another AC current, whose statistical moments carry the desired information about the quantum state of the light being probed.

In balanced homodyne detection, the signal beam is mixed with a strong coherent local oscillator on a 50/50 beam splitter. The phase relation between the local oscillator and the signal beam acts as a selector which determines which quadrature of the field will be probed. A detailed calculation of the photocurrents produced from the individual photodetectors can be found in [DiG06]. The result is

$$\begin{aligned} i_1 &= \hat\beta_1^\dagger \hat\beta_1 \\ &= \frac{g}{2}\Bigg(\alpha_1^2 + \alpha_{LO}^2 + 2\cos(\theta)\,\alpha_1\alpha_{LO} \\ &\qquad + \alpha_1\left(\delta\hat X_1^+ + \delta\hat X_{LO}^{-\theta}\right) + \alpha_{LO}\left(\delta\hat X_{LO}^+ + \delta\hat X_1^\theta\right)\Bigg), \end{aligned} \tag{5.6}$$

$$\begin{aligned} i_2 &= \hat\beta_2^\dagger \hat\beta_2 \\ &= \frac{g}{2}\Bigg(\alpha_1^2 + \alpha_{LO}^2 - 2\cos(\theta)\,\alpha_1\alpha_{LO} \\ &\qquad + \alpha_1\left(\delta\hat X_1^+ - \delta\hat X_{LO}^{-\theta}\right) + \alpha_{LO}\left(\delta\hat X_{LO}^+ - \delta\hat X_1^\theta\right)\Bigg), \end{aligned} \tag{5.7}$$

where α_1 is the classical amplitude of the signal field, α_{LO} is the classical amplitude of the optical local oscillator, θ is the relative phase between the local oscillator and the signal field, g is the electronic gain of the photodetector and δX represents the linearized version of the quadrature operators where X^+ corresponds to the amplitude quadrature and X^- corresponds to the phase quadratures. The sum and difference photocurrents read

$$i_{\text{sum}} = g\left(\alpha_1^2 + \alpha_{\text{LO}}^2 + \alpha_{LO}\delta X_{\text{LO}}^+\right), \tag{5.8}$$

$$i_{\text{diff}} = g\left(2\cos\theta\alpha_{\text{LO}} + \alpha_{LO}\delta X_1^\theta\right). \tag{5.9}$$

Calculating the variance of the resulting expressions yields

$$\Delta^2\hat i_{\text{diff}} = g^2\alpha_{\text{LO}}^2\Delta^2\hat X_1^\theta, \tag{5.10}$$

$$\Delta^2\hat i_{\text{sum}} = g^2\alpha_{\text{LO}}^2\Delta^2\hat X_{\text{LO}}^+. \tag{5.11}$$

Equation (5.10) shows that the measured quadrature is therefore dependent on the relative phase between the local oscillator and the signal field i.e. $\hat X_1^{\theta=0} = \hat X_1^+$ and $\hat X_1^{\theta=\pi/2} = \hat X_1^-$. By adjusting the phase relation between the signal beam and local oscillator, any quadrature of the field can be measured, not just the amplitude quadrature. It is interesting to note, that the noise portion of the local oscillator i.e. $\delta\hat X_{\text{LO}}^+$ is not present in the difference current. The local oscillator must also be in a vacuum state. Experimentally this is achieved by blocking the signal beam input into the beam splitter and mixing the vacuum mode with the coherent local oscillator. This then serves as the reference to observe the noise reduction of the squeezed state.

If the components I described in Section 5.1 were simply to be placed on the table and turned on, the result would be nothing short of a random walk down the optical table. This is because they must not only be set to their operating point but must also remain there despite disturbances which seek to impose the contrary. This necessitates the implementation of electronic control systems to act as the cohesion and hence make the experiment. It is these systems to which I now turn.

5.2 Feedback Control Schemes

In order to produce a stable source of entangled states, squeezed optical fields must be brought to interfere with each other at a constant relative phase. This is achieved by means of a feedback control system which suppresses the disturbances which would cause the relative phase to leave its so called "operating point". The techniques utilized to keep the optical fields at their operating point are taken from the general field of *feedback control* [FPEN05, AC00]. A control loop works by taking an input signal, known as the *error signal*, and produces as an output a correction signal to keep a system at its operating point. The error signal (ER) is generally defined as the difference between a reference value which sets the operating point and the current value of the system

$$\mathrm{ER} = i_{\mathrm{reference}} - i_{\mathrm{current}}, \tag{5.12}$$

where the operating point is reached when ER = 0. In this section, I present two different methods for deriving an error signal such that the relative phase between interfering fields can be set to a desired operating point. As will be seen, what distinguishes these two schemes from one another is the way the control signal is imprinted onto the modes.

5.2.1 Optical Fields and Classical Modulations

In order for any control system to work, a sensor must be able to detect a signal which provides the necessary information as to the current state of the system under control. In the case of interference between optical fields, the signal is imprinted onto one of the interfering modes by means of a device known as an electric optical modulator (EOM). There are two different types of modulations and I discuss each of these in turn.

Phase Modulation

A phase modulation is produced by sinusoidally modulating the phase of an electric field

$$E = E_o e^{i\omega_o t}, \tag{5.13}$$

with a modulation frequency ω_m and a modulation amplitude m resulting in

$$\begin{aligned} E_{\mathrm{phase}} &= E_o e^{i(\omega_o t + m\cos(\omega_m t))} \\ &= E_o e^{i\omega_o t}\left(1 + i\frac{m}{2}\left(e^{i\omega_m t} + e^{-i\omega_m t}\right)\right), \end{aligned} \tag{5.14}$$

where ω_o is the carrier frequency and ω_m is the modulation frequency.

Amplitude Modulation

An amplitude modulation is produced in a similar manner to a phase modulation by sinusoidally modulating the amplitude of the electric field

$$\begin{aligned} E_{\mathrm{amplitude}} &= E_o\left(1 + m\cos\left(\omega_m t\right)\right) e^{i\omega_o t} \\ &= E_o e^{i\omega_o t}\left(1 + \frac{m}{2}\left(e^{i\omega_m t} + e^{-i\omega_m t}\right)\right), \end{aligned} \tag{5.15}$$

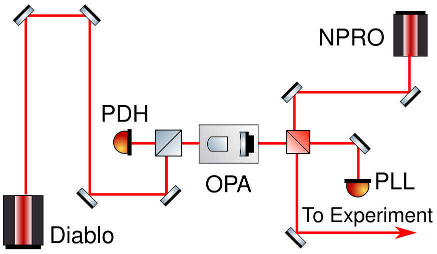

Figure 5.3: Phase-Lock Loop: The interference between the output of the optical parameter amplifier cavity (OPA) and the auxiliary NPRO laser produces an amplitude modulation on the resulting field which can be detected by all photodetectors throughout the experiment. The frequency of the amplitude modulation is determined by setting the temperature of the NPRO crystal and deviations from the working point are maintained by actuating on the piezo element attached to the NPRO crystal effectively changing the cavity length and thereby its frequency.

where again ω_o is the carrier frequency and ω_m is the modulation frequency. Equation (5.15) differs from Equation (5.14) in the phase relationship between the carrier and the sidebands. This is set by the $i = e^{i\pi/2}$ term in Equation (5.14) indicating a ninety degree phase shift between the carrier and the sidebands in the case of a phase modulation.

A phase modulated electric field can be used as a signal to set the operating point of an interferometer in the following way. The interference between a phase modulated field, E_{phase}, and a reference field with an additional phase $E_{\text{ref}}e^{i\theta}$, on a 50/50 beam splitter produces an error signal given by

$$i_{\text{ER}} \propto E_{\text{ref}} E_{\text{phase}} m \sin(\theta), \tag{5.16}$$

where E_{ref} is the amplitude of the reference field, E_{phase} is the amplitude of the phase modulated field, m is the modulation index and θ is the relative phase between the phase modulated and reference electric fields. The form of Equation (5.16) shows that the error signal is zero when the phase relationship between the two incident beams is $\phi = n\pi$, $n \in \mathbb{N}$. For the experimental demonstration of bound entanglement, however, the optical fields must be set to an arbitrary relative phase. To this end, a different locking scheme involving an external laser and known as “single-sideband” is used to derive the error signal.

5.2.2 Single-Sideband: Phase-Lock Loop

In the single-sideband technique the control signal is also imprinted on one of the interfering modes but this time is generated by the interference between the main Diablo laser with an auxiliary NPRO laser. The experimental setup is illustrated in Figure 5.3. The output of the OPA cavity is infrared light at 1064nm originating from the main laser source and the output of the NPRO laser is slightly detuned from this wavelength by controlling the temperature of its crystal. These beams are brought to interfere at the dichroic beam splitter which is actually responsible for separating the green pump beam from the squeezing that is produced at the fundamental wavelength. Part of the light is transmitted through the dichroic beam splitter to a photodetector denoted by “PLL”. The reflected beam is sent to the rest of the experiment.

It is at the PLL photodetector that the beat frequency between the OPA output beam and the NPRO beam is detected. The initial fields can be described by the following scalar quantities once the polarization, direction of propagation and wave number are set to constant values. The scalar fields then read

$$\begin{aligned} E_{\mathrm{OPA1}} &= \alpha_o e^{i\omega_o t}, \\ E_{\mathrm{NPRO}} &= \alpha_m e^{i\omega_m t}, \end{aligned} \tag{5.17}$$

where E_i is the scalar field originating from the respective source, α_i is the corresponding real valued amplitude and ω_i is the angular frequency. Interference of the fields at the beam splitter results in an electric field given by

$$\begin{aligned} \tilde{E} &= \frac{1}{\sqrt{2}} \left(E_{\mathrm{OPA1}} \pm E_{\mathrm{NPRO}} \right) \\ &= \frac{1}{\sqrt{2}} \left(\alpha_o e^{i\omega_o t} \pm \alpha_m e^{i\omega_m t} \right). \end{aligned}$$

At this point a few simplifications can be made for further calculations. First, since the carrier frequency is usually six orders of magnitude larger than the modulation frequency, I will assume that the carrier remains stationary, $\omega_o = 0$ and only the sidebands are rotating. Second, I will treat the second carrier as a single-sideband modulation and introduce the following new amplitudes

$$E_o \equiv \frac{\alpha_o}{\sqrt{2}} \quad \text{and} \quad m \equiv \frac{\alpha_m}{\alpha_o}. \tag{5.18}$$

With these simplifications the control field that will be used throughout the experimental setup is given by

$$E_{\mathrm{C}} = E_o \left(1 \pm m e^{i\omega_m t} \right) \tag{5.19}$$

The interference term is responsible for the frequency dependent intensity modulation. This modulation is measured by the photodiode and demodulated at the desired frequency. In the bound entanglement experiment, a modulation frequency of 15 MHz was chosen for the phase gates and homodyne detectors. The control loop actuates on the NPRO laser by a piezo attached to the crystal. The cavity length of the NPRO laser is thereby altered, changing the frequency of the produced laser light to match the predefined beat frequency with the Diablo.

The phase lock loop effectively produces a “ruler” in the form of a well defined beat frequency which can be detected by all other photodetectors in the experiment. As I will now show, this ruler can be used as the standard against which all other interfering modes can be compared in order to determine the relative phase between the interfering beams.

5.2.3 Setting a Phase-Gate

In this section I show how the beat frequency between the main laser and auxiliary NPRO can be used to set the relative phase between two beams at a beam splitter.

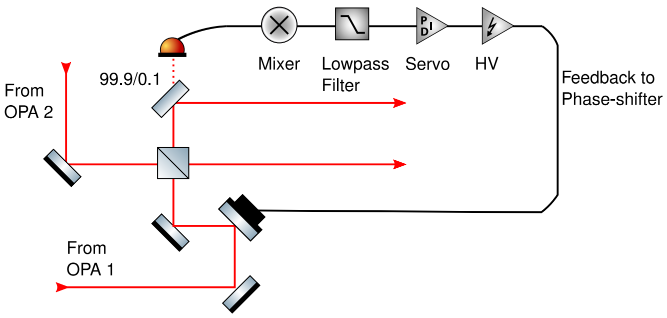

FIGURE 5.4: Single photodetector phase-gate locking scheme: This figure depicts the experimental setup for locking a phase-gate using only one locking photodetector. Approximately 0.1% of the light from the beam splitter is tapped-off and detected using a resonant photodetector. This signal is than demodulated at the beat frequency between the main Diablo and NPRO lasers. After lowpass filtering, the servo provides the correction signal which is applied to the piezo. Figure 5.6a illustrates how the error-signal behaves when using this setup.

Single Photodetector Scheme

The first locking scheme I describe involves a single photodetector. The control field, Equation (5.19), is mixed with the output of an OPA which contains an additional term to describe a relative phase-shift between the two beams

$$E_{\mathrm{OPA}} = E_{\mathrm{OPA}} e^{i\theta}, \tag{5.20}$$

where θ describes the relative phase-shift between the control field and the OPA field and the carrier of the OPA field has been suppressed by changing to the rotating frame. After mixing the control field and OPA field on a 50/50 beam splitter the output field is given by

$$\tilde{E} = \frac{1}{\sqrt{2}} \left(E_{\mathrm{C}} \pm E_{\mathrm{OPA}} \right). \tag{5.21}$$

Calculating the AC part of the photocurrent results in

$$\begin{aligned} i_{\mathrm{AC}} &= \tilde{E}\tilde{E}^{*} \\ &= 2P_0 m \cos(\omega_m t) + 2\sqrt{P_0 P_{\mathrm{OPA}}} m \cos(\omega_m t - \theta), \end{aligned} \tag{5.22}$$

where P_0 is the power associated with the field amplitude defined in Equation (5.18), P_{OPA} is the optical power of the second interfering field, θ is the relative phase between the interfering fields that is to be controlled and ω_m is the beat frequency between the NPRO and Diablo lasers.

In order to derive an error signal, Equation (5.22) is demodulated and lowpass filtered with $\sin(\omega_m t - \varphi)$ where ω_m is the beat frequency and φ is the electronic demodulation phase. The resulting error-signal is given by

$$\mathrm{ER} = -P_0 m \sin(\varphi) + \sqrt{P_0 P_{\mathrm{OPA}}} m \sin(\varphi - \theta). \tag{5.23}$$

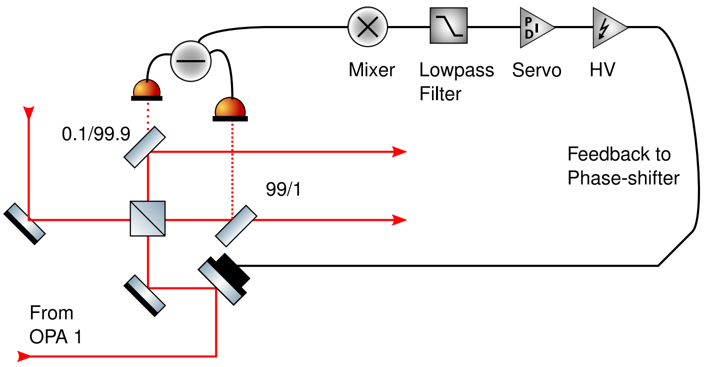

FIGURE 5.5: Dual photodetector phase-gate locking scheme: This figure depicts the experimental setup actually used to lock each phase-gate. Approximately 0.1% of the light from both outputs of the phase-gate beam splitter is tapped-off and sent to resonant photodetectors. The AC signals are than subtracted and the resulting signal is demodulated at the beat frequency between the main Diablo and NPRO lasers. The error-signal produced by this setup is given in Figure 5.6b. By changing the demodulation phase, φ, the relative phase, θ, between the interfering fields can be set arbitrarily.

Equation (5.23) is plotted in Figure 5.6a. It is seen that the signal possess an additional amplitude modulation. This is caused by the $-P_0 m \sin(\varphi)$ term in Equation (5.23) which produces a demodulation phase dependent modulation of the error signal. In order to eliminate this extra term, an additional photodetector must be introduced in the second output of the interference beam splitter.

Dual Photodetector Scheme

The introduction of a second photodetector, depicted in Figure 5.5, changes the error-signal as follows: first, the individual photocurrents are electronically added together with an additional electronic phase, ϕ, added to one of the inputs

$$i_{\text{total}} = i_1 + e^{i\phi} i_2. \tag{5.24}$$

Next, the total AC photocurrent is demodulated with $\sin(\omega_m t - \varphi)$ and lowpass filtered to eliminate the higher frequency components. The resulting error signal is given by

$$i = 2\sqrt{P_0 P_{\text{OPA}} P_m}\,\sin(\varphi - \theta), \tag{5.25}$$

where P are the optical powers of the respective fields. Equation (5.25) is plotted in Figure 5.6b for different demodulation phases φ. The second photodetector eliminates the modulation of the error signal. By simply changing the electronic demodulation phase, φ, the relative phase between two interfering fields can be set to an arbitrary angle.

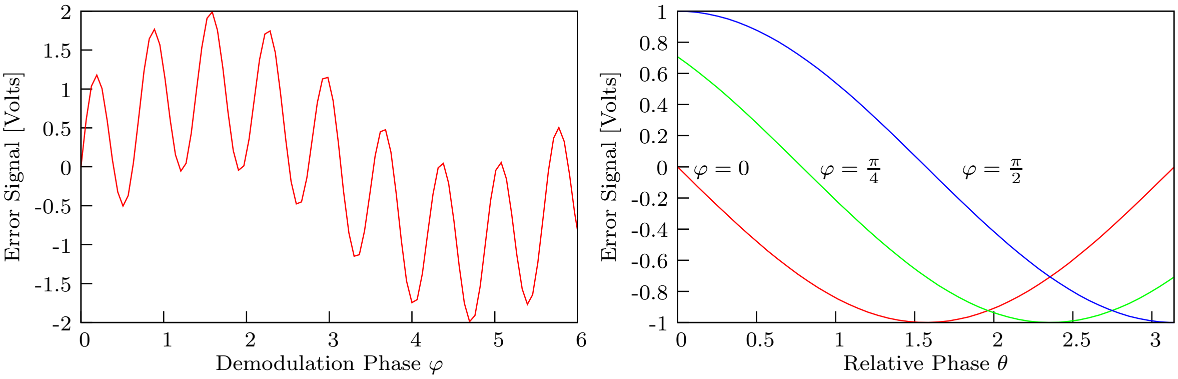

(a) Single photodetector error-signal (b) Dual photodetector error-signal

Figure 5.6: Single-sideband error-signals: These figures depict the possible error-signals which can be derived using the single-sideband locking technique. Figure(a) represents the case when using only one locking photodetector and Figure(b) is the case when two photodetectors are used. Figure(a) shows am amplitude modulation on the error-signal which is due to the demodulation phase. This amplitude modulation disappears if a second photodetector is introduced. Figure(b) also shows that simply by changing the demodulation phase, φ, the relative phase between the interfering fields can be set to an arbitrarily.

5.3 Generation of Hot Squeezing

The preparation of bound entanglement requires a type of squeezing known as “hot” squeezing. I discussed in Chapter 2 that the defining feature of a quadrature squeezed state is the reduced noise below the vacuum noise level in one quadrature with an amplification of the noise above the vacuum noise level in the conjugate quadrature. A mixed squeezed state posses a larger anti-squeezed quadrature than squeezed, but the squeezed quadrature is still below the vacuum noise limit. A state whose noise distribution is not equal in the amplitude and phase quadratures but whose reduced quadrature noise is *greater* than the vacuum noise is said to posses hot squeezing. With regard to the classicality properties of this state, hot squeezing is indistinguishable from a classical state. I will now illustrate two different methods for generating hot squeezing, the *EPR-Approach* and the *Modulation-Approach*.

5.3.1 Method 1: EPR-Approach

The EPR approach uses the same experimental setup as that which would be used to generate the two-mode squeezed state. Two initially squeezed beams are brought to interfere at a balanced beam splitter but with a relative phase of less than ninety degrees. Figure 5.7 illustrates the result of such an experiment. In both outputs of the beam splitter, the distribution of the quantum noise looks similar to that of a squeezed state but whose “squeezed” quadrature does not fall below the vacuum noise level. One output of the beam splitter would be used and the other discarded. In this way, a hot squeezed state has been prepared.

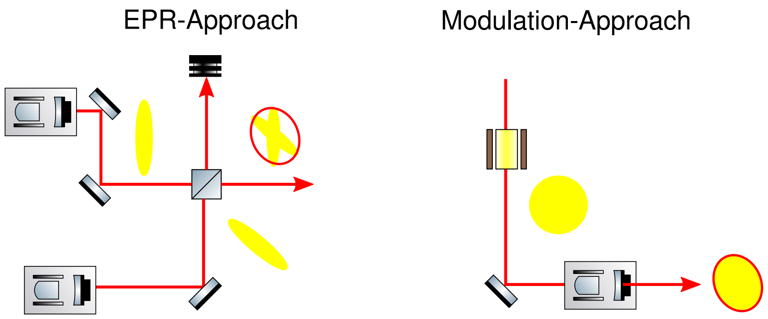

FIGURE 5.7: Generation of hot squeezing: This figure depicts two equivalent methods for generating hot squeezing. In the "EPR-approach", two squeezed modes are brought to interference at a relative phase between $0^\circ < \theta < 90^\circ$. Only one of the outputs of the beam splitter is utilized, the other is discarded. In the "modulation-approach", the control field to the OPA cavity is phase modulated at the desired sideband frequency using random classical voltage noise. The OPA is then locked in amplification mode, squeezing the phase quadrature and anti-squeezing the amplitude quadrature. The strength of the phase noise is adjusted such that after deamplification, the total quadrature noise level is still above vacuum noise. This produces the equivalent state as with the EPR-approach.

5.3.2 Method 2: Modulation Approach

The exact same state as generated by the EPR approach can also be generated using a modulation scheme. This scheme is also illustrated in Figure 5.7. Here, the input to an OPA is first phase modulated at the desired squeezing sideband frequency. Next, the OPA is locked in amplification mode whereby the phase quadrature is squeezed. At the same time, the amplitude quadrature is amplified, producing the anti-squeezed quadrature. The result for a given modulation strength is exactly equivalent to that produced by the EPR approach but without the need for a second OPA and control loop to set the phase between the modes

5.4 Summary

In this chapter, I introduced the experimental tools and techniques used to generate the quadrature entanglement for this thesis. Of particular importance is the single sideband locking technique which enables setting the working point of the phase-gates and homodyne detectors to an arbitrary relative phase. Additionally, I presented two schemes for the preparation of hot squeezed states.

I have now presented all the preparatory material needed for understanding the experiments performed for this thesis. The final chapters are each dedicated to a single experiment and provide detailed descriptions of the experimental procedures and results. The first experiment to be discussed is a Bayesian scheme for quantum state reconstruction. The last two experiments deal exclusively with quadrature entanglement.

6

Reconstructing a Quantum State

This chapter contains the first of three experiments performed for this thesis. I introduce a new statistical method for quantum state reconstruction based on the Bayesian paradigm. The goal is to derive error-bars on the reconstruction of the state that can then be used when evaluating its properties. Especially in cases where the experimental results are meant to be proof-of-principle demonstrations of some physical effect, e.g. negativity of the Wigner function or bound entanglement, all claims of a successful demonstration must be qualified in terms of the uncertainty on the stated result. The methods by which these qualifications can be quantified are the topic of this chapter.

As I described in Chapter 2 quantum states can be fully characterized by the Wigner function in phase-space. Since the theoretical discovery by Vogel and Risken [VR89] that the Wigner function can be reconstructed from homodyne detector data, a number of reconstruction schemes have been developed ranging from direct inversion of the tomographic data by means of the filtered-back projection method [SBRF93] to statistical methods such as maximum-likelihood estimation [Hra97, BDPS99, Fiu01, Lvo04, HMv06, vHKL07]. An important feature of maximum-likelihood methods is the guaranteed positive “semi-definiteness” of the reconstructed state. The result of a maximum-likelihood reconstruction method is either a density matrix [Lvo04, HMv06] or a set of parameters [DPS00, OTBG06] which have maximized the likelihood functional given a model of the measurement apparatus and of the parameterized state. A full analysis of the experimental data, however, should also answer important questions regarding error-bars on the estimation of the state parameters, possible correlations amongst the parameters, and error-propagation when using the reconstructed state for further calculations of quantities such as the purity of the state or amount of entanglement.

The uncertainties in quantum state estimation can be consistently determined by using a general and statistically well motivated Bayesian analysis scheme known as the Markov Chain Monte Carlo (MCMC). The method is based on the implementation of a Markov chain to search the parameter space resulting in a set of *samples from the joint posterior probability density distribution* on the unknown parameters of the model.

This technique produces several important results. First, it yields the Markov chain containing all of the relevant statistical information about the parameter space. Second, one can extract a set of marginalized probability density distributions for each parameter quantifying the degree of uncertainty on their estimation. Third, the resulting chain can be used in further calculations, where one can produce probability density distributions on quantities such as of the purity or amount of entanglement of the reconstructed state.

6.1 Bayesian Statistical Analysis

Bayes' theorem prescribes the rule to invert the relationship between the experimental data already observed and the parameterized model which could have generated the measured data. The uncertainties on the model parameters are described by a probability distribution known as the *posterior* and is quantified in Bayes' theorem given in conventional form by [Gre06]

$$p(\vec{\lambda}|D\,,M\,,I) = \frac{p(D|\vec{\lambda}\,,M\,,I)p(\vec{\lambda}|M\,,I)}{p(D|M\,,I)}. \tag{6.1}$$

The individual components of Bayes' theorem, presented now in a notation to be adopted throughout the rest of this thesis, correspond to probabilities and have the following interpretations

Posterior $p(\vec{\lambda}|D\,,M\,,I)$

The conditional probability of the parameters $\vec{\lambda}$, given the measured data D, a model M and some background information I.

Likelihood $\mathcal{L}(D|\vec{\lambda}\,,M\,,I)$

The conditional probability of obtaining the data, D, given the parameter values $\vec{\lambda}$, a model M and some background information I.

Prior $\pi(\vec{\lambda}|M\,,I)$

The conditional probability of obtaining the parameters $\vec{\lambda}$ given a model M and some background information.

Evidence $p(D|M\,,I)$

The conditional probability of obtaining the data D given a model M and some background information I.

In each of the elements of Bayes' theorem $\vec{\lambda}$ corresponds to the parameter vector, M labels the assumed model, D is the measured data and I is any relevant background information. The goal of Bayesian analysis is to determine the posterior. Bayes' theorem states that the posterior is proportional to the product of the likelihood and the prior. Since both of these are known the posterior can be determined. I will now explain how the various constituents in Bayes' theorem are assigned.

6.1.1 Assigning the Likelihood

The likelihood function, $\mathcal{L}(D|\vec{\lambda}, M, I)$, gives the probability for obtaining the measured data D, assuming a parameter vector, $\vec{\lambda}$, a model M and any other relevant background information I. The likelihood corresponds to the sampling statistics of the experiment and its determination will be illustrated with three examples from quantum optics.

Homodyne Detection

The first case to be considered is that of balanced homodyne detection c.f. Section 5.1.3. Optical homodyne detection yields a continuous set of values whose underlying statistics describe the properties of the quantum state under investigation. The total number, N, of raw data collected within a certain bandwidth is determined in advance by the experimentalist. The data can be summarized by building a histogram with a specified number of bins and bin locations. Since the total amount of collected data, the total number of bins and the bin locations are all under the control of the experimentalist, the only the free variable left that is under the control of the unknown quantum state, ρ, are the number of data points, n_j, that fall into the j^{th} bin. These considerations lead to the conclusion that the distributional form of the likelihood function for homodyne detection should be assigned the multinomial distribution

$$\mathcal{L} = N! \prod_{j}^{N} \frac{P_j^{n_j}}{n_j!}, \tag{6.2}$$

where N represents the total amount of data collected, n_j the number of data points contained in the j^{th} bin and P_j the theoretical probabilities for obtaining a result in the j^{th} bin.

The theoretical probabilities are calculated using quantum mechanics and basic probability theory. For example, the result of performing homodyne detection on a general Gaussian state is calculated by marginalizing the Wigner function

$$p(\xi') = \int W(\xi) d\xi \tag{6.3}$$

where ξ represents the initial vector of operators, $d\xi$ specifies those operators over which the integration is performed and ξ' is the vector containing the resulting operators. For example, assuming a single mode vacuum Gaussian state with initial quadrature operators given by $\xi = (\hat{x}, \hat{p})$ and covariance matrix γ, the probability density that would be obtained from homodyne detection for the amplitude quadrature is obtained by integrating the Wigner function over the phase quadrature

$$p(\hat{x}) = \frac{1}{\sqrt{2\pi \det(\gamma)}} \int e^{-\frac{1}{2}\xi^T \gamma^{-1} \xi} d\hat{p}. \tag{6.4}$$

The probability for a measurement result to fall within the j^{th} bin is than calculated by

$$P_j = \int p(\xi') d\xi', \tag{6.5}$$

where the integration limits are taken to be over the bin of interest.

Single Photon Detection

The second case to be considered is that of single photon detection. The idea behind a single photon detector is that of an "ON/OFF" experiment where, in the case of an event, the detector goes proverbially "click" and in its absence remains quiet. In contrast to the optical homodyne detection case, the total number of events or "clicks" per bandwidth is no longer under the experimentalist's control. Instead, the total number of clicks is the desired statistical information which describes the nature of the unknown quantum state ρ. These considerations lead to the conclusion that the distributional form for the likelihood function is Poissonian

$$\mathcal{L} = \prod_j \frac{e^{-NP_j}\,(NP_j)^{n_j}}{n_j!}, \tag{6.6}$$

where N is the unknown mean number of occurrences, n_j are the individual measurement results and P_j are their theoretically probabilities.

Apparatus Error

The final example I will consider is when the uncertainty with regard to a measurement originates from the measuring apparatus itself. In the absence of such error, each recorded datum y_i, should correspond to the expected value x. If the form of the apparatus uncertainty is additive Gaussian noise, then the statistical model for this experiment is given by

$$x = y_i + \epsilon, \tag{6.7}$$

where ϵ corresponds to a Gaussian probability distribution. The likelihood function is therefore

$$\mathcal{L} = \frac{1}{(2\pi\sigma^2)^{(N/2)}} \exp\left(-\frac{1}{2} \sum_{i=1}^{N} \frac{(y_i - x)^2}{\sigma^2} \right), \tag{6.8}$$

where N corresponds to the number of measurements, σ is the standard deviation associated with each datum and x is the parameter to be estimated. It is often the case that the measurement error, σ on each datum is not known and should be estimated from the measured data. In that case, σ, also becomes a parameter to be estimated.

6.1.2 Assigning the Prior

The prior $\pi(\vec{\lambda}|M\,,I)$ represents the degree of uncertainty on the parameter vector $\vec{\lambda}$ and is assigned *before* the data is collected. The prior can be understood to describe the degree of knowledge the experimentalist has before performing the measurement. After data collection, the prior is updated by the likelihood and the new state of knowledge with regard to the parameters is given by the posterior. Two strategies for assigning the prior are *conjugate priors* and *non-informative priors*. I will only briefly summarize these methods here. A more thorough discussion can be found in [CL96].

Likelihood	Prior
$\mathcal{L} = \frac{\lambda^n e^{-\lambda}}{n}$	$\pi = x^{k-1} \frac{\exp -x/\theta}{\Gamma(k)\theta^k}$
$\mathcal{L} = N! \prod_j^N \frac{P_j^{n_j}}{n_j!}$	$\pi = \frac{1}{B(\alpha)} \prod_{i=1}^K x_i^{\alpha_i - 1}$

TABLE 6.1: Conjugate priors: This table list two examples of conjugate priors for the Piossonian and Multinomial likelihoods. Their corresponding conjugate priors are the Gamma and Dirichlet distributions, respectively.

Conjugate Priors

A conjugate prior is one which leads to a posterior belonging to the same distributional family as the likelihood. The choice of a conjugate prior is motivated by the fact that it may lead to closed form posteriors [CL96]. Two examples of priors conjugate to likelihood functions are given in Table 6.1. There it is seen, for example, that the Dirichlet distribution is the conjugate prior to the multinomial distribution. A list of likelihoods and their conjugate priors can be found in [wik].

The distributional form of a conjugate prior is set by the likelihood. It may be, however, that no reliable prior information exists with regard $\vec{\lambda}$. In this case, non-informative priors express this degree of uncertainty.

Non-informative Priors

A non-informative prior is an expression of total uncertainty about a parameter, λ_i, before a measurement is conducted. Based on this definition it may seem that a uniform distribution on λ_i

$$\pi(\lambda_i) = \frac{1}{b-a}, \quad a < \lambda_i < b, \tag{6.9}$$

would be the best choice. However, Equation (6.9) suffers from the limitation that it is not invariant under a reparameterization of the estimation problem [Siv06]. A better choice is to a use a *Jeffrey's prior* which is defined by the Fisher information matrix.

6.2 Markov Chain Monte Carlo

Having assigned the likelihood and prior the posterior is proportional to

$$p(\vec{\lambda}|D, M) \propto \mathcal{L}(D|\vec{\lambda}, M)\pi(\vec{\lambda}|M). \tag{6.10}$$

The uncertainties on the individual components of the parameter vector $\vec{\lambda}$ are calculated by marginalizing the posterior Equation (6.10). Depending on the form of $\mathcal{L}$ and π, the integration may be intractable in closed form. At this point, numerical methods of integration are required. One such method is known as *Markov Chain Monte Carlo* and is the topic of the next section.

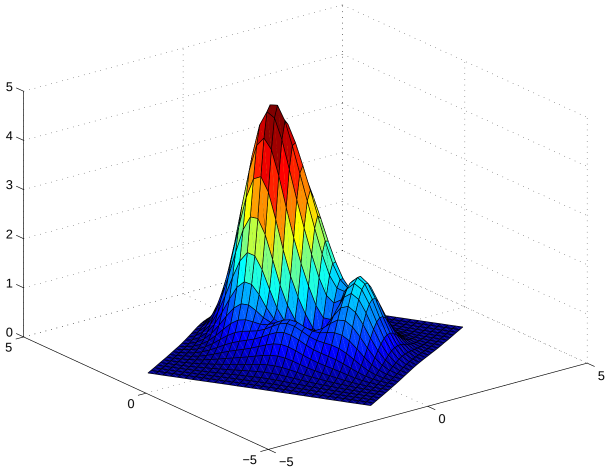

FIGURE 6.1: Example posterior: Depending on the product of the likelihood function and the prior distribution the posterior distribution may contain multiple peaks. The goal of an MCMC is to sample from the entire space without getting stuck in any local minima.

6.2.1 Basic Idea

I will first illustrate the general idea of the Markov Chain Monte Carlo (MCMC) algorithm before continuing with the exact details of its implementation. Because the posterior distribution contains all of the relevant statistical information regarding the uncertainty on the model parameters, sampling from the posterior is equivalent to obtaining all parameter values commensurate with the measured data and prior knowledge before the experiment is performed. The posterior can be understood as a function defined on a multidimensional space, whose dimension is given by the number of parameters to be estimated. Exploration of the parameter space can be achieved by "jumping" around in all dimensions, effectively mapping out its structure. The collection of these jumps is known as "the chain", $\mathcal{C}$, and corresponds to the collection of parameter vectors returned by the algorithm, i.e. $\mathcal{C} = \{\vec{\lambda}_0, \vec{\lambda}_1, \ldots \vec{\lambda}_t\}$. The point at which the chain begins to contain values that are drawn from the posterior is the point at which it has reached equilibrium. At this point, we say that the chain has "converged" to the posterior. These basic concepts: posterior, chain and convergence are summarized in Table 6.2. As illustrated in Figure 6.1 some parts of parameter space correspond to higher areas of posterior whereas some parts corresponds to lower areas of posterior. The task of the algorithm is to generate samples such that all interesting regions of the posterior have been covered.

There are two main strategies for parameter space exploration: a "grid walk" and a "random walk". The grid walk is illustrated in Figure 6.2a and involves defining some type of grid with predefined separation between the grid points. The exploration strategy is to walk along each dimension recording the value of the posterior at each node. While this approach is conceptually easy to understand, the complexity of the problem scales with N^d, where N is the number of grid points in each dimension and d is the number of parameters.

The second approach to the problem of parameter space exploration is to randomly walk through parameter space. In order to accomplish this, a criterion needs to be established

Posterior	The product of the likelihood function and prior distribution whose marginalized distributions quantify the degree of uncertainty on the respective parameter.
Chain	The collection of parameter vectors $\vec{\lambda}_t$ which are sampled from the posterior distribution.
Convergence	The point at which the chain starts to draw samples from the posterior distribution.

Table 6.2: MCMC concepts: This table lists three fundamental concepts from the Markov chain Monte Carlo method. The posterior is the distribution which describes the statistical uncertainty on the estimated parameters. The chain is a vector containing all samples drawn from the posterior and convergence of the chain is said to occur at the point where the MCMC algorithm starts sampling from the posterior.

which encourages jumps to locations of parameter space that fall within the range of the posterior and discourages jumps which do not. The goal is to let the algorithm determine this, based on the measured data and on the unknown functional form of the posterior distribution. Such a criterion was developed by Metropolis [MRR⁺53] that compares the relative values of the posterior distribution for any two positions

$$r = \frac{\mathcal{L}(\vec{\lambda}_t)\pi(\vec{\lambda}_t)}{\mathcal{L}(\vec{\lambda}_{t-1})\pi(\vec{\lambda}_{t-1})}. \tag{6.11}$$

Using this criterion, a ratio greater than one, $r > 1$, would indicate that the current position, $\vec{\lambda}_t$ corresponds to higher regions of posterior whereas a ratio less than one, $r < \vec{\lambda}_{t-1}$, would indicate that the previous position $\vec{\lambda}_{t-1}$ corresponded to higher regions of posterior. Repeating this procedure and applying a rule to determine whether to accept or reject the new position guarantees that all samples returned from the algorithm will be from the desired posterior. The procedure just described is the strategy behind the algorithm known as the *Metropolis-Hastings Sampler*, the algorithm to which I now turn.

6.2.2 Metropolis-Hastings Algorithm

The Metropolis-Hastings algorithm is given by the following steps:

1. Generate initial values for the parameters, $\vec{\lambda}_o$.
2. Iterate the following over the index t until the chain $\mathcal{C}$ has converged.
   (a) Generate a candidate parameter vector $\vec{\xi}$ according to a proposal distribution $q(\vec{\xi}|\vec{\lambda}_{t-1})$.
   (b) Compute the Metropolis ratio:

$$r = \frac{p(\vec{\xi})q(\vec{\lambda}_{t-1}|\vec{\xi})}{p(\vec{\lambda}_{t-1})q(\vec{\xi}_t|\vec{\lambda}_{t-1})}. \tag{6.12}$$

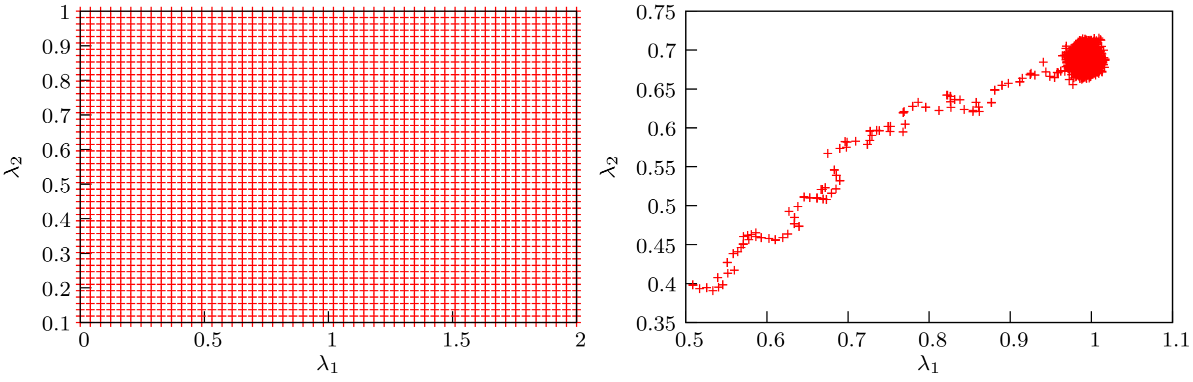

(a) Grid Walk

(b) Random Walk

Figure 6.2: Two strategies for posterior simulation: Figure(a) illustrates a grid walk through parameter space. Here, all points on the predefined grid are utilized. The random walk, Figure(b), is one where a rule, based on the posterior, is used to guide the random jumping through parameter space to the equilibrium position.

(c) Sample from a uniform distribution, $u = U(0\,,1)$

$$\text{if} \begin{cases} r < u & \vec{\lambda}_t = \vec{\lambda}_{t-1} \quad \text{reject} \\ r > u & \vec{\lambda}_t = \vec{\xi}_t \qquad \text{accept} \end{cases}$$

In the first step of the algorithm, initial values for the parameters are chosen and used to calculate the value of the posterior distribution at the point $\vec{\lambda}_0$ in parameter space. The choice of the initial parameter vector effects the convergence speed of the Markov chain. It is an essential property of Markov chains that they be *irreducible*, meaning that starting from all points they must be able to eventually jump to all points in the target distribution [Gre06].

Generating a Candidate

The second step is the iterative part of the algorithm. For each iteration a new candidate parameter vector, $\vec{\xi}$, is generated from the proposal distribution $q\left(\vec{\lambda}_{t-1}\right)$. Some proposal distributions are better suited than others for a given application. For example, if the form of the marginal distributions of the posterior are known in advance, they can be used as the proposal distributions to sample from the full joint posterior distribution. Even if this information is not available, it may be that the choice of one proposal distribution over another results in faster convergence of the Markov chain. Whether this is possible or not is not always obvious, and a certain degree of trial and error is involved in the selection of these distributions. An important practical aspect of the proposal distributions is their tuning. By tuning is understood the following: assume that a Gaussian distribution has been selected for the proposal distribution. According to step 2(a), the previous chain value is the mean, $\vec{\lambda}_{t-1} = \mu$ and the covariance matrix, Σ, determines how strongly each jump is made. The covariance matrix is kept constant throughout the iterations of the algorithm

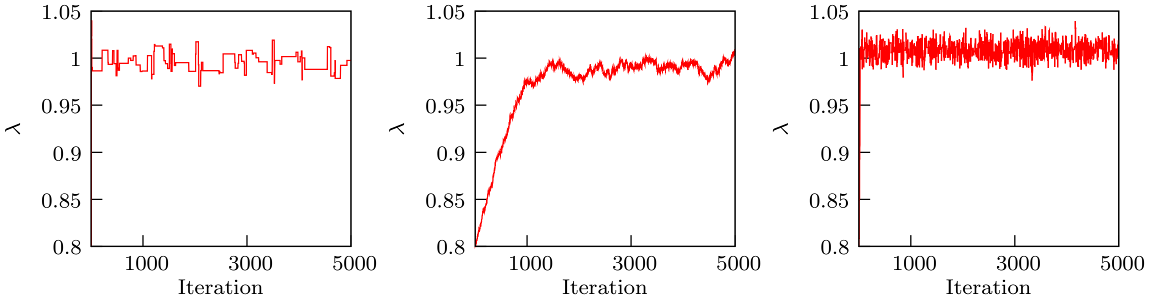

(a) Variance Too Large (b) Variance Too Small (c) Variance Correct

FIGURE 6.3: Effect of proposal standard deviations: This figure depicts the results of "tuning" the proposal distributions or setting their standard deviations. The first frame illustrates the case when the standard deviation is set too large. Few jumps are accepted as seen by the box-like form of the chain. The second frame illustrates the case when the standard deviation is too small. In this case, the chain is accepting too many points and is slow to reach the equilibrium point. Finally, the last frame is the result when the standard deviation is optimally set. Not only does the chain reach the equilibrium point quickly, the noisy-like structure of the chain indicates good mixing properties.

but its value is crucial to the convergence rate of the chain. As illustrated in Figure 6.3a choosing the standard deviation to be too large results in a large portion of jumps being rejected by step 2(c). Even after that chain has found the equilibrium position, it samples poorly from the posterior as is evident by the box-like structure of the chain. If the standard deviation is chosen to be too small, Figure 6.3b, the chain will be slow to converge and will draw samples from the target distribution which results in poor mixing because they are too finely sampled. In either case, letting the chain run for a longer length of time (even if it requires Hubble time!) will eventually result in good mixing. The goal is to select the proposal covariance matrix such that convergence and good mixing occur quickly, such as in Figure 6.3c. Here, the chain quickly moves to the equilibrium position and mixes quite well as seen by the chain's noisy appearance. This is a non-trivial task and many methods, collectively known as "adaptive Metropolis" have been developed to tackle the problem [HST05, HLMS06, RR06].

Matlab Implementation

Before explaining the other steps of the algorithm, I provide some example Matlab code which illustrates the first few steps of the Metropolis algorithm. For the quantum state reconstructed in this thesis implementing the MCMC using Matlab on a standard PC proved sufficient. For more computationally intensive problems, however, a lower level language such as C should be considered.

In this example, `length_chain`, specifies the number of desired samples to be simulated from the posterior. The line, `newpar = oldpar + randn(1, npar)*R;`, generates the candidate vector in Step 2(a). Here I am using a Gaussian proposal distribution whose mean value corresponds to the previous point in the chain and the strength of the jumping is given by `R`, which is the Cholesky decomposition of the covariance matrix containing the jumping parameters. Code lines 7 and 10 calculate the log-likelihood and log-prior, respectively and are problem specific. In the next few paragraphs, I will now explain how the criterion to accept a candidate works and is implemented.

```
1  for idx = 2:length_chain
2
3      % Generate candidate
4      newpar = oldpar + randn(1, npar)*R;
5
6      % Calculate log-likelihood
7      newLogLik = compute_loglikelihood(newpar, data);
8
9      % Calculate log-prior
10     newLogPrior = compute_logprior(newpar);
11
12 end
```

Accepting a Candidate

Steps 2(b) and 2(c) are essential in understanding how the MCMC actually works. First, in step 2(b) the quantity r, known as the Metropolis ratio, is calculated. There are two parts to the Metropolis ratio. The first part corresponds to the ratio between the posterior evaluated at the current position and the posterior evaluated at the candidate position

$$\frac{p(\vec{\xi})}{p(\vec{\lambda}_{t-1})}. \tag{6.13}$$

This quantity is responsible for moving the chain to that region of parameter space where the posterior is sharply peaked. It does this by weighting more heavily those samples drawn from the proposal distribution that are on or near the peaks in parameter space. A graphical representation of this effect can been seen in Figure 6.2b. It shows the evolution of the chain gradually moving to a concentrated region of parameter space. The samples drawn from the proposal distribution that correspond to this blob are favored in comparison to the other areas. In this way, the chain finds its way through the valley and eventually to the hill.

The second part of the Metropolis ratio corresponds to the ratio of the proposal distribution evaluated at the previous position to the proposal distribution evaluated at the candidate position

$$\frac{q(\vec{\lambda}_{t-1}|\vec{\xi})}{q(\vec{\xi}_t|\vec{\lambda}_{t-1})}. \tag{6.14}$$

This part of r is responsible for ensuring that once the chain has found a peaked region of posterior, the previous sample drawn from the proposal distribution is just as likely to be obtained as the current sample. The point is illustrated in Figure 6.4. Depicted in the figure are two different proposal distributions with mean values corresponding to the currently sampled value, $\vec{\lambda}_t$ and the previously sampled value $\vec{\lambda}_{t-1}$ each with standard deviation σ. The

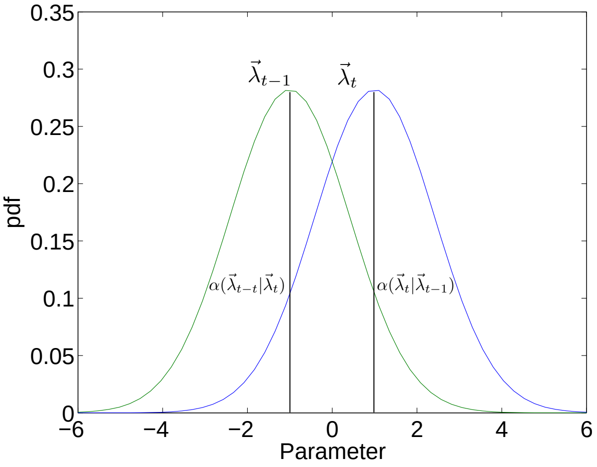

Figure 6.4: Behavior of proposal distributions: The proposal distribution is responsible for generating a posterior distribution candidate. Its mean value is given by the previous parameter $\vec{\lambda}_{t-1}$ and its standard deviation, σ, is kept constant. As the chain progresses through parameter space, the proposal distribution shifts its position as illustrated in figure. But the probability of moving either to a new position $\vec{\lambda}_t$ or jumping back to the old position $\vec{\lambda}_{t-1}$ remains the same. This results in the property of the resulting chain known as irreversibility and ensures that no one area of posterior space is preferred.

standard deviation remaining constant throughout all iterations of the algorithm guarantees that both mean values will have the same probability of being selecting since the heights of the distributions are the same. A further consequence has to do with the conditional probabilities $\alpha(\vec{\lambda}_{t-1}|\vec{\lambda}_t)$ and $\alpha(\vec{\lambda}_t|\vec{\lambda}_{t-1})$. These represent the probability of obtaining the previous sample, $\vec{\lambda}_{t-1}$, given the current sample, $\vec{\lambda}_t$, and the probability of obtaining the current sample $\vec{\lambda}_t$ given the previous sample $\vec{\lambda}_{t-1}$, respectively. Since the proposal distributions are symmetric, these probabilities are equal. This implies that the chain is *reversible*, no single point is more favored to be drawn from the sample distribution than any other.

The final step in the Metropolis-Hastings algorithm is to decide whether or not to accept the candidate $\vec{\xi}$. This is achieved by comparing the Metropolis ratio, r, to some random probability, u, drawn from a uniform distribution, $U(0,1)$. If $r \gg u$ this means that the proposed position corresponds to a more sharply peaked region of posterior than the previously accepted value so the jump should be accepted. If $0 < r < 1$ than there is a chance that proposed jump may not be accepted. Finally, if $r \ll u$ than the jump is definitely rejected. The combined effect is to sample from the posterior distribution.

Matlab Implementation

The final steps of the MH algorithm can be implemented using very little code. The program given above is extended by adding the following few lines. The second line of this program snippet corresponds to step 2(b). Since the logarithm of both the likelihood and prior are usually calculated, the ratio of the posteriors becomes a difference and the product of the likelihood and prior become a sum. The decision whether to accept or to reject the candidate point is made in lines 5 through 8. Line 5 computes the acceptance probability and line 8 compares it to a random probability; deciding whether to accept or reject the candidate. In this implementation of the MH algorithm, the decision to reject a candidate point corresponds to retaining the current position.

```
1       % Compute Metropolis ratio
2       r = (newLogLik – oldLogLik) + (newLogPrior – oldLogPrior)
3
4       % Compute the acceptance probability
5       alpha = min(1, exp(r));
6
7       % 1.) Accept the jump if following condition holds
8       if (rand < alpha)
9          acce = acce + 1;
10         oldpar = newpar;
11         oldLogLik = newLogLik;
12      end
13
14      % Update the chain
15      chain(i,:) = oldpar;
```

It is for this reason that in Figure 6.3a poor mixing is indicated by a box-like structure in the chain. This means that many candidate points have been rejected and only the current position is being retained.

The MH sampler is simple to implement but has some draw backs. Practically, selecting the covariance matrix for the proposal distributions is not obvious. Additionally, for correlated parameters and high dimensional sampling, the MH algorithm is known to produce poor mixing [HST05]. Other methods can be found in the text [GRS96]. For now, I will apply all of the ideas and code presented in this chapter to a real life example of quantum state reconstruction using phase-diffused squeezed states as the test bench. These results were published in [DMF$^+$09] and represent a new approach to this typical problem.

6.3 Reconstructing a Phase-Diffused Squeezed State

The phase-diffused squeezed states are an example of a quantum states which posses a non-Gaussian Wigner function. Since the covariance matrix is no longer a complete description of the state, full tomography would have to be performed. They arise when squeezed sates are transmitted over de-phasing quantum channels such as optical fibers affected by thermal fluctuations. Since, however, the state can be completely modeled, the problem of complete tomography is reduced to estimating just a few parameters. The uncertainty on these parameters is just as important to determine as the parameters themselves and will be quantified by the posterior distribution. I now go step by step and illustrate how this estimation can be solved within the Bayesian paradigm.

6.3.1 Deriving the Posterior

The first step is to construct the likelihood function for the quantum estimation problem. A general measurement on a quantum system can be described by the so-called positive operator-valued measure (POVM). Each possible measurement outcome j is associated with a POVM element Π_j which is a positive semidefinite operator. The probability of outcome j can be calculated as $P_j = \mathrm{Tr}[\Pi_j \rho(\vec{\lambda})]$ where $\rho(\vec{\lambda})$ denotes the density matrix of the measured quantum system that depends on the model parameters $\vec{\lambda}$. Since the total probability of some outcome is 1, the POVM elements sum up to the identity operator, $\sum_j \Pi_j = 1$. This generic framework in particular encompasses a tomographic reconstruction of the state $\rho(\vec{\lambda})$ that consists of several different measurements M with possible outcomes indexed by l_M. Then $j = (M, l_M)$ becomes a multi-index indicating both the measurement setting and the measurement outcome for a given setting. Let n_j denote the observed number of measurement outcome j and $N = \sum_j n_j$ represents the total amount of collected data. The likelihood function $\mathcal{L}$ is the probability of observation of a particular set $\{n_j\}$ for a given $\vec{\lambda}$. It follows that $\mathcal{L}$ is given by a multinomial distribution and reads

$$\mathcal{L} = N! \prod_j^N \frac{P_j^{n_j}}{n_j!}. \tag{6.15}$$

In terms of the constituents of Bayes' theorem the theoretical probabilities $\{P_j\}$ are functions of the parameters which are to be determined. The measured numbers of counts $\{n_j\}$ correspond to the data.

The Wigner function for phase-diffused squeezed state is given by

$$W(x,p) = \frac{1}{2\pi\sqrt{V_x V_p}} \int_{-\infty}^{\infty} \exp\left[-\left(\frac{x_\phi^2}{2V_x} + \frac{p_\phi^2}{2V_p}\right)\right] \Phi(\phi)\, d\phi, \tag{6.16}$$

where $x_\phi = x\cos\phi + p\sin\phi$, $p_\phi = p\cos\phi - x\sin\phi$ with x and p as the standard position and phase quadratures and ϕ representing the random phase shifts distributed according to some probability distribution $\Phi(\phi)$. Let V_x represent the variance of the squeezed quadrature and V_p for the variance of the anti-squeezed quadrature. The variances are normalized such that for vacuum state we have $V_x = V_p = 1$ and the state is squeezed in the x quadrature if $V_x < 1$. In quantum state tomography, several different different rotated quadratures x_θ, where θ defines a specific measurement setting are measured. The theoretical homodyne probability density distribution $p(x_\theta)$ can be calculated from Wigner function as a marginal distribution. Integration of $W(x,p)$ over the conjugate quadrature p_θ yields, after some algebra

$$p(x_\theta) = \frac{1}{\sqrt{2\pi}} \int_{-\infty}^{\infty} \frac{1}{\sqrt{\tilde{V}(\phi)}} \exp\left[-\frac{x_\theta^2}{2\tilde{V}(\phi)}\right] \Phi(\phi - \theta)\, d\phi, \tag{6.17}$$

where $\tilde{V}(\phi) = V_x\cos^2\phi + V_p\sin^2\phi$.

The data from each measurement is binned into L bins whose lower boundaries are defined by $Q_{\theta,l}$. The outer bins extend to infinity and we set $Q_{\theta,1} = -\infty$ and $Q_{\theta,L+1} = \infty$. The corresponding theoretical probability $P_{\theta,l}$ is given by integration of the probability density (6.17) over the bin

$$P_{\theta,l}(\vec{\lambda}) = \int_{Q_{\theta,l}}^{Q_{\theta,l+1}} p(x_\theta) dx_\theta. \tag{6.18}$$

Experimentally, two quadrature measurements were performed and the results formed into histograms each containing a total of $L = 70$ bins. From the perspective of direct data inversion this corresponds to an overdetermined system, because there are only three real parameters to estimate, c.f. below.

The POVM elements describing such binned homodyne detection can be expressed as

$$\Pi_{\theta,l} = \int_{Q_{\theta,l}}^{Q_{\theta,l+1}} |x_\theta\rangle\langle x_\theta| dx_\theta, \tag{6.19}$$

where $|x_\theta\rangle$ is an eigenstate of quadrature operator x_θ. Note that, by definition, the sum of theoretical probabilities over all bins is equal to one

$$\sum_l P_{\theta,l}(\vec{\lambda}) = 1. \tag{6.20}$$

This is a mathematical expression of the fact that the homodyne detection always yields some outcome and, after each measurement, one of $n_{\theta,l}$ is increased by one. Put in a different way, the homodyne detection is described by a complete POVM (6.19) whose elements $\Pi_{\theta,l}$ satisfy the condition $\sum_l \Pi_{\theta,l} = 1$.

Assuming the phase noise distribution, $\Phi(\phi)$, is a zero mean Gaussian, the state can be completely characterized by just three parameters $\vec{\lambda} = \{V_x\,, V_p\,, V_\phi\}$ where V_ϕ is the variance of the random phase shifts. The quantum log-likelihood function for the phase diffused squeezed states is finally obtained by taking the natural logarithm of Eq. (6.15) yielding

$$\Lambda = \sum_{\theta,l} n_{\theta,l} \ln \left[P_{\theta,l}(\vec{\lambda}) \right], \tag{6.21}$$

where, for simplicity, all terms that do not depend on the parameter values are ignored.

The prior is chosen by considering the possible values of the parameters to be determined. Since the parameters to be determined in this case are variances, their values must be greater than zero. In order to assume relative ignorance in the value the parameters could take, we use a prior which only requires the variances to be positive and satisfy the Heisenberg uncertainty relation, $V_x V_p \geq 1$. Since the likelihood in this analysis is a sharply peaked function the choice of uniform priors has negligible effect on the numerical results of the MCMC [1].

6.4 Description of the Experiment

The full details of the setup are provided in [FHD+06] and will be summarized here. The squeezing source was an optical parametric amplifier (OPA) constructed from a type I non-critically phase-matched MgO:LiNbO$_3$ crystal inside a standing wave resonator, similar to

---

[1] Since the parameters are variances the actual priors should be determined by using Jeffrey's Principle of Invariance. However, as stated, the implementation of flat priors on $\vec{\lambda}$ in this case has negligible effect.

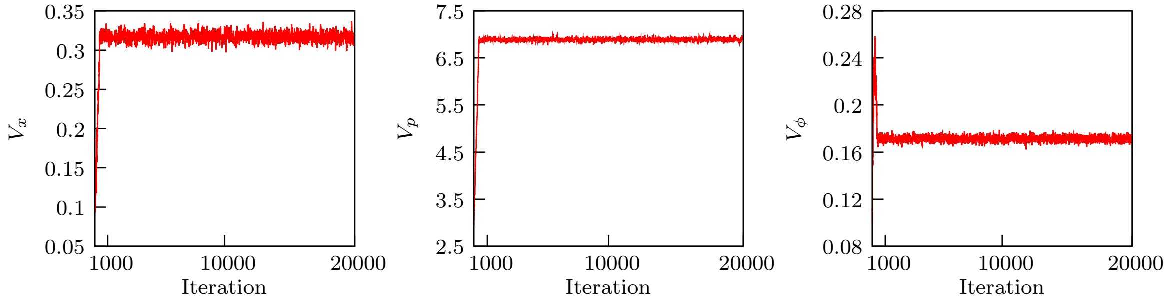

(a) Marginalized Chain: V_x (b) Marginalized Chain: V_p (c) Marginalized Chain: V_ϕ

FIGURE 6.5: Markov chains: This figure depicts the evolution of the Markov chains where the abscissa represents the iteration number and the ordinate represents the value of the chain. After an initial "burn-in" period, in which the chains head to their steady-state positions, the chains eventually converge to a region of parameter space and begin to sample from the posterior distribution. The proposal distributions were taken to be Gaussian with the standard deviations $\Sigma_x = 0.0042$, $\Sigma_p = 0.022$, $\Sigma_\phi = 0.0037$ corresponding to the squeezing parameter, the anti-squeezing parameter and the phase noise parameter, respectively. The starting values were randomly chosen with the only constraint that they be non-negative and obey $V_x V_p \geq 1$. The chains settled to their equilibrium positions with means of $\mu_x = 0.316$, $\mu_p = 6.888$, and $\mu_\phi = 0.171$ corresponding to the squeezing, anti-squeezing and phase noise parameter respectively.

the design that previously has been used in [Che07]. The OPA was pumped with 50 mW of green light at 532 nm resulting in a classical gain of about 11. The length of the OPA cavity as well as the phase of the second harmonic pump beam were controlled using radio-frequency modulation/demodulation techniques. The mode cleaner was operated in high finesse mode $\mathcal{F} = 10500$ resulting in a line width of 55 kHz. A non-classical noise power reduction of slightly more than 5.0 dB was directly observed with a homodyne detector in combination with a spectrum analyzer at a Fourier sideband frequency of 6.4 MHz.

The phase noise was induced by reflecting the squeezed field from a piezo-electric transducer (PZT) mounted high-reflection mirror that was quasi-randomly moved. The voltages applied to the PZTs were produced as follows. An independent random number generator produced data strings with a Gaussian distribution. The strings were digitally filtered to limit the frequency band to 2–2.5 kHz. The output interface was a common PC sound card with SNR of -110 dB. The sound volume was set to meet the desired standard deviation of channel phase noise.

Homodyne detection confirmed that the squeezing degraded in the same way when phase noise was increased. The detector difference currents were electronically mixed with a 6.4 MHz local oscillator. The demodulated signals were then filtered with a 400 kHz bandwidth low-pass filter and sampled with one million samples per second and 14 bit resolution using a National Instruments analog-digital sampling card.

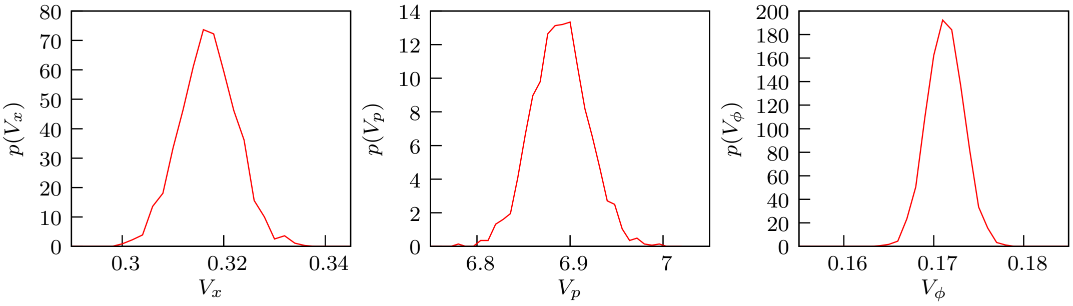

FIGURE 6.6: Marginalized posterior distributions: Each probability density was calculated using every tenth point from the marginalized chains corresponding to 1900 data points. The standard deviation of each density are $\sigma_x = 0.0056$, $\sigma_p = 0.0289$, and $\sigma_\phi = 0.0020$ corresponding to the squeezing parameter, the anti-squeezing parameter and the phase noise parameter, respectively.

6.5 Sampling from the Posterior

The goal of the Bayesian reconstruction scheme is the calculation of marginalized posterior distributions on the model parameters $\vec{\lambda} = \{V_x, V_p, V_\phi\}$. Since Bayes' theorem, Equation (6.10), states that this is proportional to the likelihood function times the prior distribution, both of which can be computed for a given set of parameters, the Metropolis-Hastings sampler can be used to draw samples from it.

6.5.1 Results of the MCMC

Figure 6.5a-c depicts the resulting chains after 20,000 iterations of the MCMC algorithm. The abscissa represents the number of iterations of the MCMC and the ordinate represents the parameter values. After an initial "burn-in" period of approximately 1000 iterations, in which the chain heads towards equilibrium, the chain converges and begins to sample from the posterior distribution (which in this Gaussian case also includes the region of maximum-likelihood). The development of criteria for the determination of chain convergence is a general problem which has been the subject of much research [BG98, EAFB06]. The general idea is to run multiple chains per estimation parameter and monitor their evolution both within each change and across each change. Convergence is inferred if all chains behave consistently. With respect to the case at hand, convergence of the chain can be inferred by comparing the locations to which the marginalized parameter chains have settled with the independent measurement of the V_x, and V_p parameter values performed with a spectrum analyzer. In the absence of such an independent measurement, the criteria in [BG98, EAFB06] can be used to infer convergence.

The width of the marginalized chains, i.e. their standard deviations, quantify the degree of uncertainty on the value of each parameter. By forming histograms of the chain as a function of each of the parameters their marginalized posterior probability distributions are obtained as shown in Figure 6.6. From these posteriors the following uncertainties on the model parameters: $\sigma_x = 0.0056$ for the squeezing parameter, $\sigma_p = 0.0289$ for the anti-squeezing parameter and finally $\sigma_\phi = 0.0020$ for the phase noise parameter are obtained.

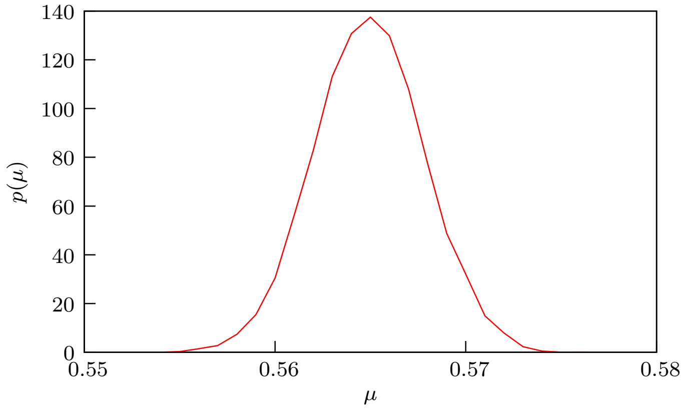

Figure 6.7: Reconstructed purity posterior distribution: The purity was calculated using the resulting Markov chain of 1900 parameter values and Equation (6.22). This results in a probability density function which exactly quantifies the uncertainty on the estimation of the purity. The purity is calculated to be $\mu = 0.5649 \pm 0.0028$. No such result is possible with a pure maximum-likelihood approach.

The proposal distributions, from which the posterior distribution samples have been drawn, were chosen to be Gaussians with the following standard deviations $\Sigma_x = 0.0042$, $\Sigma_p = 0.022$, $\Sigma_\phi = 0.0037$ corresponding to the squeezing parameter, anti-squeezing parameter and phase noise parameter, respectively. These values were obtained through manual tuning of the MCMC algorithm. This is done by adjusting the individual standard deviations, i.e. Σ_x, Σ_p, Σ_ϕ, until the proportion of accepted jumps reaches approximately 44% [GCSR04].

Since the MCMC chain contains a complete statistical description of the parameters, the statistical error on the reconstruction of both the quantum state itself as well as derived quantities from it, e.g. purity, can be exactly determined. This will be illustrated in the next section.

6.5.2 Estimating the State Purity

The Markov chain can be used in further calculations of such properties as the purity of the reconstructed state. Figure 7.15 depicts such a result. Using the analytical definition of the purity

$$\mu = 4\pi \iint W^2 \left(x \, , p\right) \, dxdp, \tag{6.22}$$

and the resulting chain from the MCMC, the purity can be calculated, automatically taking into consideration the statistical error and correlation on the parameters determined by the MCMC. The result is a probability density whose standard deviation quantifies the degree of uncertainty on the estimation of the purity. For the state in question, the purity is $\mu = 0.5649 \pm 0.0028$. It is important to note that this information is delivered directly from the MCMC itself; no additional assumptions as to the distribution of the errors and their correlation properties need to be made. Additionally, any one-dimensional quantity can be calculated in this manner. For example, if estimating the amount of entanglement of a non-Gaussian state, the logarithmic negativity [VW02] can be calculated over the span of the resulting chain. The result will be a probability density quantifying the uncertainty on its value.

6.6 Summary

In this experiment I applied a Bayesian data analysis scheme known as Markov chain Monte Carlo (MCMC) to the tomographic reconstruction of quantum states. Taking phase-diffused squeezed states as an example, I provided the details as to the derivation of the likelihood function as well as to the numerical implementation of the MCMC. The results include a set of probability density distributions which exactly quantify the degree of uncertainty on the estimation of the parameters. Furthermore, using the Markov chain in the calculation of the state's purity enabled the construction of a probability density distribution on the value of the purity, thereby quantifying the degree of uncertainty on its calculation. The MCMC scheme is completely general and can be applied to higher dimensional problems, such as the reconstruction of the density matrix and will be discussed further in the conclusion of the thesis.

I will now present two experiments that deal with quadrature entanglement. The next chapter presents a characterization of free entanglement and how it acts as a quantum communication channel.

7

Entanglement as a Communication Channel

Continuous variable quantum communication channels have been the subject of both theoretical and experimental research for the past few years [CD94, CCMR05, EW, GMVT03, HJSW96, SW97, HW01, WPGG07, ATM$^+$04, GAW$^+$03, SBT$^+$03]. Similar to classical communication channels, quantum communication channels are characterized by a channel capacity. In contrast to classical communication channels, the capacity of quantum communication channels is distinguished by two different quantities; namely, the *classical capacity* which gives the number of classical bits that can be faithfully transmitted per use of the channel and the *quantum capacity* which specifies how many quantum bits can be transmitted per use of the channel [GMVT03, NC00]. One example of a quantum communication channel is a teleportation channel, which is established by a shared entangled state with local operations and classical communication (LOCC) between two distant parties [BK98, BTB$^+$03b]. Of all the possible entangled states that could be used to establish the quantum channel, *Gaussian* states are of particular interest due to their well understood theoretical structure and ability to be easily generated experimentally [EW, WPGG07]. Because these states are characterized by a Gaussian Wigner function, only the second moments collected in the state's covariance matrix (CM) are required in order to completely define the state. Experimentally, this means that only a few tomographic measurements need to be conducted, significantly reducing the effort to measure these states. To date, several groups have conducted experiments only *partially* measuring the CM [WOTBG05, BSLR04, LKOH$^+$05].

In this chapter, I present an experimental study of Gaussian quantum teleportation channels which was published in [DHF$^+$07]. The teleportation channels are established by distributing two different classes of entangled Gaussian states illustrated in Figure 7.1 over a free-space auxiliary channel to two parties, Alice and Bob, together with local operations and classical communication (LOCC). In the experiment, every single parameter of the CMs are measured. These channels are then characterized by evaluating the lower bounds to the quantum channel capacity, the teleportation fidelities of coherent states, and the purities and the logarithmic negativities of the shared entangled states. Additionally, two different entanglement criteria are used-the Simon-Peres-Horodecki and an entanglement witness-to verify that the measured state is in fact entangled. This paper is divided into the following sections. In Section 7.1, I present an efficient experimental procedure for measuring the entire CM using only five measurement settings. The technical details of the experiment are described in Section 7.2. The experimental implementation of the measurement of the entire covariance matrix is discussed in Section 7.3.

The formal definitions of a quantum channel as well as the quantities that characterize them are presented in Section 7.4. The reconstructed CMs from the experimental data are presented in Section 7.5 and finally Section 7.6 contains a discussion of the results.

7.1 Experimental modus operandi

7.1.1 Preliminary Considerations

In order to obtain complete knowledge of a two-mode Gaussian entangled state, it is sufficient to measure its symmetric positive semi-definite ten parameter covariance matrix (CM) [BSLR04, LKOH$^+$05]. In its block form, the CM is given by

$$\gamma = \begin{pmatrix} \mathbf{A} & \mathbf{C} \\ \mathbf{C}^T & \mathbf{B} \end{pmatrix}, \tag{7.1}$$

where **A**, **B** and **C** are 2×2 matrices which contain the parameters describing Alice's mode, Bob's mode and the correlations between their modes, respectively. The CM contains the second moments of a state's quadratures, $\gamma_{jk} = \langle \Delta r_j \Delta r_k + \Delta r_k \Delta r_j \rangle$, where $r = (x_A,\, p_A,\, x_B,\, p_B)$ is a vector of quadrature operators and $\Delta r_j = r_j - \langle r_j \rangle$. We use units such that the covariance matrix of vacuum is equal to the identity matrix. From γ can be obtained information regarding entanglement properties of the state (e.g. verification, quantification) as well as the state's purity. In the case of teleportation channels, the lower bound to the quantum channel capacity and the teleportation fidelity of coherent states can also be obtained from the CM.

For applications such as monitoring of quantum communication channels it is highly desirable to develop techniques such that the reconstruction of a state's CM can be accomplished with the fewest possible measurements. Some of these techniques I discuss in Chapter 8. To this end, the structure of the matrix itself can be exploited such that only two measurement settings yield six of the ten independent parameters (simultaneous measurement of the amplitude quadrature of one mode and the phase quadrature of the other mode). Besides these more technical considerations there are a number of fundamental issues that must be addressed. These have been elaborated upon by van Enk *et al.* [vELK07] who gave five criteria that should be obeyed when conducting an entanglement experiment. The heart of the criteria is not to assume too much as to the form, symmetry or repeatability of the entanglement source for each copy that it produces. The effect of not satisfying these criteria is to increase the risk of overestimating/underestimating the amount of entanglement present in the generated state. Any entanglement verification protocol should satisfy

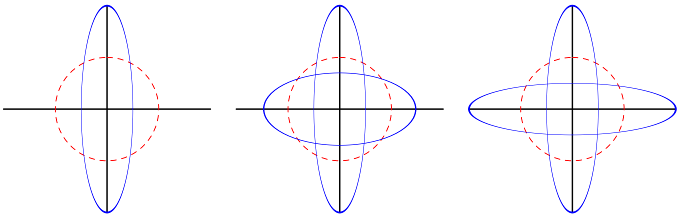

V-Class Entanglement M-Class Entanglement S-Class Entanglement

Figure 7.1: Classes of entanglement: This figure depicts three different *classes* of entanglement. V-Class entanglement is formed by mixing a single-mode squeezed state with the vacuum mode on a balanced beam splitter (BBS). M-Class entanglement is formed by mixing two unevenly and oppositely single-mode squeezed beams on a BBS and S-Class entanglement is formed by mixing two equally but oppositely single-mode squeezed beams on a BBS.

these five criteria. The choice of a verification protocol will ultimately depend on the *type* of entanglement generated (or thought to have been generated) in an experiment.

The establishment of a quantum communication channel, such as a teleportation channel, requires the distribution of what van Enk *et al.* have referred to as *a priori* entanglement [vELK07]. This type of entanglement is obtained when a source generates many copies of a bipartite state, ρ_{AB}, such that an entanglement verification protocol can be conducted on a sub-ensemble of them using the rest to perform a quantum information theoretic protocol. A possible verification protocol for *a priori* entanglement is to perform full tomography on the state. This can be achieved using linear optics and homodyne detection [BS97, Leo97]. This allows not only for a qualitative statement as to whether the state is separable or entangled but also a quantitative statement as to how much. Full tomography is expensive, however, especially when its implementation is solely to obtain information about the channel. As such, it is desirable to develop verification protocols that can be conducted using only *partial* tomographic measurements while still satisfying the van Enk criteria. I will now present such a partial tomographic protocol and later in Chapter 8 will show how it can be extended to higher dimensional systems.

7.1.2 Description of the Partial Tomographic Protocol

The partial tomographic protocol (PTP) developed to characterize the teleportation channels can be stated as follows:

1. Alice and Bob simultaneously measure their amplitude and phase quadratures, respectively, while comparing their results by means of classical communication.

2. Alice and Bob simultaneously measure their phase and amplitude quadratures, respectively, while comparing their results by means of classical communication.

3. Alice and Bob measure their amplitude quadratures.

4. Alice and Bob measure their phase quadratures.

5. Alice and Bob simultaneously measure a linear combination of their amplitude and phase quadratures, respectively.

The fact that every parameter of the CM is measured prevents one from making an assumption as to the symmetry of the state being measured. Although measuring only the second moments of the state does not contain information as to whether the state is Gaussian or not, something which in the strictest sense of the van Enk criteria should not be assumed, an entanglement criterion, such as the Simon criterion, is a sufficient criterion for both Gaussian and non-Gaussian states. Furthermore, the quantities such as the secret key rate [GPC06, NGA06] or the lower bound to the quantum channel capacity [WPGG07], while indirectly indicating the presence of entanglement, obtain their lower bounds for Gaussian states. As such, one can at worst only underestimate these quantities by measuring just the second moments and assuming that the state is Gaussian.

7.2 Experimental setup

In the experiment, two-mode entangled states are generated by mixing on a balanced beam splitter two squeezed vacuum beams produced by optical parametric amplifiers (OPAs). The laser source used in the experiment was a continuous-wave non-planar Nd:YAG ring laser with 300 mW of output power at 1064 nm and 800 mW at 532 nm. The latter was used to pump the OPAs to produce two amplitude squeezed light beams with an approximate power of 0.06 mW at 1064 nm. Both OPAs were constructed from type I non-critically phase-matched $\mathrm{MgO} : \mathrm{LiNbO}_3$ crystals inside hemilithic cavities. Each cavity was formed by a HR-coated crystal surface with a reflectivity of $r > 0.999$ and a metal spacer mounted out-coupling mirror with a reflectivity of $r = 0.957$. The intra-cavity crystal surface was AR coated for both the fundamental (1064 nm , r < 0.05%) and the second harmonic (532 nm , r < 0.5%). The out-coupling mirror had a reflectivity of r=0.15±0.02 for 532 nm. The OPAs were seeded through the HR-surface with a coherent laser beam of 15 mW power and pumped through the out-coupling mirror with various intensities, the lowest being 75 mW, corresponding to a parametric gain 5. The length of both OPA cavities as well as the phase of the second harmonic were controlled using radio-frequency modulation/demodulation techniques. The error-signals were derived from the seed fields reflected from the OPA cavities. A maximum value of 4.0 dB of non-classical noise suppression was directly observed using homodyne detection. The shot noise level was defined by mixing the local oscillator with the vacuum mode on a balanced beam splitter and measuring fluctuations of vacuum. The electronic dark noise of the homodyne detectors was approximately 13 dB below the shot noise level making dark noise correction of the observed squeezing superfluous. The visibility on both homodyne detectors was $\eta_{\mathrm{vis}} = 0.965$ and the quantum efficiency of the photodetectors is estimated to be $\eta_{\mathrm{quantum}} = 0.93$ yielding a total detection efficiency of $\eta \approx 0.87$. The phase locks on both the entangling beam splitter and homodyne beam splitters are estimated to be within 3° of the desired values. The photocurrents produced from the homodyne detectors were first demodulated at a frequency of 7 MHz and low-pass filtered with a corner frequency of 30 kHz. It was sampled with a National Instruments sampling card with maximum sampling rate of 1 mega sample per second. By

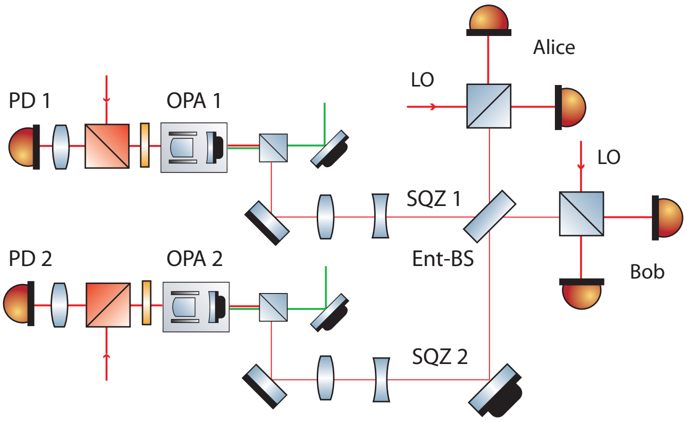

FIGURE 7.2: Experimental setup: The squeezed states are generated by the two optical parametric amplifiers (OPAs) and mixed at the entangling beam splitter (Ent-BS). The different classes of entanglement are generated by adjusting the parametric gain setting of the OPAs. The entanglement is then distributed over a free-space channel to the two homodyne detectors Alice and Bob.

independently changing the parametric gain of each amplifier we can generate all three types of entanglement as illustrated in Fig. 7.1. A diagram of the full experiment is provided in Fig. 7.2.

7.3 Experimental implementation of PTP

The partial tomographic protocol (PTP) was implemented using a custom built data acquisition system whose software component was developed using LabView and whose hardware component was realized by balanced homodyne detection with external addition and subtraction boxes. The homodyne detectors were designed such that there were multiple outputs of both the DC and AC signals generated by each detector. The AC-subtracted signals from both homodyne detectors were fed simultaneously into the LabView program where both the variances of the respective electronic channels as well as the covariance of the two electronic channels were calculated in real-time. This corresponds to the classical communication component of our protocol. Additional information as to which quadratures produced a given covariance was obtained by recording, in real-time, the DC substracted signal from one scanned homodyne detector. This was achieved by locking e.g. Alice's homodyne detector to one quadrature and scanning the phase between the local oscillator and signal beam of Bob's homodyne detector. With this setup, one measurement-e.g. measuring the amplitude quadratures simultaneously-delivered three of the ten required CM parameters.

There are two main features of this implementation that are noteworthy. First, it allows the manual setting of the measurement basis. The basis information can be obtained by looking at the covariance of the two electronic channels. A zero covariance indicates the measurement of two orthogonal quadratures for a symmetric state. Although both the verification and quantification of entanglement is basis independent, the form of the CM is not. For the case of an optimally entangled EPR state, one would expect non-zero parameters for half the elements of the CM in an orthogonal measurement basis. While the choice of a basis is arbitrary, it must be consistent. Failure to measure every parameter of the CM in the same basis is tantamount to random experimental error. Failure to measure some of the parameters in the same basis is systematic error, as it adds a constant offset to only some of the parameters. The implication of these error sources, especially systematic error, is to obtain a false estimate of quantities of interest such as the logarithmic negativity [VW02], or to reconstruct a non-physical state.

Second, systematic error can be reduced. As a result of the real-time evaluation of the covariance between the homodyne detector outputs and the DC subtracted signal from a scanned homodyne detector, one can determine which quadratures are correlated, anti-correlated and not correlated. This information helps to reduce the systematic error because it provides a means by which to adjust the phase angle between the optical local oscillator and signal beam independent of any DC offsets on the error-signal. This contributes to the overall consistency of the entanglement detection.

The method described in this section relies on the subtraction locking scheme introduced in Section 5.2.1. This scheme limits the range of angles that can be set at the entangling beam splitter and homodye detectors. Furthermore, for more complicated preparation schemes, such as for generating a multimode entangled state, the more robust method I introduced in Section 5.2.2 is required.

7.4 Theoretical description of Quantum Communication Channels

In order to more deeply understand the equivalence between a shared entangled state and an established quantum communication channel, such as for a teleportation channel, it is necessary to understand the theoretical structure of quantum communication channels. It is also within this framework that these channels obtain their physical meaning. To this end, this section will review the necessary theoretical concepts in order to understand the experimental results of Sec. 7.5.

A quantum channel is a trace-preserving completely positive map, T, that transforms quantum states according to $\rho \mapsto T(\rho)$ [HW01]. They can be understood to originate as the result of a unitary interaction U of a state, ρ, with the environment described by another Hilbert space $\mathcal{H}_E$ which is in a state, ρ_E,

$$T(\rho) = \mathrm{Tr}_E U(\rho \otimes \rho_E) U^\dagger, \tag{7.2}$$

where Tr_E denotes the partial trace with respect to $\mathcal{H}_E$ [HW01, EW, BL06]. An important subclass of these channels are *Gaussian channels*, which are characterized by a Gaussian unitary U, determined by a quadratic bosonic Hamilitonian, and a Gaussian state ρ_E [EW]. At the level of covariance matrices (CMs), which offer a complete description of Gaussian states and would be measured in all practical applications of continuous-variable quantum information protocols, the action of a channel is given by

$$\gamma \mapsto X^T \gamma X + Y. \tag{7.3}$$

	V-Class		S-Class	
Characteristic	Gain 5	Gain 10	Gain 5	Gain 10
λ	0.033±0.004	0.034±0.003	0.063±0.003	0.175±0.005
λ^{T_A}	-0.317±0.004	-0.349±0.003	-0.600±0.001	-0.566±0.004
$\mathcal{W}$	-0.341±0.004	-0.383±0.003	-0.599±0.001	-0.566±0.004
$E_{\mathcal{N}}$	0.602±0.003	0.700±0.004	1.342±0.005	1.331±0.009
Q_L	-0.071±0.003	-0.059±0.004	0.387±0.005	0.100±0.009
$\mathcal{F}$	0.586±0.003	0.597±0.003	0.701±0.003	0.695±0.005
μ	0.648±0.002	0.563±0.001	0.608±0.002	0.301±0.002
K			0.323±0.005	0.120±0.006

TABLE 7.1: Channel characteristics for entanglement classes: This table summarizes the channel characteristics for each class of entanglement used to establish a teleportation channel. Beginning with the first, they include: the state condition λ, the Simon criterion λ^{T_A}, the optimal entanglement witness $\mathcal{W}$, the log-negativity $E_{\mathcal{N}}$, the lower bound to the quantum channel capacity Q_L, the teleportation fidelity of coherent states $\mathcal{F}$, the purity μ and the secret key rate K.

The condition to ensure that the transformation is completely positive is given by

$$Y + i\Omega - iX^T\Omega X \geq 0, \tag{7.4}$$

where

$$\Omega = \begin{pmatrix} \sigma & 0 \\ 0 & \sigma \end{pmatrix}$$

is the symplectic form with

$$\sigma = \begin{pmatrix} 0 & 1 \\ -1 & 0 \end{pmatrix}.$$

The formula Equation (7.4) represents the necessary and sufficient condition for complete positivity of the Gaussian map given by Equation (7.3), see e.g. Refs. [DVV77, Lin00, EP02, Fiu02, Jam72]. It is possible to interpret this condition as the generalized Heisenberg inequality. According to the Jamiolkowski isomorphism [Jam72], every completely positive map is isomorphic to a positive semidefinite operator on the tensor product of Hilbert spaces of input and output states. In the case of Gaussian CP maps this operator becomes and infinitely squeezed Gaussian state characterized by matrices X and Y. The generalized Heisenberg inequality for the covariance matrix of this state is equivalent to Equation (7.4), c.f. Ref. [Fiu02].

The usual quantum information protocols, e.g. teleportation and quantum memory, can all be considered as quantum channels [WPGG07]. In this chapter, I consider a special subclass of teleportation channels established by means of a shared entangled state together with local operations and classical communication (LOCC) is considered. An important characteristic of teleportation channels, as well as quantum channels in general, is their capacity to transmit *quantum information*, quantified in units of qubits. To this end the *quantum capacity* [EW, Sho02, Dev05, Llo97] of an arbitrary channel, T, is given by

$$Q\left(T\right) = \lim_{n\to\infty} \frac{1}{n} \sup_{\rho} J\left(\rho\,, T^{\otimes n}\right), \tag{7.5}$$

$$J\left(\rho, T\right) = S\left(T\left(\rho\right)\right) - S\left(\left(T \otimes \mathrm{id}\right)\left(\psi\right)\right), \tag{7.6}$$

where ψ is a purification of ρ and J is known as the *coherent information.* The coherent information was first introduced by Schumacher and Nielsen in connection with error correction [SN96]. With regard to its operational interpretation, the coherent information quantifies the amount of information the environment has obtained about the state transversing it. Another information theoretic quantity related to the coherent information is the *quantum conditional entropy* [SW72, HOW05, HOW06] defined by

$$S\left(B \mid A\right) = S\left(\rho_{AB}\right) - S\left(\rho_A\right), \tag{7.7}$$

where $S(\rho_{AB})$ and $S(\rho_A)$ stand for the von Neumann entropies of the total state ρ_{AB} and the part of the total state held by Alice, ρ_A, respectively. The conditional entropy quantifies the amount of quantum information Bob must send to Alice such that she can recreate the total state, ρ_{AB}, given her prior knowledge of it, as quantified by $S\left(\rho_A\right)$. As such, the conditional entropy quantifies Alice's ignorance of the total state. The coherent information, Equation (7.6), depends on both the channel, T, as well as on the input state, ρ, to the channel. In order to evaluate the quantum capacity of an arbitrary channel, T, the coherent information must be maximized over all possible input states and regularized over many uses of the channel. For teleporation channels, where T would correspond to a shared entangled state with CM γ, however, a lower bound to the quantum capacity can be obtained by first applying a distillation protocol to the state in order to obtain k maximally entangled pairs of quantum bits (ebits). The teleportation protocol could then be conducted using these ebits. It was shown by Wolf *et al.* [WPGG07] that the number of ebits that can be obtained from a given state with CM γ can be bounded from below by the right hand side (RHS) of

$$Q\left(T\right) \geq S\left(\gamma_A\right) - S\left(\gamma\right) \equiv Q_L, \tag{7.8}$$

which in turn gives a lower bound to the quantum channel capacity. Here $S(\gamma)$ denotes the von Neumann entropy of a Gaussian state with CM γ. The development of entanglement distillation protocols is an active area of current research. To date, both single copy and iterative entanglement distillation have been experimentally demonstrated as well as single and multicopy squeezing purification [HFD$^+$07, HSD$^+$08, FHD$^+$06].

In addition to the quantum capacity, there are a number of other quantities that contribute to the characterization of teleportation channels. To begin with, the state condition, defined by

$$\gamma + i\Omega \geq 0, \tag{7.9}$$

where Ω is again the two-mode symplectic form, determines whether the reconstructed CM corresponds to a physical state [Sim00]. We define λ as the minimum eigenvalue of $\gamma+i\Omega$ and the inequality (7.9) holds iff $\lambda \geq 0$. In order to verify that the channel has been established using entanglement, the Simon-Peres-Horodecki (Simon) criterion [Sim00] can be used and can be formulated as

$$\gamma^{T_A} + i\Omega \geq 0, \tag{7.10}$$

where $\gamma^{T_A} = \Lambda\gamma\Lambda$ is the CM of a state partially transposed with respect to Alice's mode and $\Lambda = \mathrm{diag}\,(1,-1,1,1)$ corresponds to a local time reversal operation on Alice's phase quadrature only. Similarly as before, λ^{T_A} is defined as the minimum eigenvalue of $\gamma^{T_A} + i\Omega$. If $\lambda^{T_A} < 0$ then the state is entangled. In addition to the Simon criterion, an optimal entanglement witness, $\mathcal{W}$, was determined by solving the corresponding semi-definite program [HE06]. The amount of entanglement was quantified using the logarithmic negativity [VW02], defined by

$$E_{\mathcal{N}} = \log_2 \parallel \rho^{T_A} \parallel, \tag{7.11}$$

where a basis 2 sets the units to bits. The teleporation fidelity for coherent states [Fiu02] is given by

$$\mathcal{F} = \frac{2}{\sqrt{\det\mathbf{E}}}, \tag{7.12}$$

where the matrix $\mathbf{E}$ reads

$$\mathbf{E} = 2\mathbf{D} + \mathbf{R}\mathbf{A}\mathbf{R}^T + \mathbf{R}\mathbf{C} + \mathbf{C}^T\mathbf{R}^T + \mathbf{B}, \tag{7.13}$$

and the matrices $\mathbf{A}$, $\mathbf{B}$, $\mathbf{C}$ and $\mathbf{C}^T$ are obtained from the CM given by Eq. (7.1) with

$$\mathbf{R} = \begin{pmatrix} 1 & 0 \\ 0 & -1 \end{pmatrix}. \tag{7.14}$$

The purity of the state is defined by $\mu = \mathrm{Tr}[\rho_{AB}^2]$ and for Gaussian states we have

$$\mu = \frac{1}{\sqrt{\det\gamma}}. \tag{7.15}$$

Finally the achievable secret key rate for entangled state-based quantum key distribution protocol where Alice and Bob both measure certain quadrature using local homodyne detections on their parts of the shared two-mode state is evaluated. From the knowledge of the covariance matrix γ a lower bound on the achievable secret key rate can be calculated by assuming that the state is Gaussian and using the following formula,

$$K = I_{AB} - \chi(A:E). \tag{7.16}$$

Here I_{AB} is the classical mutual information between Alice's and Bob's measured data and $\chi(A:E)$ denotes the Holevo bound between Alice and an eavesdropper Eve [GPC06, NGA06]. This latter quantity can be expressed as $\chi(A:E) = S(\rho_{AB}) - S(\rho_B^a)$, where ρ_B^a is a normalized density matrix of Bob's mode conditional on Alice's measurement outcome a. Note that for Gaussian states and homodyne detection $S(\rho_B^a)$ does not depend on the measurement outcome a which justifies the use of the above expression.

7.5 Experimental Results

The partial tomographic protocol (PTP) presented in Section 7.1.2 was used to characterize teleportation channels established by two different classes of distributed bipartite entanglement. Data acquisition was performed using a LabView program. One million data points were recorded per measurement setting. The data was then divided into ten separate data blocks each with 100,000 points. Covariance matrices were generated from each of the ten and averaged yielding an average CM. For each CM, the channel characteristics were calculated and averaged. The standard error was then calculated for the 95% confidence interval. With respect to the CMs, this ranged from ±0.001 to ±0.01. The first class, to be known as V-class entanglement, was formed by mixing a single-mode squeezed vacuum state with the vacuum mode on a balanced beam splitter. According to the formalism presented by Wolf *et al.* [WEP03], this represents the optimal entangling scheme for these input states. This experiment was conducted for a parametric gain setting of 5 and a parametric gain setting of 10. The reconstructed V-Class covariance matrix (CM) for the parametric gain 5 setting is given by

$$\begin{pmatrix} 0.751 & -0.146 & 0.307 & -0.000 \\ -0.146 & 3.175 & -0.000 & -2.129 \\ 0.307 & -0.000 & 0.706 & -0.102 \\ -0.000 & -2.129 & -0.102 & 3.181 \end{pmatrix}.$$

The channel characteristics are presented in Table 7.1. They include in order of appearance: the state condition Equation (7.9), the Simon criterion Equation (7.10), an optimal witness; the logarithmic negativity Equation (7.11), the lower bound to the quantum channel capacity Equation (7.8), the teleporation fidelity of coherent states Equation (7.12), and the purity of the entangled state Equation (7.15). The state condition demonstrates that the reconstructed CM is a bona fide CM i.e., that the CM corresponds to a physical state. This serves as an indicator if the measurement has been conducted correctly. Both the Simon criterion and entanglement witness serve as a check if the state is separable or entangled. The advantage of using an entanglement witness is that it corresponds to the optimized measuring device that can be reconstructed from the measured data [HE06]. As a result of this optimization, measuring a witness may involve even fewer measurement settings in order to optimally detect the entanglement of the state.

The V-class parametric gain 10 CM reads

$$\begin{pmatrix} 0.686 & -0.054 & 0.326 & 0.003 \\ -0.054 & 4.625 & 0.001 & -3.584 \\ 0.326 & 0.001 & 0.678 & -0.031 \\ 0.003 & -3.584 & -0.031 & 4.681 \end{pmatrix},$$

with the corresponding channel characteristics also given in Table 7.1. In both cases, the lower bound to the channel capacity is negative. The teleporation fidelities, $\mathcal{F}$, both being greater than 1/2, indicate the presence of entanglement. The negative values for the Simon criterion and entanglement witness clearly show the measured state was entangled.

The second class of entanglement generated, to be known as S-Class entanglement, was established by mixing two equally but oppositely squeezed beams on a balanced beam splitter. For ideal pure squeezed states this would yield the two-mode squeezed vacuum state. The reconstructed S-Class CMs for the parametric gain 5 and 10 settings read

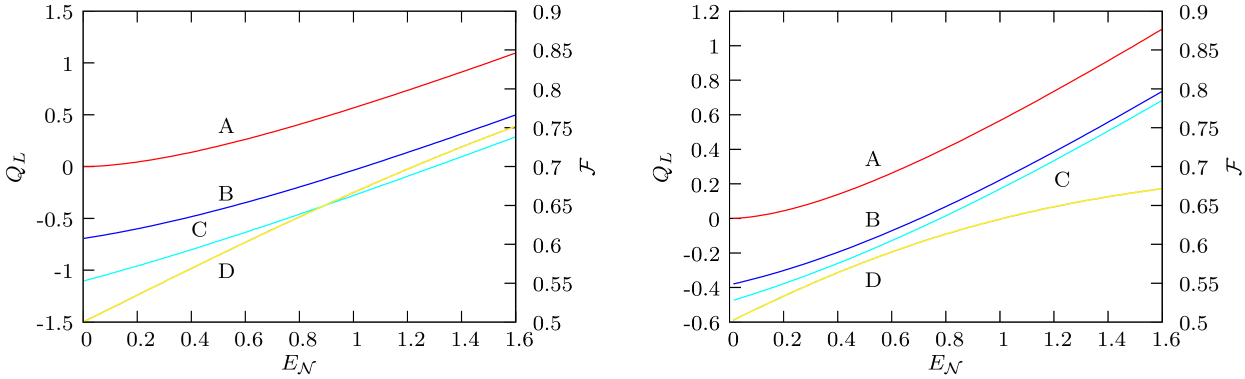

(a) S-Class Entanglement: Channel properties

(b) V-Class Entanglement: Channel properties

Figure 7.3: Channel properties: This plot depicts the dependence of the lower bound to the quantum channel capacity, Q_L on the purity of the entangled state, where A is $\mu = 1$, B is $\mu = 0.5$ and C is $\mu = 0.2$, and the amount of entanglement. Interesting for the application of a state merging protocol or to obtain a positive secret key rate, is the point at which Q_L becomes positive. It is seen that as the purity of the state decreases, more entanglement is required for it to become positive. Curve D is the fidelity for each case.

$$\begin{pmatrix} 2.359 & 0.132 & 1.885 & 0.028 \\ 0.132 & 2.205 & 0.008 & -1.883 \\ 1.885 & 0.008 & 2.266 & 0.372 \\ 0.028 & -1.883 & 0.372 & 2.427 \end{pmatrix},$$

and

$$\begin{pmatrix} 4.200 & -0.090 & 3.773 & -0.033 \\ -0.090 & 4.462 & 0.035 & -4.216 \\ 3.773 & 0.035 & 4.228 & -0.208 \\ -0.033 & -4.216 & -0.208 & 4.842 \end{pmatrix},$$

respectively. The corresponding channel characteristics are listed in the third and fourth columns of Table 7.1, respectively. Comparing the two log-negativities of the V-Class and S-Class entangled states, it is seen that the introduction of another squeezed beam increases the amount of entanglement for the same gain setting roughly by a factor of 2. The lower bound to the quantum capacity also now shows a positive value for each S-Class state. The sign of Q_L is dependent on both the purity of the state as well as on the amount of entanglement, a relationship that will be explored more fully in Sec.7.6. The fidelities are both greater than 0.5, indicating the presence of entanglement. The fidelity of the gain 5 S-Class state, $\mathcal{F} = 0.701$, breaks the 2/3 no-cloning limit, which is experimentally significant [GG01, BTB$^+$03a]. The difference of purities can be understood when considering that for V-Class entanglement the vacuum mode introduces only a fixed amount of noise whereas for S-Class entanglement, the extra noise introduced into the entangled state in the form of anti-squeezing is not fundamentally bounded.

As a final result, a positive secret key rate was obtained from both S-Class states. With a resolution bandwidth of 50kHz, 16.1kbit/s of a secure key could be extracted using the channel established by the parametric gain 5 setting. This shows that the S-Class entangled states can be used for continuous variable quantum cryptography. Additionally, drawing on the recent results of Horodecki *et al.* [HOW05, HOW06], the positive Q_L's indicate that *state merging* can be achieved using only local operations and classical communication.

7.6 Discussion

The experimental results highlight a relationship between the purity, log-negativity and the lower bound to the quantum channel capacity Q_L. This relationship is made explicit in the numerical results presented in Figure 7.3a-b. The Q_L for S-Class entanglement is shown for three different purities in Figure 7.3a. It is seen that for pure states i.e., $\mu = 1$, the presence of entanglement ensures a positive Q_L. As the purity of the state decreases, the zero crossing is shifted towards higher levels of entanglement. The teleportation fidelity, plotted on the second abscissa, is independent of the purity of the state (assuming that the channel has been properly homodyned). The purity dependence of the Q_L can be further investigated by looking at its behavior for a second class of entanglement. The Q_L for V-Class entanglement is also shown in Figure 7.3b. It is readily seen that the zero crossing for less than pure states occurs at lower levels of entanglement than for S-Class entanglement. Although all both entangled states are bipartite Gaussian states, their utility is very much dependent on their underlying construction.

7.7 Summary

In this chapter, I presented an efficient method for the characterization of Gaussian communication channels with which the *entire covariance matrix* can be measured. This method was applied to two different classes of continuous variable entangled states which were used to establish a teleportation channel between distant parties. The lower bound to the quantum channel capacity as well as other characteristics of the channel were evaluated from the reconstructed covariance matrix. The relationship between the purity, entanglement class, and quantum channel capacity were explored numerically. Two of the established teleportation channels delivered both a positive Q_L as well as a positive secret key rate.

8

Experimental Demonstration of Gaussian Bound Entangled States

In this chapter I present the experimental preparation of unconditional continuous-variable Gaussian bound entangled states. Unlike in the discrete variable regime where often the preparation of a quantum state occurs only after post-selection of the data, the unconditional preparation of the state means that multiple copies of the state are present at the moment of detection. This proof-of-principle demonstration of bound entangled is but one of the results of this experiment. The other result is a demonstration of the complete control over a mutlipartite entangled state. These states are of particular interest for quantum computing since cluster states are an example of CV multipartite entanglement [Nie04]. Additionally, more elaborate schemes could be developed for quantum communication networks now that it is demonstrated how to construct such states. Given these possibilities, I will focus mostly on the experimental procedure implemented to measure bound entanglement and than present the results along with a discussion of the error-analysis.

8.1 Experimental Procedure

The experimental setup is depicted in Figure 8.1. It is composed of three degenerate optical parametric amplifiers (OPAs) as the squeezing source and a network of beam splitters, which together with a piezo mounted mirror (phase-shifter), act as a phase-gate (PHG) and four homodyne detectors labeled “Alice”, “Charlie”, “Bob” and “Domenica” in keeping with the tradition in quantum information to treat each detection stage as a communicating partner. Additionally, there are beam splitters which act as a loss channel to introduce the required amount of extra thermal noise. The result of a numerical search for robust bound entangled states returned a number of different possible candidates Section 4.2. Table 8.1 lists the parameters chosen for the state prepared in this thesis [Pin].

Mode	OPA	Squeezing	Anti-Squeezing	Vx	Vp	Angle [deg]
1	1	6.32 dB	3.52 dB	4.28	2.24	0 ±5°
2	3	-2.90 dB	5.74 dB	0.51	3.74	32 ±5°
3	2	-3.65 dB	7.05 dB	0.43	5.06	150 ±5°

Table 8.1: Parameters for preparing a bound entangled state: This table provides the experimental parameters i.e. squeezing, anti-squeezing and relative phases between the squeezed states, in order to produce a bound entangled state. The relation between the amount of squeezing and anti-squeezing can be controlled by introducing additional thermal noise in the form of a variable beam splitter in the path in of the squeezed mode. The hot squeezing, Mode 1, is produced by locking OPA1 in amplification and phase modulating the control beam entering the OPA cavity.

The first squeezed mode, produced by OPA1, corresponds to the "hot squeezing" described in Section 5.3. This mode is mixed with a "cold squeezed" state produced by OPA3 at phase-gate 1 (PHG1). This state is not entangled as can be verified by the Simon criterion, $\gamma^{T_A} = 0.0544$. The initial amount of NPT entanglement required for the preparation of bound entanglement is produced by mixing the cold squeezing output of OPA2 with the vacuum state on BS2. As characterized in Section 7.5, this corresponds to a V-class entangled state and contains $E_{\mathcal{N}} = 0.607$ bits of entanglement. The outputs of BS2 and PHG1 are then mixed at phase-gate 2 (PHG2) and phase-gate 3 (PHG3). The final output is a four party state which is measured at the homodyne detectors.

Successful preparation and verification of bound entanglement demands an accurate preparation of the underlying squeezed states and setting of the phase-gates. In order to decouple the setting of the phase-gates from the setting of the homodyne detectors and to ensure that the inputs to the phase-gates are correctly measured, a systematic approach is needed to treat each of the building blocks separately while incorporating enough redundancy to check each step of the process. This approach is the subject of the next few sections.

8.1.1 Preparing the Input Squeezed States

The first step in the preparation of bound entanglement is to produce the correct amount of squeezing and anti-squeezing from each of the individual OPAs. The characterization of the input squeezed states requires that they be homodyned. The initial squeezing, however, suffers major losses due to the open phase-gate beam splitters before reaching the homodyne detectors. As a result the entire experiment must first be modeled and the initial squeezing and anti-squeezing levels must be inferred from the mixed states that reach the homodyne detectors. The modeling is performed by assuming the target input state from OPA1 is given by the covariance matrix

$$\gamma_{\text{target}} = \begin{pmatrix} 4.28 & 0 \\ 0 & 2.24 \end{pmatrix}. \tag{8.1}$$

The state that would be measured by Charlie's homodyne detector is given by

$$\gamma_{\text{Charlie}} = A^T \gamma_{\text{target}} A + C \tag{8.2}$$

where

$$A = \begin{pmatrix} \sqrt{\eta} & 0 \\ 0 & \sqrt{\eta} \end{pmatrix}, \quad C = \begin{pmatrix} 1-\eta & 0 \\ 0 & 1-\eta \end{pmatrix}, \tag{8.3}$$

are the matrices representing the loss channel and η specifies the amount of light transmitted through a single beam splitter. The formula is implemented recursively for each open beam splitter in the path towards Charlie. For OPA1, the expected covariance matrix at Charlie is

$$\gamma_{\text{OPA1}} = \begin{pmatrix} 1.79 & 0 \\ 0 & 1.30 \end{pmatrix}. \tag{8.4}$$

The homodyne detector is scanned in order to measure all quadratures. The squeezing and anti-squeezing values correspond to the maximum and minimum values recorded. Since the variances are recorded in real-time, the amount of squeezing, anti-squeezing and extra thermal noise can be adjusted while the data is being recorded. This is performed for each of the three OPAs and is a rough estimate of the amount of input squeezing and anti-squeezing.

8.1.2 Setting the Phase-Gate Operating Point

Having roughly set the input squeezed states, the next step is to set the phase-gates to their operating point as given in Table 8.1. The accuracy of the input states can be checked once again by noting that the quantity

$$\frac{1}{2}\text{tr}\,(\gamma)\,, \tag{8.5}$$

represents the overall noise in the quantum state and is therefore invariant to rotations [CS85]. Another way to understand this invariance is to recall the Hamiltonian for the quantum harmonic oscillator

$$H = \hbar\omega\left(\hat{n} + \frac{1}{2}\right) = \hbar\omega\left(\hat{X}_1^2 + \hat{X}_2^2\right). \tag{8.6}$$

Equation (8.6) establishes the energetic equivalence between the particle and wave description of light. It also states that the average number of photons, $\bar{n}$, in a state is equal to the average quadrature noise. Since rotations in phase-space neither create nor destroy the number of photons, Equation (8.6) and Equation (8.5) are rotation invariant. The rotational invariance of the total quantum noise can be utilized to check the inputs to each phase-gate in the way depicted in Figure 8.2a-b. The outputs of OPA1 and OPA3 are mixed at PHG1, and locked to an arbitrary relative phase. The output is then homodyned by Charlie and produces a result depicted in Figure 8.2a. The red curve represents some initial values for the input states from OPA1 and OPA3. Increasing either of these results in the green curve. Whereas the average value of the variances was 1.82, it is now 1.93. Therefore, if the input states to any phase-gate are correct, the average value of the quantum noise at the output of the phase-gate should match the expected value. Table 8.2 summarizes the average values of the quantum noise expected from one output of each phase-gate.

Once the input states to each phase-gate have been fine tuned, the angle between the incident quantum modes can be set by examining the difference between the maximum and minimum noise variance recorded by the homodyne detector. A pictorial description of the

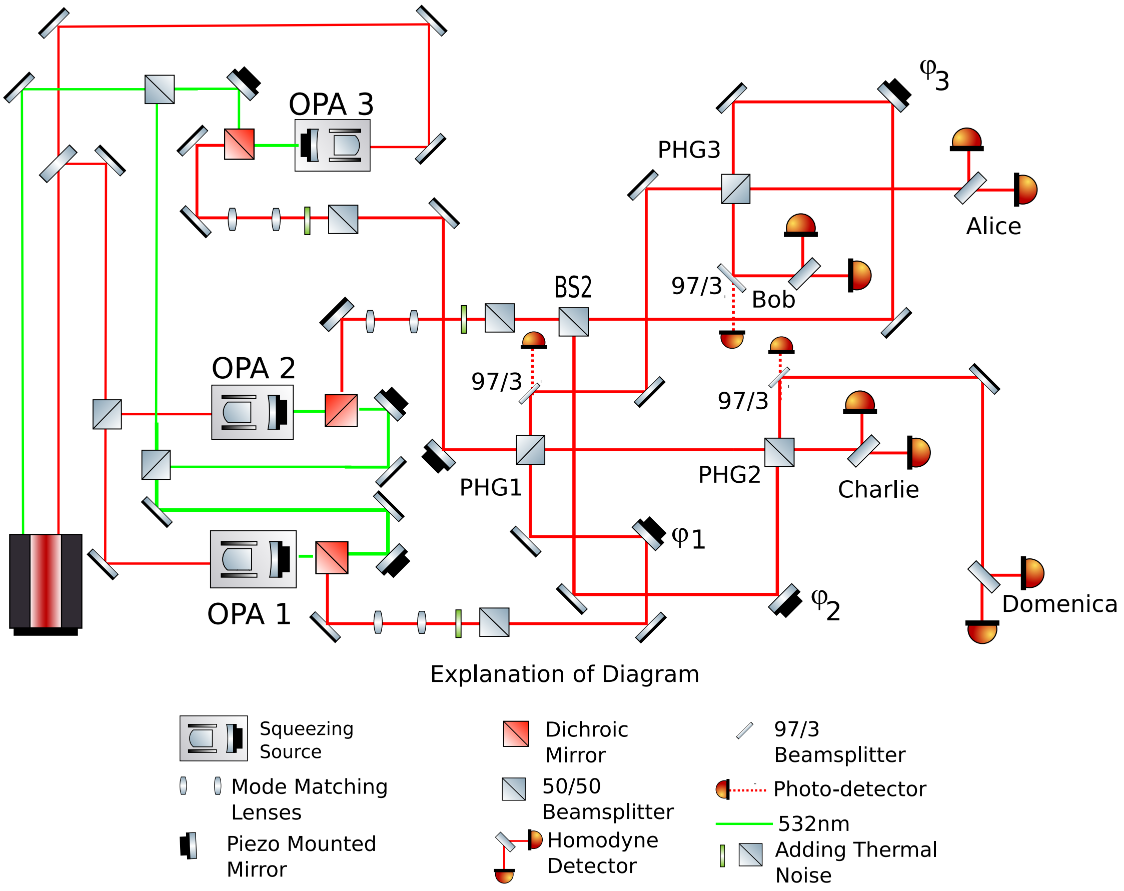
OPA 3
OPA 2
OPA 1
BS2
PHG1
PHG2
PHG3
97/3
97/3
97/3
φ1
φ2
φ3
Alice
Bob
Charlie
Domenica
Explanation of Diagram
Squeezing Source
Mode Matching Lenses
Piezo Mounted Mirror
Dichroic Mirror
50/50 Beamsplitter
Homodyne Detector
97/3 Beamsplitter
Photo-detector
532nm
Adding Thermal Noise

FIGURE 8.1: Exact experimental setup: The experiment is constructed from three optical parametric amplifiers, OPAs, a network of beam splitters, homodyne detectors and some extra loss channels. The OPAs generate the fundamental squeezing resource used to produce the initial entanglement. The network of beam splitters together with piezo mounted mirrors, form phase-gates which set the relative phase between the quantum noise amongst the different modes. The entire experiment is controlled using a single-sideband optical RF technique. The data acquisition occurs using a National Instruments DAQ card and LabView for partial post-processing of the data.

Phase-Gate	Homodyne Detector	Avg
1	Charlie	183
2	Charlie	2.24
3	Alice	2.03

TABLE 8.2: Average noise of phase-gates: This table provides the average value of the quadrature noise of a single mode from a phase-gate output as measured in a homodyne detector. This value depends only on the input states and can therefore be used to check whether the input states have been correctly set.

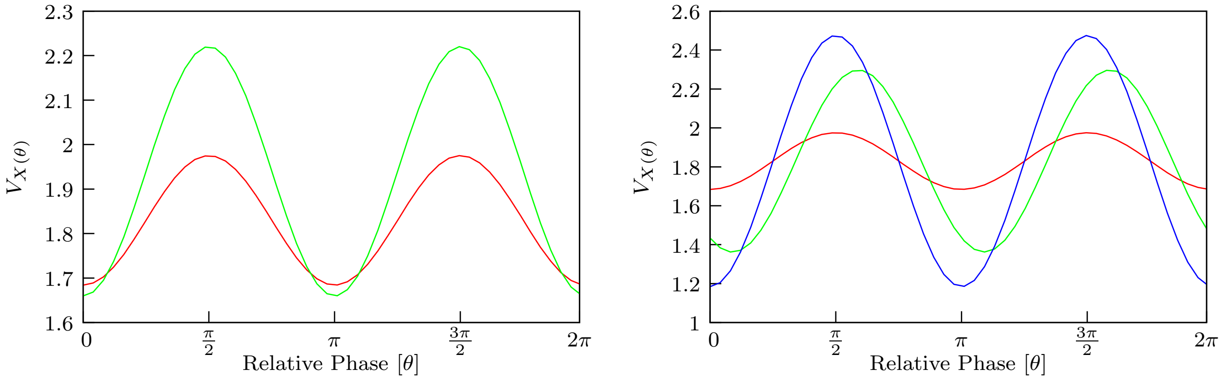

(a) Increasing the Squeezing

(b) Increasing the Relative Phase

Figure 8.2: Method for setting the phase-gates: When setting the phase-gates to their operating point, both the input states to the beam splitter and the relative phase between the quantum noise can be checked. The abscissa corresponds to the variance of the rotated quadrature for an arbitrary angle θ and the ordinate the homodyne angle. Figure (a) illustrates the effect of increasing the amount of squeezing entering the phase-gate for a given phase angle. The entire curve is shifted to a new average value indicating the overall increase in the level of quantum noise or photon number. Figure (b) illustrates the effect of changing the relative phase between the input states for a given amount of squeezed input. The average value remains constant whereas the maximum and minimum variance change with a changing phase angle.

task is given in Figure 8.3. Each input mode is composed of two parts: a bright coherent part at the carrier frequency, (shown in red), and squeezed vacuum noise at sideband frequencies within the linewidth of the OPA, (yellow ellipses). Of interest is the interference of the quantum noise. As the relative phase between the bright carriers changes, the orientation of the squeezing ellipses with respect to each other also changes. This is illustrated in Figure 8.3 for two different cases: the carrier fields interfering at 0° and at 90°. In both cases, the resultant vector of the coherent part of the field is shown in green and the resulting quantum noise possess a red dashed boarder. The distribution of the quantum noise is a function of this phase angle and ranges from a thermal state to a “cold squeezed” state. The relative phase between the quantum noise ellipses is inferred by calculating the expected maximum and minimum values for the noise variances and changing the relative phase between the bright carriers until that point is reached.

When setting the phase-gates, the working point must be set to the exact angle returned from the simulations. The second phase-gate is an example of this point. The inputs to PHG2 are composed of the output from OPA2 and one of the outputs of PHG1. The target relative phase between the quantum noise of the input stats is, according to Table 8.1, 32°. It is important to note that 32° is not equivalent to 328°. This is especially seen in the covariances and the cross-variances of the resulting four-mode state. Table 8.3 provides an example of what occurs when only PHG2 is set to 328°.

There is no real way to determine if either PHG2 or PHG3 have been set correctly without first constructing the complete state and measuring the covariances and cross-variances between the different modes. Having constructed a four-mode state and determined whether

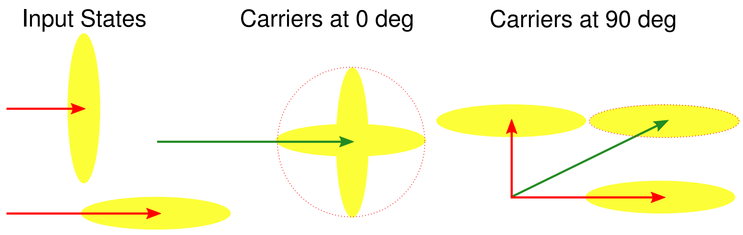

FIGURE 8.3: Setting the phase-gates: This diagram depicts the physical situation behind locking phase-gate 1 (PHG1). The input states are composed of a coherent part, shown in red, modulated by quantum noise shown here by the yellow ellipses. Setting the relative phase between the carriers to be 0° results in the quantum part of the field to interfere at 90° whereas when the carriers are at 90° with respect to each other the quantum part of the field to interfere at 0°. This produces states which can be distinguished by scanning a homodyne detector and examining the behavior of the variances of the different quadratures.

Relative Phase	Cov(p_A, x_D)	Cov(x_B, x_D)	PPT
32°	-0.27	1.16	0.0309
328°	0.34	0.53	-0.1563

TABLE 8.3: The relative phases between the quantum states at each phase-gate must be set exactly. This table illustrates the point using phase-gate 2. The first column corresponds to two different phases which are mathematically equivalent. The second and third columns show the cross-variance between Alice's phase quadrature and Domenica's amplitude quadrature and the co-variance between Bob's amplitude quadrature and Domenica's amplitude quadrature, respectively. The fourth column gives the resulting PPTness for the global state. As is clearly seen, simply changing the second phase-gate to 328° results in changing from a PPT entangled state to an NPT entangled state.

the state is bound entangled or not, one or both of the phase-gates must be changed to a new position. This can be achieved in the following way. As described in Section 5.2.3, the phase-gates are locked by tapping off a small percentage of the light from each output of the beam splitter and detecting it with a photodetector. The DC output from a single photodetector contains the information as to the relative phase between the bright carrier fields. This in turn can be interpreted in terms of the relative phase between the quantum noise of the input fields. Figure 8.4 illustrates a typical record of the DC output from a single locking photodetector of PHG2. Locking to either the maximum or the minimum value implies that the bright carriers are parallel/anti-parallel with respect to one another. Changing the relative phase between the carriers therefore transforms in a change in the relative phase between the quantum noise. Since the maximum and minimum voltages are known, the exact voltage needed to attain the desired angle between the carriers can be calculated from

$$\theta = \mathrm{acos}\left(\frac{2V - V_{\max} - V_{\min}}{V_{\max} - V_{\min}}\right), \tag{8.7}$$

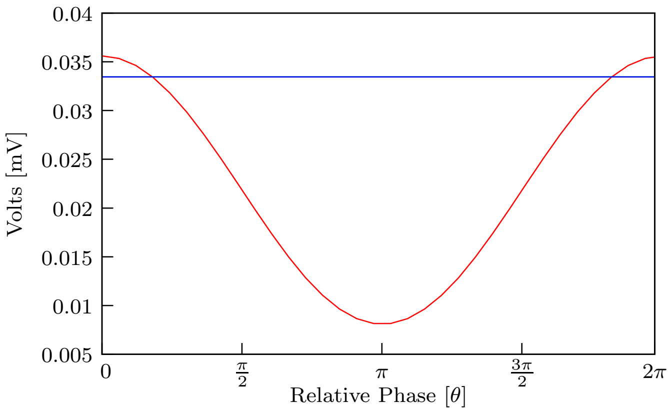

FIGURE 8.4: DC voltage from single phase-gate locking photodetector: The ordinate contains the voltage as read on the oscilloscope and is measured in units of mV. The output voltage is a function of the maximum and minimum voltage as well as the relative phase between the carriers entering the phase-gate. The operational point, corresponding to 32° has the same voltage as an angle of 328°. Both of these points correspond to those that intersect the horizontal line. If after measuring the global state no bound entanglement is detected, the phase-gate can be shifted forwards or backwards to the same voltage but representing a different angle.

and set using an oscilloscope as a guide. In the case of PHG2, there are two different points on either side of the maximum where the angle can be set. If after setting to either one of the working points it is determined that the state is not bound entangled, than the phase-gate simply has to be changed to arrive at the second or third operating point using the oscilloscope as a guide.

8.1.3 Setting the Homodyne Detectors

Having set the input squeezed states and phase-gates to their operating points, the preparation of the bound entangled state is complete. The last stage in the process is the verification of the bound entanglement. This requires performing a set of quadrature measurements on the individual modes of the state in order to measure the full 8×8 covariance matrix. This is facilitated by noting that the amount of entanglement is invariant to local unitary transformations. Therefore any orthogonal basis can be selected for each mode when performing the homodyne detection.

The method for setting the homodyne detectors is similar to that for locking the phase-gates. The DC signal from a single homodyne photodetector is monitored on an oscilloscope and produces a picture given in Figure 8.5. The amplitude quadrature is defined to be that point on the curve where the bright carriers of the signal beam and the strong local oscillator are parallel. By knowing the maximum and minimum voltage, all other quadratures can be calculated (Equation (8.7). This is also depicted in Figure 8.5.

A topographically complete set of measurements for the reconstruction of the covariance matrix requires a total of seven measurement settings, excluding the shot noise measurement, as outlined in Table 8.4, where the first letter corresponds to the quadrature, i.e. x is the

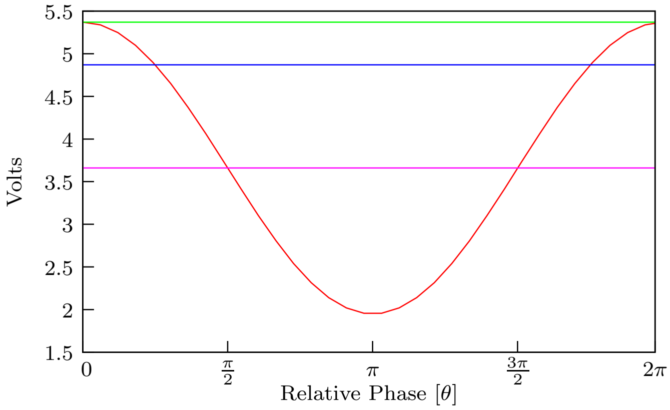

FIGURE 8.5: DC voltage from single homodyne photodetector: Using the DC output from a single homodynde photodetector enables defining an orthogonal basis for performing the homodyne detection. In this plot, the ordinate contains the voltage produced by the photodetector and is measured in units of volts. The three horizontal lines correspond to the three different measurement settings; namely, the amplitude quadrature (green), a linear combination of amplitude and phase (blue), and the phase quadrature (purple). Since entanglement is invariant under local unitary operations, any orthogonal basis could have been chosen.

amplitude quadrature and p is the phase quadrature, and the second letter corresponds to the respective homodyne detector.

8.1.4 Data Acquisition

Data acquisition and partial real-time data analysis is achieved using an National Instruments data acquisition card and LabView interface to record and process the data. The data acquisition occurs at two different levels, measuring the raw data from the homodyne detectors and processing the raw data into statistical moments in real-time to reconstruct the covariance matrix. Before discussing the data analysis, I now provide some more details as to the data acquisition itself.

Data Acquisition Pipeline

The entire data acquisition process is composed of three stages and is depicted in Figure 8.6. The first stage corresponds to photodetection and subtraction of the AC signals from the homodyne photodetectors. It is important at this stage that the electronic gains of the photodetectors are equal. This is because the AC subtracted photocurrent serves two purposes: as a signal for locking the homodyne detector to the operating point and as the signal containing the information regarding the quantum noise.

In the second stage, the AC-subtracted photocurrent is demodulated at a sideband frequency of 6.4 MHz. This produces a signal known as the intermediate frequency or IF signal. The IF signal is than lowpass filtered using a 6^{th} order Bessel filter and sampled at 1 M Samp/s. When performing correlation experiments it is important that electronic delays be

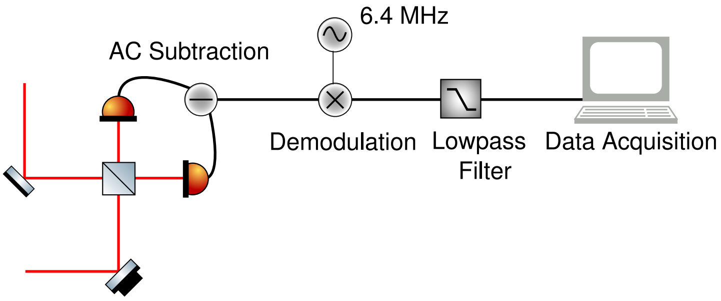

Figure 8.6: Data acquisition pipeline: The data acquisition pipeline begins with basic homodyne detection. The AC signals from the two homodyne photodetectors are externally subtracted and sent to the demodulation box. The AC subtracted signal is mixed down at 6.4 MHz and then lowpass filtered to removed high frequency components. The resulting IF signal is than sampled with a National Instruments analog-to-digital conversion card and post-processed using LabView.

reduced as much as possible. All of the inputs to the lowpass filter must be tested in order to ensure that the phase of each channel is equal. The third stage is the analog-to-digital conversion which takes place in the National Instruments DAQ card.

Real-time Evaluation of Moments

Once the homodyne signals have been acquired, the data is recorded in two different formats: as variances and covariances and as raw numbers. The first format can be achieved by first recording the shot noise level at each homodyne detector and choosing the appropriate normalization. In this thesis, the shot noise is always normalized to a value of one. After saving these values, a LabView application calculates the variances of the individual channels as well as the covariances between the different channels. These values are written to a text file and passed to a Matlab script which than reconstructs the covariance matrix by calculating the average of all the recorded variances and covariances. The second formate is obtained by writing directly to a binary file the voltages measured with the DAQ. This data is not processed during the acquisition. In total, between two and four million data points are collected at a sampling rate of one million samples per second.

8.2 Presentation and Analysis of Results

In this last section I present and analyze the results of several experiments performed to generate a Gaussian quadrature bound entangled state. As I showed in Section 4.1, there are two conditions that must be satisfied for verification of bound entanglement, 1) that the state is PPT and 2) that is the state is separable. In addition to these two conditions, a third condition will be added; namely, that the reconstructed covariance matrix indeed represents a physical state. This third condition is important because a measured matrix

Data File	Quadratures
dataSetshot	Shot Noise
dataSet1	xa xc xb xb
dataSetsub	45 deg
dataSet2	pa pc pb pb
dataSet3	xa pc xb xb
dataSet4	xa xc pb xb
dataSet5	xa xc xb pb
dataSet6	pa xc xb xb

Table 8.4: Measurement Settings: This table presents the measurement settings that are needed to reconstruct the 8×8 covariance matrix. The first letter corresponds to the quadrature being measure, e.g. x is the amplitude quadrature, and the second letter is the first initial of the homodyne detector which is measuring. In total seven measurements are required excluding the shot noise measurement.

which represents an unphysical state indicates that the error-bars on the estimation of the matrix are large. In what follows, I represent these conditions by the following symbols:

$$\text{Physical} \rightarrow \ \lambda, \quad \text{PPT} \rightarrow \ \Gamma^{T_A}, \quad \text{Separable} \rightarrow \ \text{E}_{\text{sep}}.$$

In this section, I also present a method for performing the error analysis and dicuss some features of these experiments.

8.2.1 First Results

The first set of results I present is the 8×8 covariance matrix obtained from directly measuring the second moments from the homodyne detectors using LabView. The matrix reads

$$\Gamma = \begin{pmatrix} 1.5905 & 0.1034 & 1.0342 & -0.3472 & 0.3327 & -0.0235 & -0.5476 & -0.4164 \\ 0.1034 & 1.9752 & 0.2119 & -0.8267 & -0.3137 & -0.1324 & 0.1041 & -0.0507 \\ 1.0342 & 0.2119 & 1.9359 & -0.4295 & 0.3175 & -0.1596 & -0.4034 & -0.5643 \\ -0.3472 & -0.8267 & -0.4295 & 2.8163 & -0.1010 & 0.5862 & -0.3493 & -0.3483 \\ 0.3327 & -0.3137 & 0.3175 & -0.1010 & 1.1656 & -0.2195 & -0.3070 & -0.4764 \\ -0.0235 & -0.1324 & -0.1596 & 0.5862 & -0.2195 & 2.4249 & -1.0790 & 0.6791 \\ -0.5476 & 0.1041 & -0.4034 & -0.3493 & -0.3070 & -1.0790 & 1.9172 & -0.5221 \\ -0.4164 & -0.0507 & -0.5643 & -0.3483 & -0.4764 & 0.6791 & -0.5221 & 2.1324 \end{pmatrix},$$

with entanglement properties

$$\lambda = 0.0153, \quad \Gamma^{T_A} = 0.0021, \quad \text{E}_{\text{sep}} = 0.9993. \tag{8.8}$$

Each entry of the covariance matrix is averaged over 300 realization of the respective moment where the moments were calculated using 20,000 raw data points directly sampled from the homodyne detectors and normalized to vacuum noise. All three requirements for bound entanglement are satisfied by this state.

8.2.2 Data Binning

The results presented in Section 8.2.1 correspond to a verification of bound entanglement which was prepared experimentally. However, it is difficult to perform a reasonable statistical error analysis due to the way the data has been collected and the few raw data points that are used in the calculation of the second moments. A method to place error bars on the entanglement properties of the state is to record large amounts of raw data for each measurement setting and than to "bin" the data into blocks of a finite size and produce multiple covariance matrices from which the ppt and separability criteria can be calculated. In order to keep the error bars small, bins of 1 million data points should be used when calculating the covariance matrix. The results of this method are presented in Table 8.5. From the entanglement properties alone it is tempting to declare a verification of bound entanglement. The state, however, violates the condition for representing a bona fide physical state. In order to satisfy this condition, one can try to alter the measured covariance matrix for each bin such that it does satisfy the physicality condition. The way to do this is the topic of the next section.

Bin	λ	Γ^{T_A}	E_{sep}
1	-0.0097	0.0109	0.9896
2	-0.0066	0.0186	0.9929
3	-0.0054	0.0227	0.9942
4	-0.0045	0.0156	0.9951

Table 8.5: Data binning results: The entanglement properties of the reconstructed state using data binning with 1 million raw points in each bin. From the entanglement properties alone it is tempting to declare a verification of bound entanglement. The fact that each matrix fails the bona fide condition, however, is an indication that the measurement error-bars are still too large.

8.2.3 Determining Physical Matrices

In the process of reconstructing the covariance matrix from the raw data it may occur that matrix, Γ, violates the Heisenberg uncertainty relation

$$\Gamma + i\Omega \geq 0, \tag{8.9}$$

where Ω is the symplectic form as defined in Section 3.1.1. One way to solve this problem is to look for the nearest physical covariance matrix, γ, and use it as the reconstruction of the measured state. The nearest minimum state is defined as that state which minimizes the norm between the two matrices. This is a problem in convex semidefinite programming and can be stated as

$$\begin{aligned} \min \quad & \|\gamma - \Gamma\|_2, \\ \text{subject to} \quad & \gamma + i\Omega \geq 0, \\ & \gamma = \gamma^T, \end{aligned} \tag{8.10}$$

Bin	λ	Γ^{T_A}	E_{sep}
1	0.0000	0.0162	1.0000
2	0.0000	0.0221	1.0000
3	0.0000	0.0256	1.0000
4	0.0000	0.0180	1.0000

Table 8.6: Data binning results using 2-norm: When adjusting the measured covariance matrix to fit the nearest physical state, the entanglement properties change such that all reconstructed states become separable. The same analysis is performed using the 1-norm and is presented in Table 8.7.

Bin	λ	Γ^{T_A}	E_{sep}
1	0.0009	-0.0646	0.9129
2	0.0012	-0.0700	0.9055
3	0.0014	-0.0683	0.9081
4	0.0014	-0.0700	0.9057

Table 8.7: Data binning results using 1-norm: When adjusting the measured covariance matrix to fit the nearest physical matrix using the 1-norm the entanglement properties of the state change such that it becomes NPT entangled. This is the complete opposite conclusion one would draw when using the 2-norm. The reasons for this are discussed in the text.

where the 2-norm is the Frobenius norm defined by

$$\|\gamma - \Gamma\|_2 = \operatorname{tr}\left((\gamma - \Gamma)^2\right). \tag{8.11}$$

The method described in Equation (8.10) was applied to the data set corresponding to Table 8.5. Repeating the binning method and correcting each resulting covariance matrix such that the uncertainty relation is statisfied produces the results in Table 8.6. Although all of the states are now physical, they also are all separable. The choice of the norm influences the resulting entanglement properties of the reconstructed state. Instead of using the 2-norm in the minimization, the 1-norm, which is defined by $\|\gamma - \Gamma\|_1 = \operatorname{tr}\left(|\gamma - \Gamma|\right)$, could also be used and produces the results in Table 8.7. This is a significant difference from the results in Table 8.6. It is an indication that although the state may in fact be bound entangled, the level of experimental and statistical noise should be further reduced either by taking more data or seeking to prepare a more robust bound entangled state.

8.3 Summary

In this chapter I have presented first results indicating the experimental demonstration of bound entanglement. In order to make the verification even more convincing, data should be collected such that the entanglement properties are independent of the choice of matrix norm. The results presented here indicate that the prepared states are close to the boarder from being NPT entangled, PPT entangled or separable. An experimental procedure was developed to construct a four party entangled state and is completely general enough to be used in the preparation of arbitrarily entangled multipartite states. The final chapter of the thesis contains a general conclusion as well as an outlook for further research.

9

Conclusion and Outlook

In this concluding chapter I will present some ideas for further research based on the three experiments performed for this thesis. Beginning with quantum state reconstruction, the problem of reconstructing a phase-diffused squeezed state was reduced to estimating three parameters which completely characterized the non-Gaussian Wigner function. This assumed, however, a specific model for the these states. The model of the state may not, however, always be known. For example, when trying to estimate the density matrix of a single-mode squeezed state, a truncation of the infinite dimensional Hilbert space is required. Letting N represent the dimension of the truncated Hilbert space, the first question to be answered is "how large should N be". Leonhardt and Munroe [LM96] addressed the issue of the number of homodyne phases that should be measured for a given truncation. They also attempted to quantify the error on the reconstructed state when N is not known but assumed that the state already agrees with the true density matrix. The Bayesian approach provides a better solution. One way to tackle the problem would be to evaluate the evidence

$$E(D|M\,, I) = \int \mathcal{L}(D|\vec{\lambda}, M\,, I)\pi(\vec{\lambda}|M\,, I)d\lambda. \tag{9.1}$$

In this case, the model M, corresponds to the size of the Hilbert. The evidence, Equation (9.1), would be evaluated for different truncations, i.e. $M_1 = N = 2, M_2 = N = 3, \ldots M_i = N$ corresponding to different models and would quantify the degree to which the measured data D could have been generated from a specific model. At some point, the data will no longer be informative as to the size of the Hilbert space and at that point the truncation can stop. This would provide a consistent method to estimate not only the parameters of the density matrix but also determine the size of the Hilbert space commensurate with the measured data and prior knowledge.

In Chapter 7 I characterized shared bipartite quadrature entanglement in the laboratory setting. The next steps would be to use these types of channels in actual applications. The first step would be to change the wavelength of the laser source to one of the telecommunication wavelengths currently in use. This would enable long distance quantum communication by sending the states through fiber optic links to spatially separated parties. A second improvement would be to generate pure, highly squeezed states that can be used for quadrature entanglement preparation. Figure 2.8a-b in Section 2.4.2 shows that whether it be transmitting unknown quantum information, i.e. teleportation, or classical information, i.e. dense coding, the information carrying capacity of the channel is a function of the underlying entanglement strength. Since the strength of quadrature entanglement depends on the strength of the underlying squeezing, strong squeezed states are required in order to increase the channel capacity of any quantum resource. A third possibility would be to combine fundamental primitives, such as entanglement distillation [HSD$^+$08] with teleportation [FSB$^+$98, BTB$^+$03a]. Such research would be the beginnings of *quantum engineering* and would serve as the foundation for constructing more elaborate large scale quantum communication networks.

Finally, the preparation of continuous-variable bound entanglement will always require the generation of a multiparty entangled state. This could serve as the motivation for developing new techniques for the construction of such states which could also be used for one-way quantum computing in the form of cluster states [YUvLF08]. From the fundamental perspective, there has been much work in the recent years in developing the thermodynamics of entanglement [HH98, HHH01, MNV09, HOH02, Ved99, PV01]. I discussed in Section 4.3 how entanglement can be uniquely quantified when considering reversible transformations. Mixed state entanglement was given as an example of an irreversible entanglement transformation and I showed how this can still be quantified by using the von Neumann entropy. Bound entanglement was seen to be an example of an irreversible entanglement transformation, since NPT entanglement is required for its preparation but cannot be obtained through distillation of the bound entangled state. There is an interesting connection between physical irreversibility and so called “information erasure”. This was first established in the 1960’s when Landauer recognized that irreversible computation implied information erasure in computing machines [Lan61]. He argued that in erasing information, a minimal amount of heat is released into the environment equal to

$$S = kTn \ln 2, \tag{9.2}$$

where n corresponds to the number of bits, T is the temperature of the environment and k is Boltzmann’s constant.

Using bound entanglement as a test bench, Landauer’s principle could be further explored in its relation to quantum states. For example, it could be investigated as to whether information erasure is the reason why bound entangled states retain their inseparability but lose their distillability properties. Additionally, a generalized notion of protocol efficiency, similar to that defined for the Carnot heat engine, could also be developed and tested to determine how well a distillation protocol can work given a certain entangled state or what the maximal capacity of a channel is for information transfer.

The research program I have just suggested can be conducted using entangled states of light. It has the potential to open the doors to discovering new forms of entanglement as well as acquiring a better understanding of those already known.

A

Rules for Experimentalists

In this appendix I discuss some issues that have reappeared repeatedly throughout my time as a PhD student. I known of no text which covers these typical problems in the life of an experimentalist and therefore have sought to gather as much as I could into one common place for the next generation. I hope that these notes can be both useful as well as serve as a starting point for further investigation.

A.1 Rule 1: Impedance Matching

Impedance matching is an absolute must for anyone who hopes to actually have their electronics work as expected. It becomes especially important when working with RF signals, or as Andreas Weidner would say, when working with anything "you cannot hear" [Wei]. For example, whereas a servo for locking the relative phase between the squeezed beam and the local oscillator produces AC voltages in the kilohertz regime, the actual detection of squeezed and entangled states generally speaking occurs at sideband frequencies on the order of MHz. It is for these frequencies were impedance matching becomes important.

Quickly stated, an impedance is the generalization of a resistance for frequency sensitive components. There are three types of impedances which are summarized in Table A.1. All three types may be present in any one circuit or cable and large impedances are not required in order to have a discernible effect.

Type	Z
Resistive	R
Capacitive	$\frac{1}{i\omega C}$
Inductive	$i\omega L$

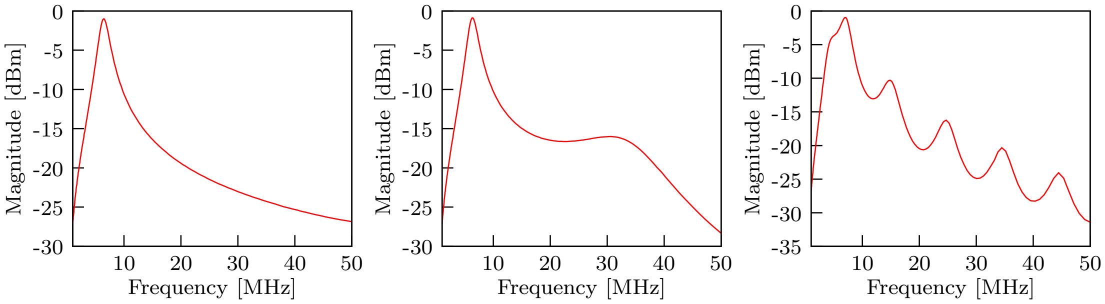

(a) 1 meter cable (b) 3 meter cable (c) Very long cable

FIGURE A.1: Effect of impedance matching: These transferfunctions are suppose to correspond to a passive bandpass filter at 6.4 MHz. Depending on how long the cables connecting the circuit to some 50 Ω input device are determines how bad the transferfunction behaves.

To illustrate the effect of impedances on circuit operation, Figure A.1a-c depicts three transferfunctions of the same circuit. The circuit is a passive bandpass filter which should pass frequencies at or around 6.4 MHz and suppress all others. In order to measure the transferfunction, the circuit was attached to a network analyzer which has a 50 Ω input impedance. Figure A.1a illustrates what happens when the connecting cables are 1 m long. The transferfunction looks good. Figure A.1b-c illustrate what happens when the cable lengths are increased. The transferfunction becomes distorted and finally the circuit no longer behaves as it should.

The reason why this happens is because the cables have their own finite impedance. The circuit has its own input and output impedance and the network analyzer as its well defined input impedance. As long as the entire circuit, cables and network analyzer, are not all set to 50 Ω, nothing with work properly. There are two solutions to this problem. The first is to measure all input and output impedances and build a passive circuit which performs the impedance matching. The second, is to use buffer circuits composed of operational amplifiers to achieve the same result.

The choice is yours....have fun!

A.2 Rule 2: Ground loops

It has often been the case that when trying to measure a DC voltage or when trying to control the temperature of an OPA crystal, a strange low frequency “oscillation” appears on the signal. Sometimes this is due to ground loops. Ground loops are the result of a circular connection of references. Remembering that a voltage is a potential, defined with respect to some point, having multiple “some point” changes the way that voltages are defined. This can cause problems in the experimental setup.

In order to avoid ground loops, Andreas Weidner has laid the dogmatic groundwork for a New Electrical Religion. The following Commandments are from him.

1. Thou shalt create a common low-impedance earth and ground reference

2. Thou shalt connect accessible metallic device parts to low-impedance earth
3. Thou shalt distribute earth and ground star-shaped to all devices
4. Thou shalt known your internal hardware wiring
5. Thou shalt use predefined designing and wiring recipes
6. Thou shalt categorise and label all cables
7. Thou shalt connect measurement equipment properly
8. Thou shalt think before wiring, and not after it
9. Thou shalt ask for guidance when in doubt
10. Thou shalt be patient

A.3 Rule 3: RF Pickup

Antennas are great if you want to listen to Deutsche Schlager. Building one in the lab is, however, not such a great idea. And yet this is precisely what will happen if the proper precautions are not taken. This last section gives a brief overview of some of these issues.

The problem is a follows. Say you need to lock a homodyne detector and decide to do this by imprinting a phase modulation at 15 MHz on one of the beams. After interference with the strong local oscillator, this phase modulation is converted into an even stronger amplitude modulation at the same frequency. The photodetector converts this strong amplitude modulation into a strong AC signal which gets sent through the cables to the next device, usually an external subtracter. Herein lies the problem. Depending on what cables are being used, this 15 MHz signal is now going to be broadcasted throughout the lab. Any equipment which is sensitive to this frequency will detect it and you will probably see it in some form, somewhere in the experiment. To eliminate this problem, think about the following before building the experiment:

1. Does my modulation amplitude need to be so large?
2. Are all of my devices properly impedance matched?
3. Can I perform demodulation and low pass filtering all on one circuit board?
4. Are my cables properly insulated?

Spending some time to answer these questions can potentially save weeks of work.

References

[AC00] A. Abramovici and J. Chapsky, *Feedback control systems: A fast-track guide for scientists and engineers*, Kluwer Academic, 2000.

[AGR81] A. Aspect, P. Grangier, and G. Roger, Phys. Rev. Lett. **47** (1981), 460.

[AI05] G. Adesso and F. Illuminati, Phys. Rev. A **72** (2005), 032334.

[ATM$^+$04] R. Alléaume, F. Treussart, G. Messin, Y. Dumeige, J. F. Roch, A. Beveratos, R. Brouri-Tualle, J. P. Poizat, and P. Grangier, New. Jour. Phys. **92** (2004).

[BBC$^+$93] C. Bennett, G. Brassard, C. Crepeau, R. Jozsa, A. Peres, and W. Wootters, Phys. Rev. Lett **70** (1993), 1895.

[BBPS96] C. H. Bennett, H. J. Bernstein, S. Popescu, and B. Schumacher, Phys. Rev. A **53** (1996), 2046.

[BDPS99] K. Banaszek, G. .M. D'Ariano, A. Paris, and M. F. Sacchi, Phys. Rev. A **61** (1999), 010304(R).

[BDSW96] C. H. Bennett, D. P. DiVincenzo, J. A. Smolin, and W. K. Wootters, Phys. Rev. A **54** (1996), 3824.

[BG98] S. P. Brooks and A. Gelman, *General methods for monitoring convergence of iterative simulations*, Journal of Computational and Graphical Statistics **7** (1998), no. 4, 434–455.

[BK98] S. L. Braunstein and H. J. Kimble, Phys. Rev. Lett. **80** (1998), 869.

[BK00] S. L. Braunstein and H. J. Kimble, Phys. Rev. A. **61** (2000), 042302.

[BL06] D. Bruss and G. Leuchs, *Lectures on quantum information*, Wiley-VCH, Berlin, 2006.

[BS97] G. Breitenbach and S. Schiller, J. Mod. Opt. **44** (1997), 2207.

[BSLR04] W. P. Bowen, R. Schnabel, P. K. Lam, and T. C. Ralph, Phys. Rev. A **69** (2004), 012304.

[BTB$^+$03a] W. P. Bowen, N. Treps, B. Buchler, R. Schnabel, T. C. Ralph, T. Symul, and P. k. Lam, IEEE. Quant. Elec. **9** (2003), 1519.

[BTB$^+$03b] W. P. Bowen, N. Treps, B. C. Buchler, R. Schnabel, T. C. Ralph, H. A. Bachor, T. Symul, and P. K. Lam, Phys. Rev. A. **67** (2003), 032302.

[BvL05] S. L. Braunstein and P. van Loock, Rev. Mod. Phys. **77** (2005), 513.

[BW92] C. Bennett and S. J. Wiesner, Phys. Rev. Lett. **69** (1992), 2881.

[CCMR05] N. J. Cerf, J. Clavareau, C. Macchiavello, and J. Roland, Phys. Rev. A **74** (2005), 042330.

[CD94] C. M. Caves and P. D. Drummond, Rev. Mod. Phys. **66** (1994), 481.

[CG69] K. E. Cahill and R. J. Glauber, Phys. Rev. **177** (1969), 1882.

[Che07] S. Chelkowski, *Squeezed light and laser interferometric gravitational wave detectors*, Ph.D. thesis, Faculty of Mathematics and Physics of the University of Hanover, Hanover, Germany, 2007, url: http://www.aei.mpg.de/hannover-de/07-instPublikationen/Dissertationen.

[CL96] Bradley P. Carlin and Thomas A. Louis, *Bayes and empirical bayes methods for data analysis*, Chapman and Hall, 1996.

[CS85] C. M. Caves and B. L. Schumaker, Phys. Rev. A **31** (1985), 3068.

[CT06] T. M. Cover and J. A. Thomas, *Elements of information theory*, 2nd ed., John Wiley and Sons, 2006.

[Dev05] I. Devetak, IEEE. Trans. Inf. Th. **51** (2005), 44.

[DGCZ00] L. M. Duan, G. Giedke, J. I. Cirac, and P. Zoller, Phys. Rev. Lett. **84** (2000), 2722.

[DHF$^+$07] J. DiGuglielmo, B. Hage, A. Franzen, J. Fiurášek, and R. Schnabel, Phys. Rev. A **76** (2007), 012323.

[DiG06] J. DiGuglielmo, *Entangled states of light*, Master's thesis, Faculty of Mathematics and Physics of the University of Hanover, 2006.

[DLH$^+$08] R. Dong, M. Lassen, J. Heersink, C. Marquardt, R. Filip, G. Leuchs, and U. Andersen, Nature Phys. **4** (2008), 919.

[DMF$^+$09] J. DiGuglielmo, C. Messenger, J. Fiurášš, B. Hage, A. Samblowski, T. Schmidt, and R. Schnabel, Phys. Rev. A **79** (2009), 032114.

[DPS00] G. M. D'Ariano, M. G. Paris, and M. F. Sacchi, Phys. Rev. A. **62** (2000), 023815.

[DSH$^+$10] J. DiGuglielmo, A. Samblowski, B. Hage, C. Pineda, J. Eisert, and R. Schnabel, In preparation.

[DVV77] B. Demoen, O. Vanheuverzwijn, and A. Verbeure, Lett. Math. Phys. **2** (1977), 161.

[EAFB06] S. El Adlouni, A.-C. Favre, and B. Bobée, *Comparison of methodologies to assess the convergence of Markov chain Monte Carlo methods*, Computational Statistics & Data Analysis **50** (2006), no. 10, 2685–2701.

[EBSP04] J. Eisert, D. Browne, S. Scheel, and M. B. Plenio, Ann. Phys. **311** (2004), 431.

[EP02] J. Eisert and M. B. Plenio, Phys. Rev. Lett. **89** (2002), 097901.

[EW] J. Eisert and M. M. Wolf, quant-ph/0505151.

[FFS07] J. Fiurášek, M. Filip, and R. Schnabel, Phys. Rev. A. **75** (2007), 050302(R).

[FHD$^+$06] A. Franzen, B. Hage, J. DiGuglielmo, J. Fiurášek, and R. Schnabel, Phys. Rev. Lett. **97** (2006), 150505.

[Fiu01] J. Fiurášek, Phys. Rev. A **64** (2001), 024102.

[Fiu02] J. Fiurášek, Phys. Rev. A **66** (2002), 012304.

[FPEN05] G. F. Franklin, J. D. Powell, and A. Emami-Naeini, *Feedback control of dynamic systems*, 5 ed., Prentice-Hall, 2005.

[FSB$^+$98] A. Furusawa, J. L. Sorensen, S. L. Braunstein, C. A. Fuchs, H. J. Kimble, and E. S. Polzik, Science **23** (1998), 706.

[GAW$^+$03] F. Grosshans, G. Van Assche, J. Wenger, R. Brouri, N. J. Cerf, and P. Grangier, Nature **421** (2003), 238.

[GCSR04] Andrew Gelman, John B. Carlin, Hal S. Stern, and Donald B. Rubin, *Bayesian data analysis*, second ed., Chapman and Hall/ CRC, 2004.

[GG01] F. Grosshans and P. Grangier, Phys. Rev. A. **64** (2001), 010301.

[GK05] C. Gerry and P. Knight, *Introductory quantum optics*, Cambridge Unviersity Press, 2005.

[GKD$^+$01] G. Giedke, B. Kraus, L. M. Duan, P. Zoller, J. I. Cirac, and M. Lewenstein, Fortschr. Phys **49** (2001), 973.

[GKLC] G. Giedka, B. Kraus, M. Lewenstein, and J. I. Cirac, Phys. Rev. Lett. **87**, 167904.

[GKLC01a] G. Giedke, B. Kraus, M. Lewenstein, and J. I. Cirac, Phys. Rev. A **64** (2001), 052303.

[GKLC01b] ———, Phys. Rev. Lett **87** (2001), 167904.

[GMVT03] V. Giovannetti, S. Mancini, D. Vitali, and P. Tombesi, Phys. Rev. A. **67** (2003), 022320.

[GPC06] R. García-Patrón and N. J. Cerf, Phys. Rev. Lett. **97** (2006), 190503.

[Gre06] Phil Gregory, *Bayesian logical data analysis for the physical sciences*, second ed., Cambridge University Press, 2006.

[GRS96] W. R. Gilks, S. Richardson, and D. J. Spiegelhalter, *Markov chain monte carlo in practice*, Chapman & Hall/CRC, 1996.

[HE06] P. Hyllus and J. Eisert, New J. Phys. **8** (2006), 51.

[HFD$^+$07] B. Hage, A. Franzen, J. DiGuglielmo, P. Marek, J. Fiurášek, and R. Schnabel, New J. Phys. **9** (2007), 227.

[HH98] M. Horodecki and R. Horodecki, Phys. Lett. A **244** (1998), 473.

[HH99] M. Horodecki and P. Horodecki, Phys. Rev. A **59** (1999), 4206.

[HHH] M. Horodecki, P. Horodecki, and R. Horodecki, quant-ph/9807091.

[HHH01] R. Horodecki, M. Horodecki, and P. Horodecki, Phys. Rev. A **63** (2001), 022310.

[HJSW96] P. Hausladen, R. Jozsa, B. Schumacher, and M. Westmoreland, Phys. Rev. A **54** (1996), 1869.

[HLMS06] H. Haario, M. Laine, A. Mira, and E. Saksman, Stat. Comput **16** (2006), 339.

[HMv06] Z. Hradil, D. Mogilevtsev, and J. Řeháček, Phys. Rev. Lett. **96** (2006), 230401.

[HOH02] M. Horodecki, J. Oppenheim, and R. Horodecki, Phys. Rev. Lett **89** (2002), 240403.

[HOW05] M. Horodecki, J. Oppenheim, and A. Winter, Nature **436** (2005), 673.

[HOW06] ———, Comm. Math. Phys. **269** (2006), 107.

[Hra97] Z. Hradil, Phys. Rev. A **55** (1997), 1561(R).

[HSD$^+$08] B. Hage, A. Samblowski, J. DiGuglielmo, A. Franzen, J. Fiurášek, and R. Schnabel, Nature Physics **4** (2008), 915.

[HSD$^+$10] B. Hage, A. Samblowski, J. DiGuglielmo, J. Fiurášek, and R. Schnabel, Submitted to Nature Physics.

[HST05] H. Haario, R. Saksman, and J. Tamminen, Comput. Stat **20** (2005), 265.

[HW01] A. S. Holevo and R. F. Werner, Phys. Rev. A **63** (2001), 032312.

[Jam72] A. Jamiolkowski, Rep. Math. Phys. **3** (1972), 275.

[JZY^{+}03] J. Jing, J. Zhang, Y. Yang, F. Zao, C. Xao, and K. Peng, Phys. Rev. Lett. **90** (2003), 167903.

[KBLSG01] P. Kwiat, S. Barraza-Lopez, A. Stefanov, and N. Gisin, Nature **409** (2001), 1014.

[KLC02] B. Kraus, M. Lewenstein, and J. I. Cirac, Phys. Rev. A **65** (2002), 042327.

[Lan61] R. Landauer, IBM Journal Reasearch and Development **44** (1961), 261.

[Leo97] Ulf Leonhardt, *Measuring the quantum state of light*, Cambridge University Press, 1997.

[Lin00] G. Lindblad, J. Phys. A: Math. Gen. **33** (2000), 5059.

[LKOH^{+}05] J. Laurat, G. Keller, J. Oliveiria-Huguenin, C. Fabre, T. Coudreau, A. Serafini, G. Adesso, and F. Illuminati, J. Opt. B: Quantum Semiclass. Opt. **7** (2005), S577.

[Llo97] S. Lloyd, Phys. Rev. A **55** (1997), 1613.

[LM96] U. Leonhardt and M. Munroe, Phys. Rev. A **54** (1996), 3682.

[Lub87] E. Lubkin, Int. J. Theor. Phys. **26** (1987), 523.

[Lvo04] A. I. Lvovsky, J. Opt. B **6** (2004), S556–S559.

[Mas06] L. Masanes, Phys. Rev. Lett **96** (2006), 150501.

[MNV09] K. Maruyama, F. Nori, and V. Vedral, Rev. Mod. Phys. **81** (2009).

[MRR^{+}53] N. Metropolis, A. Rosenbluth, M. Rosenbluth, A. Teller, and E. Teller, J. Chem. Phys. **21** (1953), 1087.

[MWFS05] J. Mizuno, K. Wakui, A. Furusawa, and M. Sasaki, Phys. Rev. A. **71** (2005), 012304.

[MWKZ96] K. Mattle, H. Weinfurter, P. G. Kwiat, and A. Zeilinger, Phys. Rev. Lett. **76** (1996), 4656.

[NA05] M. Navascues and A. Acin, Phys. Rev. A **72** (2005), 012303.

[NC00] M. Nielsen and I. L. Chuang, *Quantum computation and quantum information*, Cambridge University Press, Cambridge, 2000.

[NGA06] M. Navascués, R. Grosshans, and Antonio Acín, Phys. Rev. Lett. **97** (2006), 190502.

[Nie04] M. Nielsen, Phys. Rev. Lett. **93** (2004), 040503.

[OTBG06] A. Ourjoumtsev, R. Tualle-Brouri, and P. Grangier, Phys. Rev. Lett. **96** (2006), 213601.

[Per96] A. Peres, Phys. Rev. Lett. **77** (1996), 1413.

[Pin] C. Pineda, Private Communication.

[PR97] S. Popescu and D. Rohrlich, Phys. Rev. A **56** (1997), R3319.

[Pre] J. Preskill, http://theory.caltech.edu/people/preskill/ph229.

[PV01] M. B. Plenio and V. Vitelli, Contemporary Physics **42** (2001), 25.

[RR06] G. Roberts and J. Rosenthal, Stat. and Comput **6** (2006), 269.

[Sam07] A. Samblowski, *Continuous variable entanglement of optical sidebands*, Master's thesis, Faculty of Mathematics and Physics of the University of Hanover, 2007, http://www.aei.mpg.de/hannover-de/07-instPublikationen/diplomarbeiten.

[SBRF93] D. T. Smithey, M. Beck, M. G. Raymer, and A. Faridani, Phys. Rev. Lett **70** (1993), 1244.

[SBT$^+$03] R. Schnabel, W. P. Bowen, N. Treps, T. C. Ralph, H. A. Bachor, and P. K. Lam, Phys. Rev. A **67** (2003), 012316.

[Sch35] E. Schroedinger, Die Naturwissenschaften **48** (1935), 823–28.

[sed] *Matlab toolbox for convex optimization problems*, http://sedumi.ie.lehigh.edu/.

[Sha48] C. E. Shannon, Bell System Tech. Journal **27** (1948), 379.

[Sho02] P. W. Shor, *The quantum channel capacity and coherent information*, 2002, Lecture notes, MSRI Workshop on Quantum Computation.

[Sim00] R. Simon, Phys. Rev. Lett. **84** (2000), 2726.

[Siv06] D. S. Sivia, *Data analysis a bayesian tutorial*, second ed., Oxford University Press, 2006.

[SMD94] R. Simon, N. Mukunda, and B. Dutta, Phys. Rev. A **49** (1994), 1567.

[SN96] B. Schumacher and M. A. Nielsen, Phys. Rev. A **54** (1996), 2629.

[SSM87] R. Simon, E. C. G. Sudarshan, and N. Mukunda, Phys. Rev. A **36** (1987), 3868.

[SV] J. Sperling and W. Vogel, quantun-ph/0908.3974.

[SW72] D. Slepian and J. K. Wolf, IEEE. Trans. Inf. Th. **19** (1972), 461.

[SW97] B. Schumacher and M. Westmoreland, Phys. Rev. A **56** (1997), 131.

[TAK$^+$05] N. Takei, T. Aoki, S. Koike, K. Yoshino, K. Wakui, H. Yonezawa, T. Hiraoka, J. Mizuno, M. Takeoka, M. Ban, and A. Furusawa, Phys. Rev. A. **72** (2005), 042304.

[Vah08] H. Vahlbruch, *Squeezed light for gravitational wave astronomy*, Ph.D. thesis, Faculty of Mathematics and Physics of the University of Hanover, Hanover, Germany, 2008, url: http://www.aei.mpg.de/hannover-de/07-instPublikationen/Dissertationen.

[Ved99] V. Vedral, Proc. R. Soc.Lond. A **456** (1999), 969.

[vELK07] S. J. van Enk, N. Lutkenhaus, and H. J. Kimble, Phys. Rev. A **75** (2007), 052318.

[vHKL07] J. Řeháček, Z. Hradil, E. Knill, and A. I. Lvovsky, Phys. Rev. A **75** (2007), 042108.

[vLF03] P. van Loock and A. Furusawa, Phys. Rev. A. **67** (2003), 052315.

[VPRK97] V. Vedral, M. B. Plenio, M. A. Rippin, and P. L. Knight, Phys. Rev. Lett **78** (1997), 2275.

[VR89] K. Vogel and H. Risken, Phys. Rev. A. **40** (1989), 2847.

[VW02] G. Vidal and R. F. Werner, Phys. Rev. A **65** (2002), 032314.

[Wei] A. Weidner, Private Communication.

[WEP03] M. M. Wolf, J. Eisert, and M. B. Plenio, Phys. Rev. Lett. **90** (2003), 047904.

[Wer89] R. F. Werner, Phys. Rev. A **40** (1989), 4277.

[Wig32] E. Wigner, Phys. Rev **40** (1932), 749.

[wik] http://en.wikipedia.org/wiki/ConjugatepriorTableofconjugatedistributions.

[WOTBG05] J. Wenger, A. Ourjoumtsev, R. Tualle-Brouri, and P. Grangier, Eur. Phys. J. D **32** (2005), 391.

[WPGG07] M. M. Wolf, D. Perez-Garica, and G. Giedka, Phys. Rev. Lett **98** (2007), 130501.

[WW01] R. F. Werner and M. M. Wolf, Phys. Rev. Lett **86** (2001), 3658.

[YBF07] H. Yonezawa, S. L. Braunstein, and A. Furusawa, Phys. Rev. Lett. **99** (2007), 110503.

[YUvLF08] M. Yukawa, R. Ukai, P. van Loock, and A. Furusawa, Phys. Rev. A **78** (2008), 012301.

Acknowledgements

The road to writing this thesis began with my arrival in Hannover in September of 2004. In the course of these six years, many people have contributed in some way to me attaining my ultimate goal of “Promotion”. It is these individuals I would now like to mention.

I would first would like to extend my gratitude to the American-German Fulbright Commission who granted me a one year scholarship to study at the Max-Planck Institut für Gravitationsphysik. It was Prof. Dr. Karsten Danzmann who wrote a letter of recommendation for me and I thank him for giving me the opportunity to come here and work at the institute. I also thank my supervisor, Prof. Dr. Roman Schnabel for his encouragement and support over the years and for taking me into his group six years ago.

There are many former and current remembers of the AEI who were very helpful to me over these years. To my colleagues in the mechanics workshop, Jan, Hans and Filip as well as in the electronics workshop, Heiko and Andreas thank you for your patience and exceptional skill. To Kirsten and Sabine, thank you for helping me to get through all the paperwork and dealing with the university “Beamten”. Laboratory work is more fun when conducted with highly skilled and good natured individuals. To this end I thank Simon Chelkowski, Hank Vahlbruch, Alexander Franzen, Moritz Mehmet, Daniel Friedrich, Michi Britzger, Nico Lastzka and many others who made working here a really great experience. A special thanks to Paul Couchrane who read many of the chapters in this thesis and whose advice was most useful throughout the whole writing process. I especially want to thank Aiko Samblowski who, with the last experiment, helped me obtain not only the experimental results but also helped me keep my sanity and motivation over the months leading up to our results. Thank you Aiko!

My life here in Hannover was not just about physics. Along the way I made many friends and learned alot from each of them. Marcin Czubanowski was not only a good friend but great adviser. Przemek, Hung and Fadi taught me an enormous amount about all sorts of things. My roommates in the Burse especially Annemarie, Georg, Audace and Lars made living with seven people a whole lot of fun.

Finally, I would like to thank my immediate family, Mom, Dad, Lisa, Michael, my dearest friends Jeff and David and my German family, Meike, Uli, Hendrik, Marion and Markus for their patience, sacrifice and constant encouragement during my stay in Germany.

Selbständigkeitserklärung

Hiermit versichere ich, die vorliegende Arbeit allein und selbständig und lediglich unter Zuhilfenahme der genannten Hilfsmittel und Quellen angefertigt zu haben, und dass die Dissertation nicht schon als Masterarbeit, Diplomarbeit oder ähnliche Prüfungsarbeit verwendet worden ist.

James DiGuglielmo
Juni 2010